

REPORT DOCUMENTATION PAGE

The public reporting burden for this collection of information is estimated to average 1 hour per response, including the time for reviewing instructions, searching existing data sources, gathering and maintaining the data needed, and completing and reviewing the collection of information. Send comments regarding this burden estimate or any other aspect of this collection of information, including suggestions for reducing the burden, to the Department of Defense, Executive Service Directorate (0704-0188). Respondents should be aware that notwithstanding any other provision of law, no person shall be subject to any penalty for failing to comply with a collection of information if it does not display a currently valid OMB control number.

PLEASE DO NOT RETURN YOUR FORM TO THE ABOVE ORGANIZATION.

1. REPORT DATE (DD-MM-YYYY) 10-12-2008		2. REPORT TYPE FINAL REPORT		3. DATES COVERED (From - To) 1 FEB 2003-29 FEB 2008	
4. TITLE AND SUBTITLE MODELING LIQUID ROCKET ENGINE ATOMIZATION AND SWIRL/COAXIAL INJECTORS				5a. CONTRACT NUMBER	
				5b. GRANT NUMBER F49620-03-1-0025	
				5c. PROGRAM ELEMENT NUMBER	
6. AUTHOR(S) Prof. STEPHEN HEISTER				5d. PROJECT NUMBER	
				5e. TASK NUMBER	
				5f. WORK UNIT NUMBER	
7. PERFORMING ORGANIZATION NAME(S) AND ADDRESS(ES) SCHOOL OF AERONAUTICS AND ASTRONAUTICS PURDUE UNIVERSITY 1282 GRISSOM HALL WEST LAFAYETTE, IN 47907				8. PERFORMING ORGANIZATION REPORT NUMBER	
9. SPONSORING/MONITORING AGENCY NAME(S) AND ADDRESS(ES) AFOSR/NA 875 N. RANDOLPH STREET STE 325 ARLINGTON, VA 22203				10. SPONSOR/MONITOR'S ACRONYM(S) AFOSR	
				11. SPONSOR/MONITOR'S REPORT NUMBER(S) (703) 696-7234	
12. DISTRIBUTION/AVAILABILITY STATEMENT Distribution A: Approved for Public Release					
13. SUPPLEMENTARY NOTES					
14. ABSTRACT This report summarizes efforts to enhance our knowledge of the dynamic processes associated with injectors in liquid rocket engines. Progress has been made on a number of fronts. Linear stability analysis has been performed to assess the wavelengths of instabilities in oxygen rich staged combustion (ORSC) injector elements. Most unstable wavelengths have been characterized over a wide parameter space to provide researchers with an understanding of drop sizes shed from fuel films in these injector elements. The dynamics of classical swirl injectors have been investigated for both single and dual tangential inlet channel designs. The use of multiple inlet channels is believed to lead wave cancellations in the chamber, thereby reducing injector response to perturbations imposed from the combustion chamber. Existing theoretical/linear models have been modified to handle the multi-channel design and show substantial reduction in injector response over a range of frequencies. Companion nonlinear calculations are also in work for both single and dual channel designs. For both cases, it appears that nonlinear effects reduce the overall amplitude of the response as compared to the linear theory.					
15. SUBJECT TERMS					
16. SECURITY CLASSIFICATION OF:			17. LIMITATION OF ABSTRACT U	18. NUMBER OF PAGES	19a. NAME OF RESPONSIBLE PERSON STEPHEN HEISTER
a. REPORT U	b. ABSTRACT U	c. THIS PAGE U			19b. TELEPHONE NUMBER (Include area code) (765) 494-5126

AFOSR Contract F49620-03-1-0025

Modeling Liquid Rocket Engine Atomization and Swirl/Coaxial Injectors

Stephen D. Heister
School of Aeronautics and Astronautics
Purdue University
1282 Grissom Hall
West Lafayette, IN 47907

27 February 2008

Final Technical Report for Period: 1 January, 2002 to 31 December, 2007

Prepared for:
AFOSR, Aerospace and Materials Sciences Directorate
Attn. Dr. Mitat Birkan, Program Manager, Ms. Ilse Espinoza, Contract Manager
875 N. Randolph Street, Rm 3112
Arlington, VA 22203

20090312180

CONTENTS

1	Summary	2
2	Research Objective	4
3	Status of Research	
3.1	Nonlinear dynamics and drop sizes from swirl injectors	5
3.2	Hydrodynamic Modeling of Swirl Injectors with Multiple Rows of Tangential Channels	12
3.3	Boundary Element Method (BEM) Acceleration using ScaLAPACK Utility	16
3.4	Boundary Element Method (BEM) Development and Dynamic Response Studies for Swirl Injectors	20
4	References	26
5	Appendices	
A.	Nonlinear Dynamic Response Modeling of a Swirl Injector	29
B.	Hydrodynamic Modeling of Swirl Injectors with Multiple Rows of Tangential Channels	48
C.	On the Linear Stability of Compound Capillary Jets	63
D.	Modeling Dense Sprays Produced by Pressure-Swirl Atomizer – Model Parallelization	84

1. Summary

This report summarizes efforts to enhance our knowledge of the dynamic processes associated with injectors in liquid rocket engines. Progress has been made on a number of fronts. Linear stability analyses have been performed to assess the wavelengths of instabilities in ox-rich staged combustion (ORSC) injector elements. Most unstable wavelengths have been characterized over a wide parameter space to provide researchers with an understanding of drop sizes shed from fuel films in these injector elements.

The dynamics of classical swirl injectors have been investigated for both single and dual tangential inlet channel designs. The use of multiple inlet channels is believed to lead to wave cancellations in the chamber, thereby reducing injector response to perturbations imposed from the combustion chamber. Existing theoretical/linear models have been modified to handle the multi-channel design and show substantial reduction in injector response over a range of frequencies. Companion nonlinear calculations are also in work for both single and dual channel designs. For both cases, it appears that nonlinear effects reduce overall amplitude of the response as compared to the linear theory.

Work has continued on a comprehensive primary atomization model that relies on no empirical inputs. With recent parallelization of our boundary element codes, we are now able to simulate more and more complex and dense sprays and are able to compute drop statistics (Sauter Mean Diameter) from first principles in a unique nonlinear simulation.

Related work has been conducted in drop splashing as a result of capabilities built up to assess primary atomization physics. Numerous archival publications have resulted from the efforts:

Archival publications (published) during reporting period:

1. Yoon, S. S., and Heister, S. D., "A Nonlinear Atomization Model Based on a Boundary Layer Instability Mechanism," *Physics of Fluids*, V16, No.1, pp. 47-61, 2004.
2. Yoon, S. S., and Heister, S. D., "A Fully Nonlinear Model for Atomization of High-Speed Jets," *Engineering Analysis with Boundary Elements*, V28, pp 345-357, 2004.
3. Yoon, S. S., and Heister, S. D., "Categorizing Linear Theories for Atomizing Jets," *Atomization and Sprays*, V13, pp.499-516, 2003.
4. Kim, B-D, and Heister, S. D., "Two-Phase Modeling of Hydrodynamic Instabilities in Coaxial Injectors," *J. Propulsion and Power*, V20, pp 468-479, 2004.
5. Yoon, S. S., and Heister, S. D., "Analytic Solutions for Computing Velocities Induced from Potential Vortex Ring," *International J. for Numerical Methods in Fluids*, 44:665-672, 2004.
6. Xu, C., Heister, S. D., and Blaisdell, G. A., "Simulation of Cavitated Flow in Orifices Fed by a Manifold," *Atomization and Sprays*, V14, pp 37-52, 2004.
7. Austin, B., Heister, S. D., and Anderson, W. A., "Development of Pintle and Splashplate Injectors for Nontoxic, Storable, Hypergolic Bipropellants," *J. Propulsion and Power*, V21, No.4, pp. 627-635, 2005.

8. Kim, B-D, and Heister, S. D., "Three Dimensional Flow Simulations in Recessed Region of a Coaxial Injector," *J. Propulsion and Power*, V21, No.4, pp. 728-742, 2005.
9. Park, H., Yoon, S.S., and Heister, S.D., "A Nonlinear Atomization Model for Computation of Drop Size Distributions and Spray Simulations", *Intl. J. for Numerical Methods in Fluids*, 48:1219-1240, 2005.
10. Park, H. and Heister, S.D., A Numerical Study of Primary Instability on Viscous High-Speed Jets, *Computers and Fluids*, V35, pp. 1033-1045, 2006.
11. Corpening, J. H., Heister, S. D, and Anderson, W.A., "On the Thermal Decomposition of Hydrogen Peroxide, Part II: Modeling Results", *J. Propulsion & Power*, Vol. 22, No. 5, pp. 996-1005, 2006.
12. Park, H., and Heister, S. D., "Nonlinear Simulation of Free Surfaces and Atomization in Pressure Swirl Atomizers", *Physics of Fluids*, Vol. 18, 052103, 11 pages, May, 2006.
13. Park, H., Yoon, S. S., and Heister, S. D., "On the Nonlinear Stability of a Swirling Liquid Jet", *Intl. J. of Multiphase Flow*, to appear, 2006.
14. Macdonald, M., Canino, J. V., and Heister, S. D., "On the Nonlinear Response of Plain Orifice Injectors", to appear, *AIAA J. Propulsion & Power*, 2007.
15. Park, H., Yoon, S. S., Jepsen, R. A., and Heister, S. D., "Droplet Bounce Simulations and Air Pressure Effects on the Deformation of Pre-Impact Droplets Using a Boundary Element Method", *Engineering Analysis with Boundary Elements*, 2007.

Technology Transfer

The research group at Purdue is supporting a variety of developments throughout the industry. Under NASA sponsorship, models that were initially created in the AFOSR program are being used to assess the forced response of plain orifice "pressure atomizers" under a wide range of conditions. The models are being incorporated into the industry-standard Rocket Combustor Interactive Design (ROCCID) code that is used by NASA MSFC, U.S. Air Force, and numerous propulsion contractors. The models will substantially improve the basic treatment of these atomizers and the Purdue team is working closely with Sierra Engineering on implementation of the new models. Results from current AFOSR-sponsored efforts in the dynamics of swirl injectors has also been transmitted to NASA officials as well as prior simulations of shear coaxial injectors that are of great interest for new Crew Exploration Vehicle propulsion. Our team works closely with small companies including Sierra Engineering and INSpace LLC to provide recommendations on injector designs. We have also provided inputs on gas/gas injectors for potential application to lunar transfer vehicles under sponsorship from entities affiliated with Kistler Aerospace. Currently, we are working on nonlinear dynamics of swirl injectors and hope to be able to create a submodel for ROCCID that would incorporate these results and permit the code to assess a whole new class of injectors. A comparable submodel for shear and swirl coaxial injectors is also under development under NASA sponsorship, although this is a rather low-level effort at present.

2. Research Objectives

The understanding of the complex combustion phenomena present in liquid rocket engines begins with the fundamental process of fuel and oxidizer jet atomization. The objective of this research has been to develop a series of models, incorporating increasingly complex physics, to assess the role of atomization in the combustion instability process. The models have centered on the use of Boundary Element Methods (BEMs) as a means to provide accurate description of these complex, nonlinear processes under arbitrary unsteady conditions. The models have demonstrated a capability to have calculations proceed *beyond* atomization events.

While the basic BEM techniques are inviscid, recent development of a zonal model using an integral method for boundary layer modeling, permits a full viscous capability. This model, described in Appendix A of this report, is the first primary atomization model to provide accurate, fully nonlinear treatment of atomization processes under full-scale Reynolds numbers consistent with actual engine conditions. While these BEM simulations have been useful in describing parent surfaces of modest complexity, other techniques are required to resolve dense sprays formed in many rocket injection processes. For this reason, we have embarked on the development of a viscous, unsteady, nonlinear model capable of addressing flows in which large numbers of droplets are present.

3. Status of Research

3.1 Nonlinear dynamics and drop sizes from swirl injectors

In prior work, we compared nonlinear steady-state computations with the linear theory for a variety of parametric injector designs including the baseline geometry summarized in Table 1. Results were generated for various grids thereby demonstrating convergence and accuracy of the model. These grid tests showed no discernable difference in core radius, film thickness, velocities, and jet half angle, for the meshes studied from $ds = 0.020$ to 0.040 .

Table 1. Assumed Baseline Geometry for Swirl Atomizer Simulations

Radius to Center of Tangential Chn, a_o	= 3.226 mm
Radius of Nozzle, a	= 2.151 mm
Radius of Vortex Chamber, R_v	= 4.234 mm
Radius of Tangential Channel	= 0.643 mm
Length of Tangential Channel	= 1.516 mm
Length of Nozzle, L_n	= 1.500 mm
Length of Vortex Chamber, L_v	= 4.547 mm
No. of Inlet Channels	= 4
Inlet Velocity	= 17.50 m/s

Computed film thicknesses also show excellent agreement with experimental results and limited comparisons of computed drop sizes with measured data show good agreement. A typical number of nodes that evolve for subsequent calculations is 250 nodes with the grid space of $ds = 0.032$ but the number of points increases with time up

to 900 nodes due to increased jet length. In addition, the simulation time for a dynamic response computation takes typically about 2 weeks on the 1.0 GHz Athlon CPU used in the modeling.

The steady-state results show surprisingly little nonlinear effects and the core radius, nozzle exit film thickness, and jet half angle were nearly identical for both the nonlinear calculation and the linear theory for a wide range of designs. The one exception to this result is for nozzles that are short; in this case the linear theory tends to over predict the spray half angle and under predict the film thickness relative to the model calculations. Table 2. shows the extent of agreement between the two BEM calculations (using perturbing inflow velocity and the other using pulsating chamber pressure incorporating Ref. 18 for solution at interior nodes) and the linear theory for the baseline conditions summarized previously. The minor differences between them are attributed to the limitations of the methods employed in calculating these parameters and to the accurate calculation of fluid properties at interior nodes rather than the difference in the specified boundary condition. This is further confirmed, as will be discussed in a later section, by the fact that the change in core radius in the vortex chamber due to fluctuating chamber pressure is negligible compared to the thickness of the liquid film.

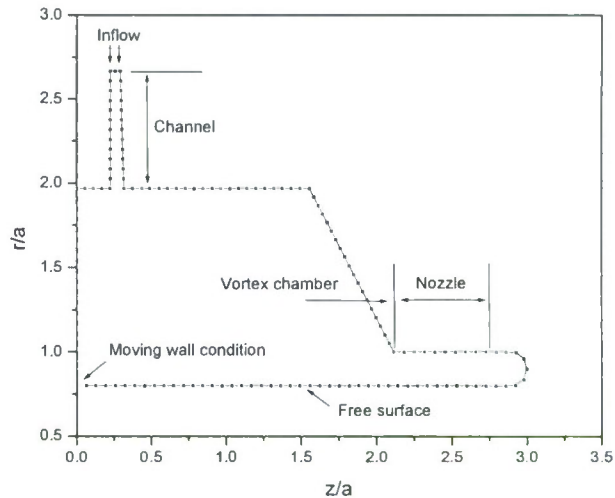


Figure 1. A 2-D axisymmetric grid system used to model a swirl injector.

The minor differences between them are attributed to the limitations of the methods employed in calculating these parameters and to the accurate calculation of fluid properties at interior nodes rather than the difference in the specified boundary condition. This is further confirmed, as will be discussed in a later section, by the fact that the change in core radius in the vortex chamber due to fluctuating chamber pressure is negligible compared to the thickness of the liquid film.

Table 2. Calculated result comparison against the theoretical result of V.G. Bazarov¹⁰

		Theoretical result	BEM (perturbing inflow)	BEM (perturbing chamber pressure)
Core radius (r_a)		0.707	0.705	0.706
Film thickness (h)		0.200	0.205	0.204
Half spray angle		45°	45.5°	45.5°
Total Velocity (m/s)	Nozzle entrance	-	20.7 (at wall) 11.7 (at free surface)	20.5 (at wall) 11.6 (at free surface)
	Nozzle exit	-	24.3 (at wall) 21.0 (at free surface)	24.3 (at wall) 21.03 (at free surface)
	Outside injector	36.09	36.12 ($z = 5.04$, $r = 2.78$)	36.10 ($z = 5.04$, $r = 2.78$)
Axial Velocity (m/s)	Inlet channel	17.50	17.50	17.56
	At nozzle center	17.37	17.45	17.51
	Outside injector	26.26	26.26	26.3

A. Static Characteristics Analysis

The geometry provided in Table 1. served as a baseline condition for the computations. In a steady chamber pressure condition, the radial/axial velocity profiles on both upper and lower fluid surfaces are compared against theoretical values in Fig. 2. Results tend to asymptotically approach the quasi-1-D theoretical values as one moves far away from corners. Figure 3 also shows the free surface shape inside the injector as well as the final jet shape (at $t^* = 12$) with shed droplets. The liquid core evolves naturally as a part of the calculation as does the cone angle formed by the conical sheet exiting the orifice. Under steady flow conditions, the shed droplets are moving in the same direction as the parent jet and their size distribution is almost constant. The computed flow properties for the steady injection case result in an SMD/a of 0.185, and a cone half angle of 46° with other statistical properties summarized in Table 3.

Figure 4 provides a 3-D visualization of the spray evolution and the jet core structure. The breakup length is nearly constant after $t^* = 5.0$ and shed droplets are tracked downstream with the direction angle of the parent jet. The overall spray is qualitatively similar with that of actual experimental images.¹⁶ The initial ligament pinching events lead to droplets that are dispersed somewhat from the final cone angle formed by the spray. This is an artifact of the initial conditions selected for the simulation and not necessarily representative of the chaotic startup observed during the chamber filling process of a real device.

Table 3. Statistical properties for a swirl injector

	Properties
SMD/a	0.185
N_D	1741
D_D/a	0.198
\bar{u}_D/U	1.21
\bar{v}_D/U	1.26
θ_D (°)	45.8

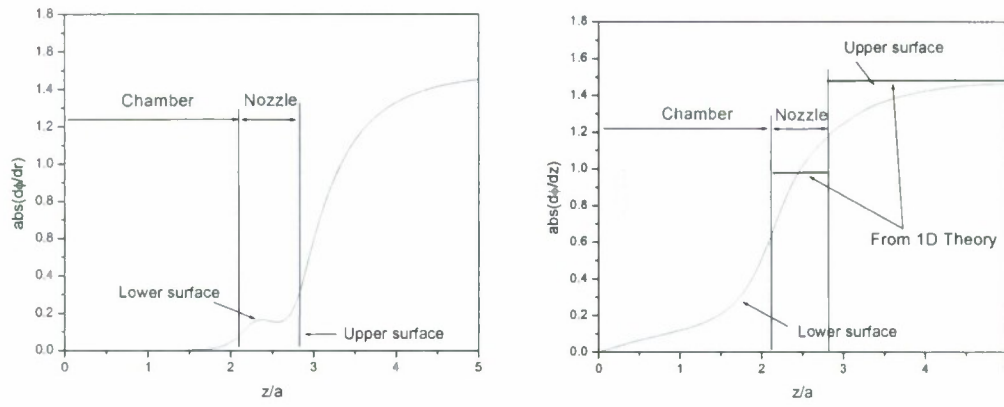


Figure 2. Radial (left) and axial (right) velocity profile along fluid surface in a classical swirl injector.

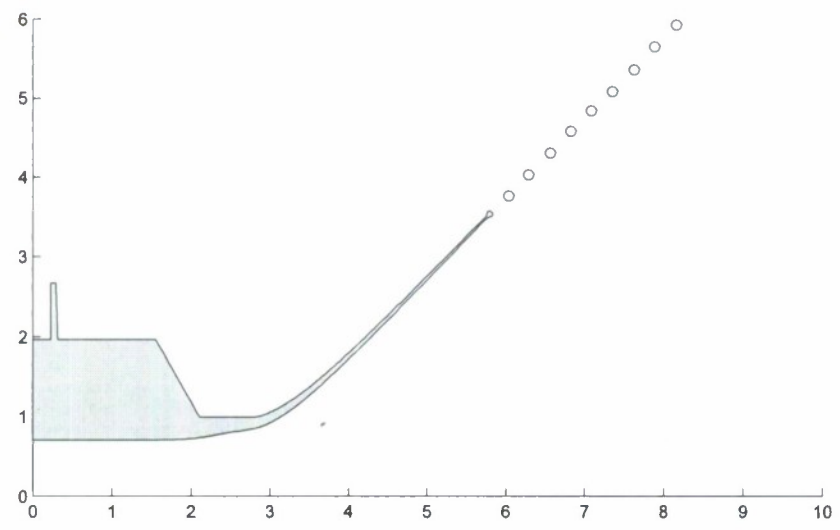


Figure 3. Final jet shape showing shed droplets for baseline swirl injector, at $t^* = 12.0$.

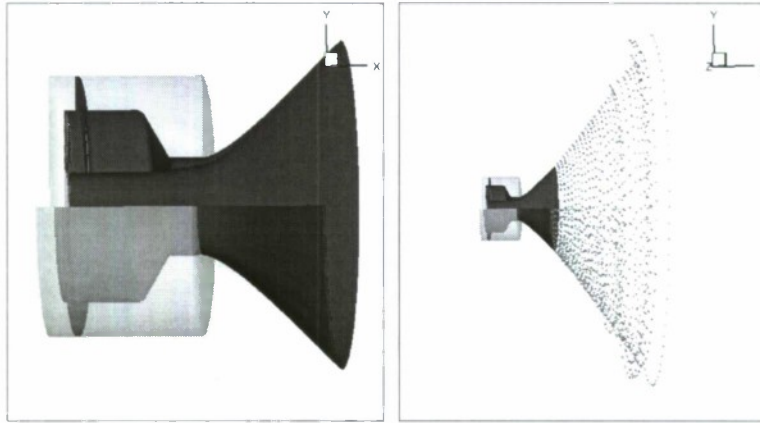


Figure 4. Dimensional view of the final jet shape computed for baseline conditions noted in Table 1

B. Behavior under Dynamic Injection

The dynamic response was studied for the injector geometry described in Table 1. at the baseline injection velocity and pressure drop of 17.5 m/s and 0.69 MPa respectively. To compare results against the theoretical analysis of Bazarov & Yang,² the velocity was interrogated at a variety of locations in the film. Figure 5 shows locations for dynamic response analysis in our calculation. The detailed locations are as follows:

Pt 1: U_{inp} :	$z = 0.258,$	$r = 2.665$	(at the channel inlet)
Pt 2: U_{chamb} :	$z = 1.495,$	$r = 1.968$	(at the chamber wall)
Pt 3: $U_{noz,entr}$:	$z = 2.113,$	$r = 1.000$	(at the wall of nozzle entrance)
Pt 4: $U_{noz,exit}$:	$z = 2.798,$	$r = 1.000$	(at the wall of nozzle exit)
Pt 5: U_{out} :	$z = 5.036,$	$r = 2.789$	(outside the nozzle)

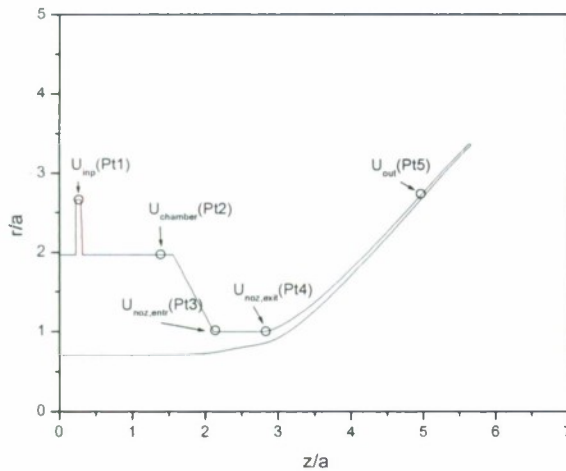


Figure 5. Selected locations for dynamic response analysis in a classical swirl injector.

variations, while the former approach is more representative for feed system based oscillations.

Two distinct approaches have been used for simulation of unsteady flow conditions. Initially, we utilized a forced excitation via oscillation of the inlet massflow. Since the dynamics of the film thickness in the vortex chamber could lead to large amplitude surface waves, this process can in principle give results substantially different from the case where the gas pressure in the vortex chamber was oscillating in time. For this reason, a second approach was also investigated wherein the oscillation was imposed via an unsteady pressure in the vortex chamber. This latter approach is more realistic for dynamics induced by combustion chamber pressure

1. Dynamic Massflow Simulations

The dimensionless time in the computational domain is $t' = U/a \cdot t$, so the dimensionless oscillation wave number (ϖ') for actual oscillation frequency (f) is as follows:

$$\varpi' = \frac{a}{U} \varpi = \frac{a}{U} 2\pi f = \frac{2.151E-3}{17.5} \times 2\pi \times f = 7.7229E-4 \times f \quad (3.1)$$

Then, for a given input oscillation frequency, the injection velocity is pulsation can be written:

$$F(\varpi') = A \sin(\varpi' t') \quad (3.2)$$

where A is the amplitude of the massflow pulsation. In our study, the disturbance is prescribed as a fluctuation of the inflow velocity in the tangential channel, Eq. (3.2), or as perturbation of chamber pressure as seen in Eq. (3.3).

$$\Delta P = \Delta P_{\text{Steady}} + \varepsilon \sin(\omega t) \quad (3.3)$$

In addition, the inlet for the tangential channel is assumed as the circular cylinder in our axisymmetric simulation and its area is determined to have the same mass flow rate with the actual injector. In order to keep the constant area for the same mass flow rate throughout the tangential channel, the channel width at the tip and the root can be calculated:

$$W_{T,tip} = \frac{R_v}{R_v + L_T} W_{T,root}, \text{ where } W_{T,root} = \frac{4R_T^2}{2R_v} \quad (3.4)$$

2. Dynamic Chamber Pressure Simulations

Here, the unsteady pressure drop across the film in the vortex chamber must be ascertained in order to determine the instantaneous pressure drop across the tangential channels. From the radial momentum equation, $\frac{V_\theta'^2}{R} = \frac{1}{\rho'} \frac{\partial p'}{\partial R'}$, where for the potential vortex: $V_\theta' = \frac{\Gamma}{2\pi R'}$. After integration, the dimensional pressure drop across the liquid film can be computed:

$$\Delta P_1' = -\frac{\rho' \Gamma'^2}{8\pi^2} \left(\frac{1}{R_{in}^2} - \frac{1}{R_C^2} \right) \quad (3.5)$$

So that the nondimensional pressure drop can be written:

$$\Delta P_1 = -\frac{\Gamma^2}{8\pi^2} \left(\frac{1}{R_{in}^2} - \frac{1}{R_C^2} \right) \quad (3.6)$$

Substituting nondimensional circulation $\Gamma = 2\pi R_{in} V_\theta = 2\pi R_{in} V_{in}$ we obtain:

$$\Delta P_1 = -\frac{R_{in}^2 V_{in}^2}{2} \left(\frac{1}{R_{in}^2} - \frac{1}{R_C^2} \right) = \frac{V_{in}^2}{2} \left(\frac{R_{in}^2}{R_C^2} - 1 \right) \quad (3.7)$$

Assuming a constant stagnation pressure in the manifold and neglecting viscosity losses, Bernoulli's equation gives the pressure drop across the inlet channel: $\Delta P_2 = \frac{V_\theta^2}{2}$.

So the total pressure drop across the injector is the sum of pressure drops across the liquid film and inlet channel:

$$\Delta P = \Delta P_1 = \Delta P_2 = \frac{V_{in}^2 R_{in}^2}{2 R_C^2} \quad (3.8)$$

Knowing this pressure drop the inflow velocity can be computed as:

$$V_{in} = \sqrt{2\Delta P} \frac{R_C}{R_{in}} \quad (3.9)$$

Where the overall pressure drop in the system is assumed to be a sinusoidal function of time $\Delta P = \Delta P_{Steady} + \varepsilon \sin(\omega t)$. The steady state pressure drop is calculated from the initial conditions:

$$\Delta P_{Steady} = \frac{q_{mean}^2 R_{in}^2}{2R_{CSteady}^2} \quad (3.10)$$

Figure 2 shows a typical computational grid employed in the studies. The initial pressure drop is computed from Eq. (3.1) based on the steady state solution for the core radius using constant inflow rate. This pressure drop plus perturbation is further converted to massflow on the inlet boundary using Eq. (3.2).

C. Simulations Assuming Forced Mass Flow Pulsations

A series of simulations were conducted using the unsteady massflow methodology outlined in Eqs. (3.1)–(3.4). An initial simulation was performed with a 10% massflow fluctuation ($A = 0.1$) at a frequency of 5000 Hz. At lower frequencies, the dynamic simulation can require long integration times in order to build up statistical properties for drop sizing. In order to save computational cost, this simulation was restarted from the steady state solution obtained at the time of $t^* = 5.0$ and integrated in time until quasi-periodic behavior was obtained. The input and nozzle exit velocity histories are overlaid for the period $10 < t^* < 20$ in Fig. 6. The phase lag and amplitude modulation of the input signal is evident from this comparison.

The dynamic response for a single cycle of the imposed oscillation is depicted at various points in the injector in Fig. 7. The unsteady part of the signal is plotted at each location in order to assess wave amplitude and phase shifts at various points in the flow path. In Fig. 7, the oscillation frequency and the amplitude, for the plot on the left, were set as $f = 5000$ Hz and $A = 0.1$, respectively. The vortex chamber acts as an accumulator and changes in massflow cause very little variations in velocity at Pt. 2; the massflow variations lead to changes in the size of the vortex core in this region. At Pt. 3 (nozzle inlet), a very large lag is notable and the amplitude of the oscillation increases as the fluid accelerates into the contraction region. At the nozzle exit, the oscillation amplitude is diminished somewhat as the swirl velocity is increased. The signal actually appears to be leading the input at this location for the conditions studied—this unusual characteristic is unique to swirl injectors with large vortex chambers that can cause large lags in response. The amplitude of the signal is attenuated further at the nozzle exit and into the conical film with smaller phase lags noted in these regions due to the relatively shorter flow times characteristic of the nozzle and regions downstream.

The right plot of Fig. 7 shows the dynamic response for $f = 1000$ Hz and $A = 0.1$. At this lower frequency, the response lags the input much more modestly, and the overall trends in amplitude are preserved from the 5000 Hz case. As the flow times are more comparable to the oscillation period in this case, the overall lag of the injector is much more modest.

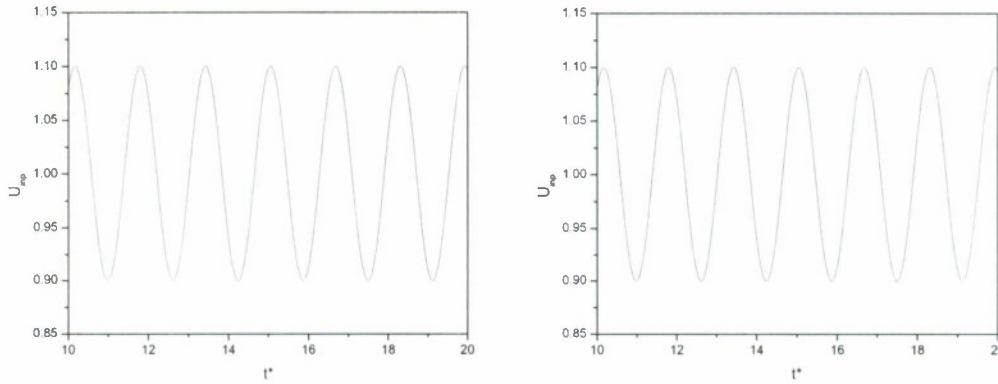


Figure 6. Raw input (left) and response (right) for initially disturbed inflow velocity; the oscillation frequency and the amplitude were set as $f = 5000$ Hz and $A = 0.1$, respectively.

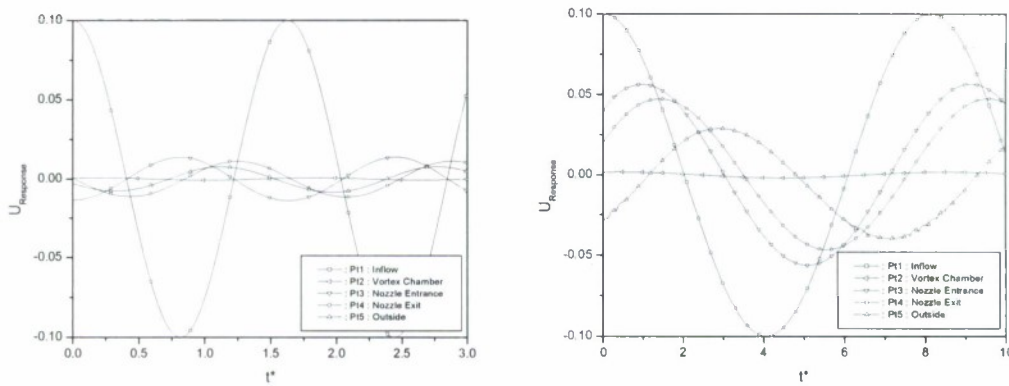


Figure 7. Dynamic response through a classical swirl injector, which was investigated in velocity response; the oscillation frequency and the amplitude where set as $f = 5000$ Hz, $A = 0.1$ (left), and $f = 1000$ Hz, $A = 0.1$ (right), respectively.

3.2 Hydrodynamic Modeling of Swirl Injectors with Multiple Rows of Tangential Channels

Modified model for dual channel injector

Consider a swirl injector with two rows of tangential injectors separated from each other by a distance L_x (Figure 8). We assume that the response of the tangential channels and nozzle are unchanged (with respect to single row of inlets) with the introduction of another row of inlet. Also the any modification needed due to the 'vorticity' effect in the vortex chamber is neglected as it is found to be negligible. However the interaction of the surface waves in the vortex chamber has to be accounted for. See Richardson⁴⁰ for a detailed analysis of a two channel swirl injector.

The phase shift associated with the distance between the two inlet channels L_x is given by,

$$\phi_x = \frac{\omega L_x}{V'_{wv}} \quad (3.11)$$

Where angular velocity, $\omega = 2\pi f$ and V'_{wv} is the wave velocity in the vortex chamber.

We can use the principle of superposition to examine the influence of reflected waves in the vortex chamber of any arbitrary length. Let us consider an initial wave in the vortex chamber at inlet 'a' given by

$$\xi_{vh_1} = \Lambda_a e^{i\omega t} \quad (3.12)$$

Where Λ_a is the initial height of the wave due to the perturbation in the inlet 'a'. Near the nozzle this wave travels a distance of L'_v (length of Vortex Chamber) and becomes,

$$\xi_{vm_1} = \Lambda_a e^{i(\omega t - \phi_v) - \nu\phi_v} \quad (3.13)$$

Where ϕ_v the shift angle is associated with traveling L'_v distance and $\nu\phi_v$ is the reduction in the amplitude due to viscosity ν . A part of this wave gets reflected which is given by,

$$\left(\xi_r\right)_{vm_1} = \Pi \Lambda_a e^{i(\omega t - \phi_v) - \nu\phi_v} \quad (3.14)$$

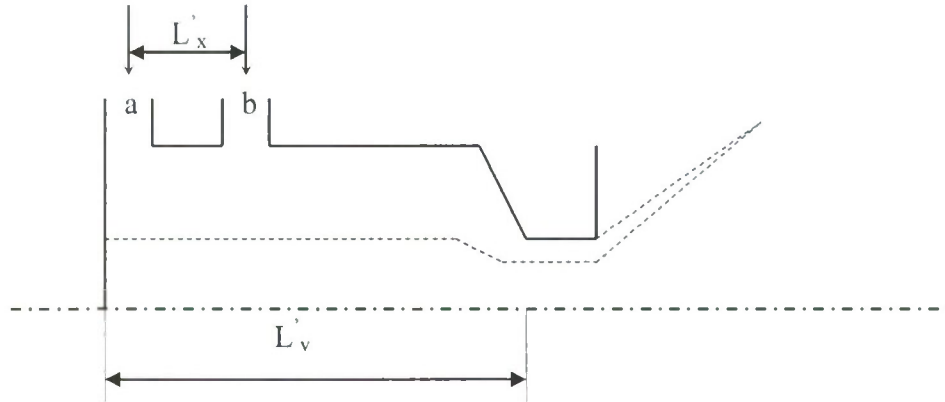


Figure 8. A classical swirl injector with two inlets at locations 'a' & 'b' separated by a distance L_x

Where Π is the reflection coefficient. This reflected wave changes in the following manner when it travels a length L'_v to reach the closed end of the Vortex Chamber

$$\xi_{vh_2} = \Pi \Lambda_a e^{i(\omega t - 2\phi_v) - \nu 2\phi_v} \quad (3.15)$$

This wave is reflected completely from the closed end and reaches the nozzle,

$$\xi_{vm_2} = \Pi \Lambda_a e^{i(\omega t - 3\phi_v) - \nu 3\phi_v} \quad (3.16)$$

The reflected wave will be,

$$(\xi_r)_{vm_2} = \Pi^2 \Lambda_1 e^{i(\omega t - 3\phi_v) - \nu 3\phi_v} \quad (3.17)$$

And so the waves reflect back and forth until their amplitudes become negligibly small.

Using the principle of superposition we have the following wave near the closed end of the vortex chamber,

$$\xi_{vh} = \Lambda_a \sum_{n=0}^{\infty} \Pi^n e^{i(\omega t - 2n\phi_v) - 2n\nu\phi_v} \quad (3.18)$$

Near the nozzle,

$$\xi_{vn} = \Lambda_a \sum_{n=0}^{\infty} \Pi^n e^{i(\omega t - (2n+1)\phi_v) - (2n+1)\nu\phi_v} \quad (3.19)$$

Similarly we can derive equations for surface waves in the vortex chamber due to the perturbations in the inlet channel 'b'.

Then, using the principle of superimposition we can compute the wave near the head end of vortex chamber as follows

$$\xi_{vh} = \Lambda_a \sum_{n=0}^{\infty} \Pi^n e^{i(\omega t - 2n\phi_v) - 2n\nu\phi_v} + \Lambda_b \sum_{n=0}^{\infty} \Pi^n e^{i(\omega t - 2n\phi_v + \phi_x) - 2n\nu\phi_v + \nu\phi_x} \quad (3.20)$$

Similarly near the nozzle inlet we have

$$\xi_{vn} = \Lambda_a \sum_{n=0}^{\infty} \Pi^n e^{i(\omega t - (2n+1)\phi_v) - 2n\nu\phi_v} + \Lambda_b \sum_{n=0}^{\infty} \Pi^n e^{i(\omega t - (2n+1)\phi_v + \phi_x) - (2n+1)\nu\phi_v + \nu\phi_x} \quad (3.21)$$

The above two equations are used in computing the response of the dual channel injector.

A dual channel swirl injector was analyzed using the modified linear model and compared with computational results generated by BEM code described in section II using oscillation pressure boundary conditions. An injector currently being tested by Miller⁴¹ at Purdue University was used as basis for this study (Table 4).

Inlet radius of tangential channel	$R'_{in} = 0.454$ in
Radius of nozzle	$R'_n = 0.454$ in
Radius of vortex chamber	$R'_v = 0.454$ in
Radius of tangential channel	$R'_T = 0.0175$ in
Length of tangential channel	$L'_T = 0.359$ in
Length of nozzle	$L'_n = 0.0$ in
Length of vortex chamber	$L'_v = 0.4767$ in
Length between two channels	$L'_x = 0.0999$ in
No of inlet channels	$n = 8$
Inlet velocity	$V'_T = 913$ in/s

Table 4. Design parameters of a dual channel swirl injector

Since the injector to be analyzed is an ‘open’ injector that is the radius of vortex chamber and nozzle being equal further modification where required to the existing model. The effect due to reflection coefficient Π was eliminated (set to a very small value) and the nozzle length was set to an insignificant value. The flow was shared equally among both the inlet channels.

The linear model shows a local minima around 1344 Hz (Figure 9,10). This frequency corresponds to the distance between the two inlets $L_x = 0.1$ in. The amplitude of response is never greater than unity; this is a feature of the ‘open’ injector which makes it more attractive

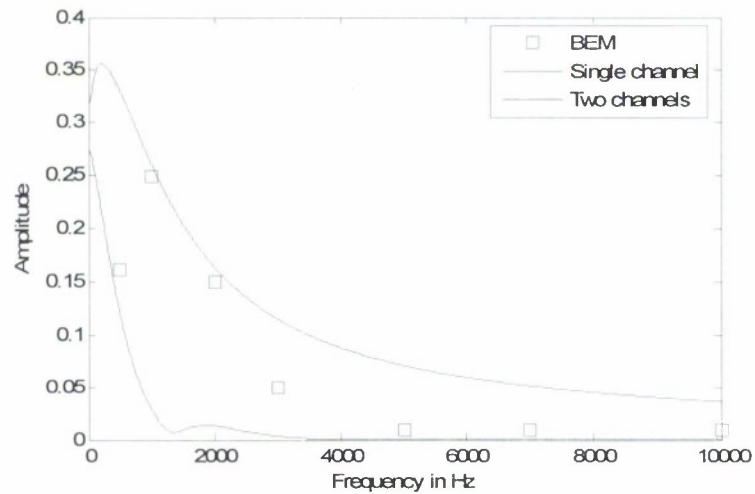


Figure 9. Amplitude vs Frequency for dual channel swirl injector

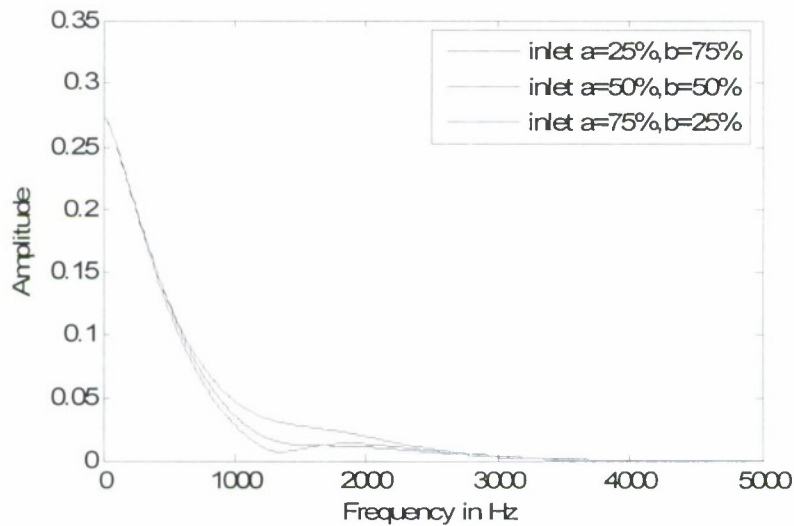


Figure 10. Amplitude vs frequency for different combinations of flow through the two sets of inlets

option over the ‘classical’ swirl injector. The dual channel injector is much more stable than the single inlet design due to the destructive interference of the surface waves in the vortex chamber. The computational results seem bounded by the single and dual channel analytical

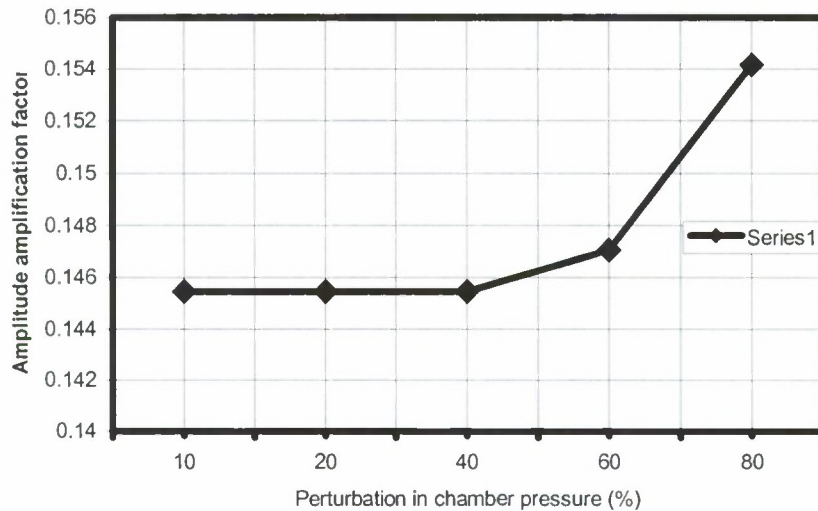


Figure 11. Amplitude vs perturbation

analysis for the same design parameters.

At low frequencies (< 1000 Hz) the interference of surface waves is more prominent owing to longer wavelengths and fewer waves in the vortex chamber. However at higher frequencies the computational model shows a diminishing effect of the two channel inlet probably due to decreasing wavelengths of the surface waves and probably the simple dual channel analysis seems inadequate to capture all the phenomena in the vortex chamber. Also the non-linear effects are not being accounted for in the theoretical model.

The amount of mass flow rate (Fig. 10) was varied among the two sets of inlets. A 50-50 split shows to be the most stable combination with clear local minima at 1344 Hz. Other combinations are a little less stable than the 50-50 split and also don't show any clear local minima.

Fig. 11 shows BEM results for amplitude amplification factor (ratio of outflow to inflow perturbation magnitudes) as a function of chamber pressure perturbations for the frequency of 2000 Hz. As we can see even 80% perturbation causes nonlinearity of just above 5%.

3.3 Boundary Element Method (BEM) Acceleration using ScaLAPACK Utility

Assuming the Runge-Kutta time integration scheme, the BEM calculation requires the solution of the large-dense system of linear equations for four times at every time step. Computational cost on solving this matrix system is fairly expensive. Current BEM codes developed within the research group have used LU decomposition and SOR(Successive Over Relaxation) to solve the large-dense matrix system. Although SOR has been a quite successive method for solving larger matrix systems(over 1000 nodes), it has not been fast enough to get the grid convergence for high Weber number jets. A small Δs (grid size) has been required to ensure the exactitude of computation in this case, so that computational cost of BEM based on SOR has been quite high. Therefore, it has been necessary to modify the matrix system solver in BEM.

The fully populated square matrix gives BEM codes a unique characteristic compared to the banded structure present in classical CFD codes. Classical CFD codes usually accomplish the acceleration by the use of sparse matrix inversion schemes and parallelization; dividing the computational domain into smaller matrices that are distributed to a set of CPUs. In addition, BEM atomization problems are distinguished by computational domains that increase with time, which yields different size matrix system at every time step. In addition, BEM matrices for fluids problems of this nature are generally poorly conditioned, i.e. not diagonally dominant, thereby further complicating inversion processes. These issues make the matrix inversion in BEM fluids codes quite challenging. To improve performance of current codes, the ScaLAPACK utility was investigated as an aspect of the current work.

Scalable Linear Algebra Package (ScaLAPACK) is a set of library for distributed memory MIMD(Multiple Instruction stream, Multiple Data stream) parallel computers developed by the ScaLAPACK project⁴². ScaLAPACK provides routines for dense and band system of linear equations, linear least squares problems, and eigenvalue and singular value problems. The large-dense matrix system solver in ScaLAPACK implies Block and Parallel LU Factorization; blocked submatrices from original matrix are distributed to a set of CPUs and then solved by LU Factorization. ScaLAPACK accelerates BEM significantly and finally shows a good grid convergence for SMD(Sauter Mean Diameter).

The test for the comparison of ScaLAPACK and prior successive overrelaxation(SOR) methodologies have been completed. The acceleration obtained by ScaLAPACK relative to SOR is shown in Fig. 12. This test is done for matrix systems obtained by test-run of BEM code on our current HPC(High Performance Computing) cluster which has 2.4 GHz AMD Opteron Quad Processors onevery computational node. As ScaLAPACK project suggests that the maximum performance is achieved when 1000x1000 matrix is set on one CPU, 1000x1000 matrix system is solved most rapidly on 1x1 CPU. 2000x2000 matrix system shows best performance on 2x2 CPUs(total 4 CPUs). BEM often yields a matrix over 2000x2000 so that it is expected that ScaLAPACK will significant advantages over SOR for very large problems.

The time taken to run the entire code using ScaLAPACK has been compared to code using SOR. The run time of BEM code for the simulation of Rizk and Lefebvre's experiment⁴³ is shown in Fig. 13. When Δs is 0.016, BEM based on ScaLAPACK takes 13.2 days but BEM based on SOR can not simulate the case due to computational constraints. Therefore, it has been confirmed that relatively large grid cases can be simulated within a short time relative to SOR with the aid of ScaLAPACK and small grid cases which can not be simulated by SOR can be simulated using ScaLAPACK. Figure 14 demonstrates convergence of the scheme for conditions consistent with Rizk and Lefebvre's experiments⁴³. Prior simulations with SOR could not get the grid convergence for SMD due to exhorbitant run times.

Using Ponstein's linear analysis for a rotating column, rings pinched from an axisymmetric computation can be fractionated into droplets to provide a quasi-3-D simulation of a spray. Limited prior work has shown some success using this approach with modest grid sizes. Figure 15 and 16 depicts some current simulations using the methodology. In the image on the right of Fig. 15, over 23,000 drops are produced. Approximately 80,000 drops are produced in the current simulation of Cousin *et al's* experiments⁴⁴, 3D visualization of this simulation is presented in Fig. 16.

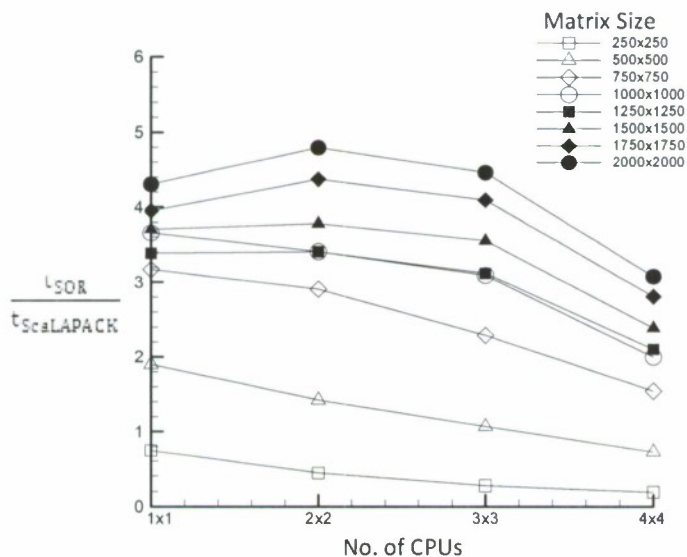


Figure 12. Acceleration by ScaLAPACK for various matrix sizes with various number of CPUs (t_{SOR} is time taken by SOR, $t_{ScaLAPACK}$ is time taken by ScaLAPACK)

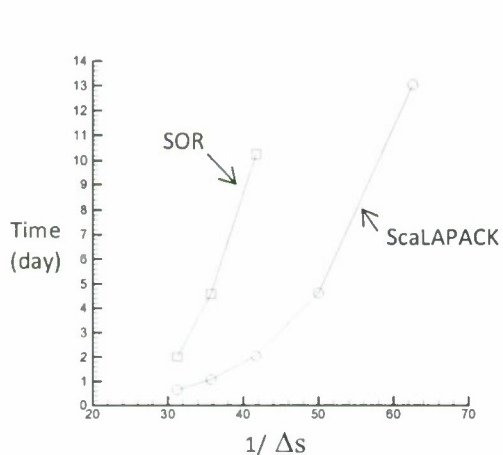


Figure 13. Run time of code for SOR and ScaLAPACK with various grid size (from $t=0$ to 10s)

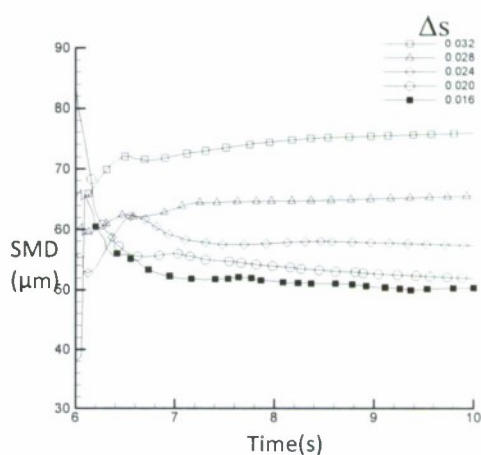
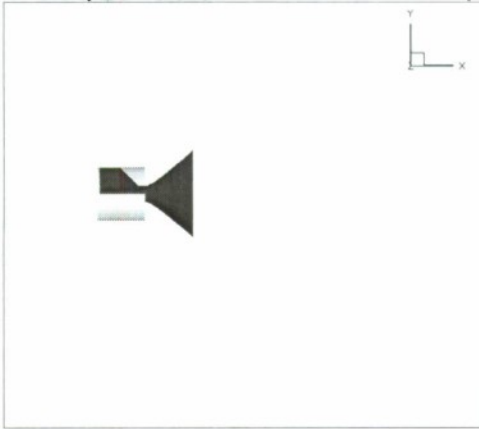
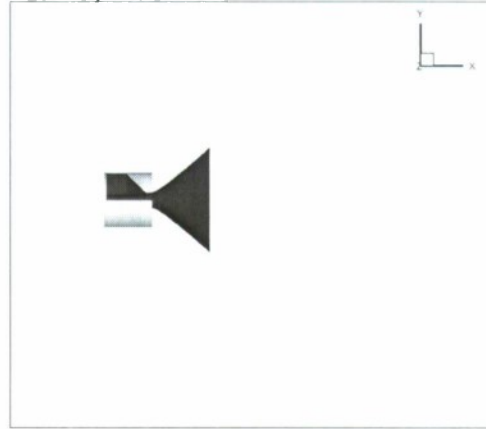


Figure 14. SMD for various grid sizes with time

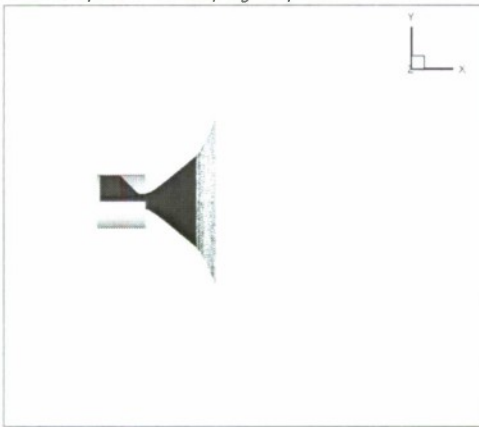
$t = 5.0 \text{ s}, \Delta s = 0.028$



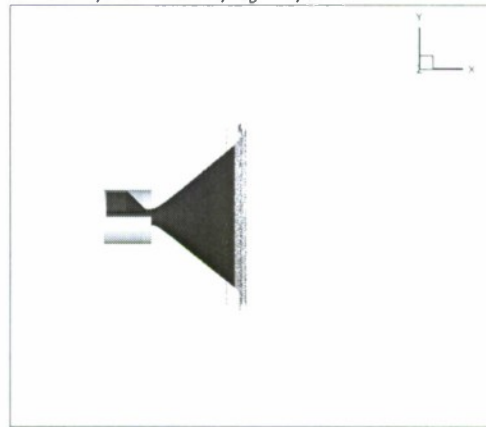
$t = 5.0 \text{ s}, \Delta s = 0.016$



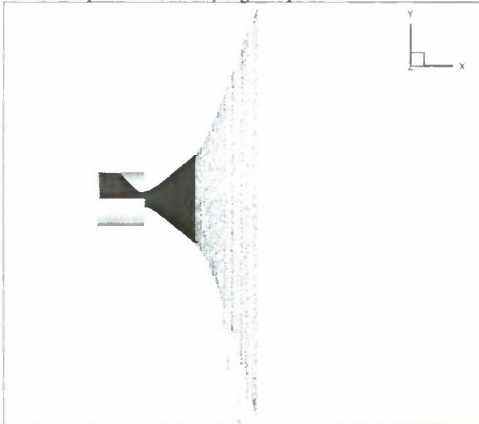
$t = 7.0 \text{ s}, \Delta s = 0.028, N_D \approx 2,700$



$t = 7.0 \text{ s}, \Delta s = 0.016, N_D \approx 5,400$



$t = 9.0 \text{ s}, \Delta s = 0.028, N_D \approx 8,300$



$t = 9.0 \text{ s}, \Delta s = 0.016, N_D \approx 23,200$

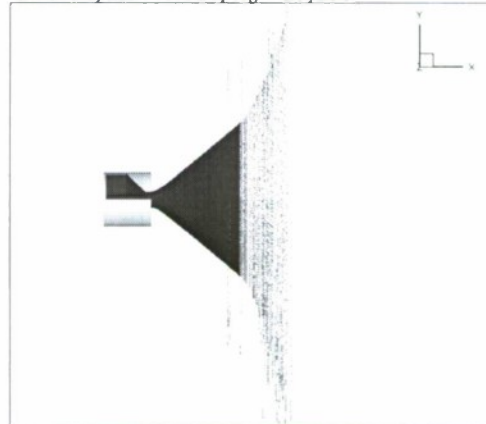


Figure 15. Variation of the flow field with time, comparison between two cases; the left is for $\Delta s = 0.028$ and the right is for $\Delta s = 0.016$ (N_D is the number of drops, Drops produced after the flow field is fully developed are only included in this figure.)

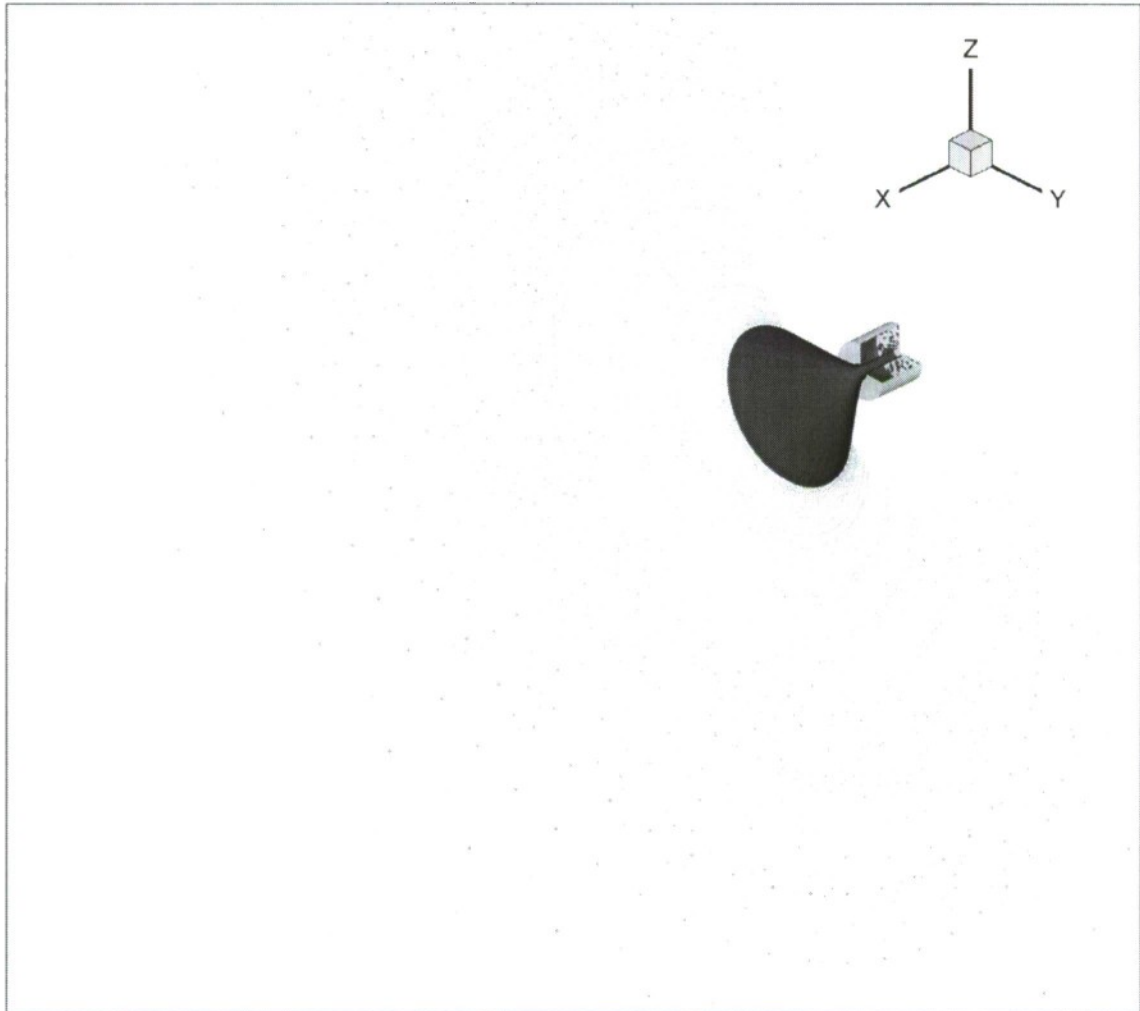


Figure 16. 3D visualization of the simulation of Cousin et al's Injector #04 ($t=10s$, $\Delta s = 0.016$, $N_D \approx 80,000$, The whole drops produced in the simulation are included in this figure.)

3.4 Boundary Element Method (BEM) Development and Dynamic Response Studies for Swirl Injectors

Under AFOSR sponsorship, we are performing boundary element simulations to determine the nonlinear dynamic response of swirl injectors utilized in many liquid engine systems. Highly compute-intensive work is ongoing to determine injector massflow response (amplitude and phase) over a wide range of pulsation conditions and orifice geometries.

This year's work was focused on the analytical revision of existing codes computing the dynamic response of swirl injectors of a typical design shown on Figure 17.

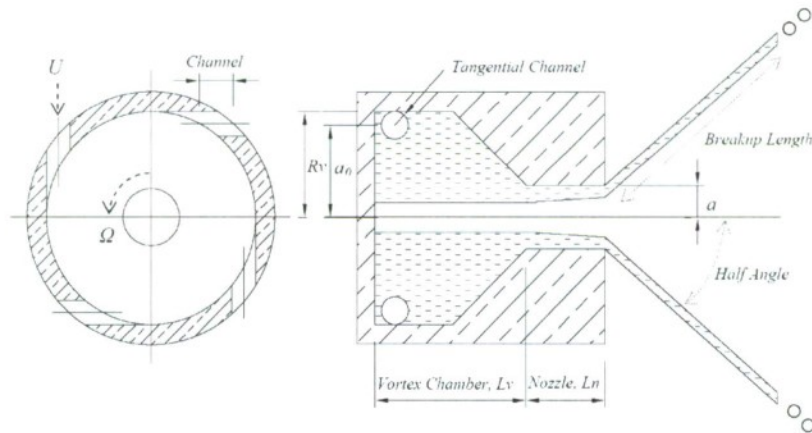


Figure 17. A classical swirl injector noting nomenclature used for design variables

Since no experimental evidence exists on how the pulsations of mass flow rate at the injector inlet or of the combustion chamber gas pressure correlate with the pulsations of mass flow rate at the exit orifice, work by Bazarov² is used as the only available reference for validation of BEM results. Bazarov's theory is linear and is based on the assumptions that the flow has essentially a free vortex distribution of tangential velocities, is incompressible and inviscid. It predicts that two types of waves should exist on the vortex free surface. The first type results from the fact the film adjusts its thickness to accommodate the fluctuating incoming mass of liquid. The second type results from the idea that as the inlet velocity or the back pressure is changed, the different layers of liquid start to rotate with different speeds. The centrifugal forces associated with this process cause the slower moving particles to move towards the vortex core surface and the faster ones to the walls, which generates the so called vorticity waves. Both types of waves propagate within the vortex chamber on the core surface and get refracted back and forth by the head end and contraction section walls of the vortex chamber, see Figure 19. Studies have shown that the vorticity waves have much stronger effect on the dynamic response than the first type of waves². A corresponding linear code⁴⁰ had been in use which incorporated the equations of the linear theory. Two types of injectors are being investigated: single channel, Figure 17, and dual channel, Figure 19.

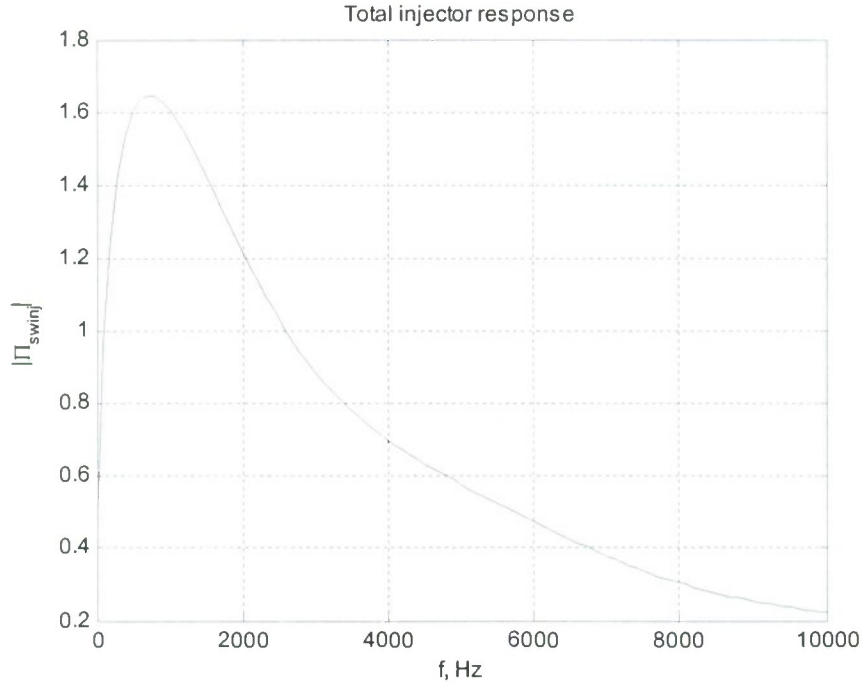


Figure 18. Single channel swirl injector dynamic response due to linear theory.

A typical correlation between inlet and exit flow pulsations produced by linear code for a single channel injector is shown on Figure 18. Here the response is presented as a transfer function

$$\Pi_{swinj} = \frac{Q_n' / Q_n}{p_c' / p_c} \quad (3.22)$$

where Q_n is the average mass flow rate at the exit orifice, p_c is the average combustion chamber gas pressure and primes denote the fluctuation of these quantities given by

$$[]' = \frac{\max[] - \min[]}{2} \quad (3.23)$$

According to the linear theory, in the situation when two inlet channels are present, some distance apart, the vorticity waves generated by both inlets, start to interact, causing the injector response to have minimums at certain frequencies of flow disturbances⁴⁰. This phenomena occurs due to cancellation of the waves which are moving in opposite directions and phases, see Figure 19. The response compared to the response calculated by the BEM code showed that the minimums do not match. A typical comparison for the dual channel response for the case when chamber gas pressure is being pulsated within 37% from its average value is shown in Figure 20.

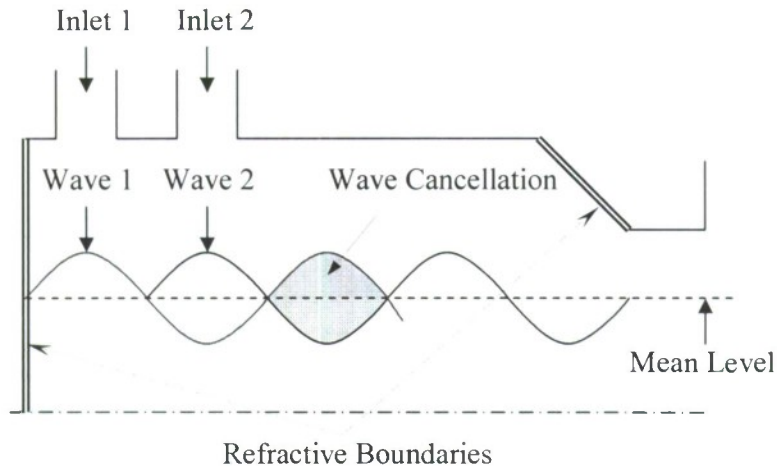


Figure 19. Dual channel injector schematic.

Most recent studies have been done to find the reason for this mismatch. Several minor problems were found in the linear code, for example, some nondimensional parameters were used as dimensional, etc.. Furthermore, the graphical dual channel BEM results depicting the instantaneous axial and radial coordinates of the points on vortex surface, did not show any apparent occurrence of the surface waves. As disturbance frequencies varied, the surface came to a steady flat form, similar to the static one shown on Figure 17, or close to the mean level shown on Figure 19.

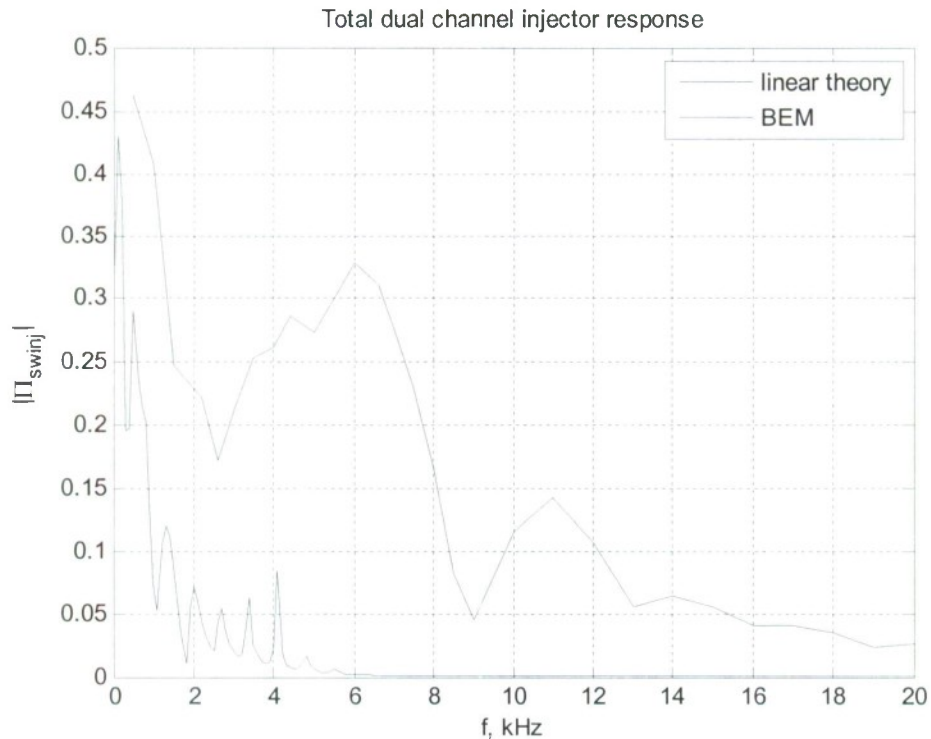


Figure 20. Dual channel response comparison between BEM and linear theory.

In order to check if the code is responding accurately to small discrete changes of inflow conditions, a test was conducted where the inlet velocity was changed in the form of a single

pulse. Figure 21 shows the flow development consisting of the transient, steady and pulsed parts in terms of inlet and exit mass flow rates. The zoomed in picture of the pulse shows that the nozzle exit disturbance is much smaller compared to the inlet one. This also implicitly tells us that the amplitude of surface waves on the vortex core stays negligibly low.

Therefore, the initial single channel version of the BEM code was revised to investigate the governing equations, with particular focus on the Bernoulli's equation, Table 5, which serves as dynamic boundary condition on the liquid-gas interface.

One of the reasons for the decrease of surface wave amplitude is the artificial viscosity, given by all terms having u_v and v_v . In previous versions of BEM code computing non-swirling flows the viscosity was modelled by means of superposing a potential vortex ring on a uniform flow of liquid column⁴⁵. In the current version the viscous terms are still present in exactly same form. But since the flow is swirling then the way for modelling the viscosity should also be revised.

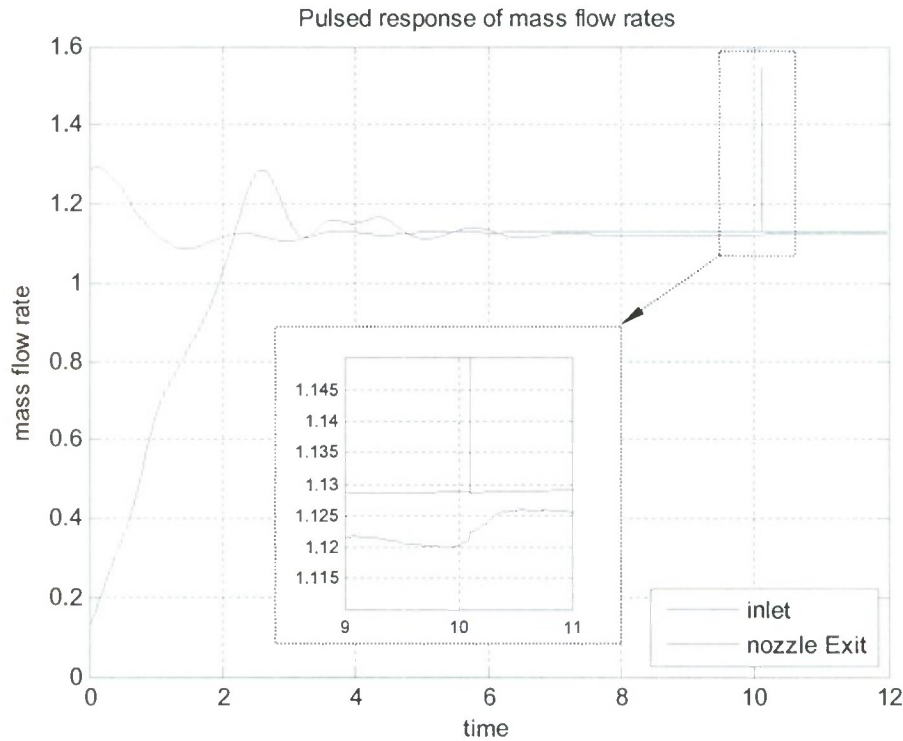


Figure 21. Inlet and exit mass flow rate responses to the pulsed inflow.

Another reason for small amplitude of surface waves is related to the main term responsible for the rotation of liquid given by

$$-\frac{1}{2} \left(\frac{a_0^2 \Omega_0}{r} \right)^2, \quad (3.24)$$

where a_0 is the distance from injector axis to the inlet channel axis, Ω_0 is the angular velocity at a_0 and r is any other radius. Here the angular velocity is computed as

$$\Omega_0 = \frac{U_{in}(t)}{a_0}, \quad (3.25)$$

where $U_{in}(t)$ is the current inlet velocity. This means that as inlet velocity is changed, every infinitesimal slice or disk of liquid perpendicular to the injector axis has same angular velocity Ω_0 at a_0 , which causes equal free vortex tangential velocity distribution for all of them, see Figure 22. This corresponds to the situation when the whole liquid body would respond instantaneously to the change of inflow conditions. Since radial velocities are much lower than tangential or axial ones in a swirl injector flow, then any disturbance of the inlet velocity affects either tangential or axial velocities on the vortex surface. Also, the small magnitude of radial velocities leads to the situation that the points on the vortex core have approximately same radial positions and therefore, the same tangential velocity, due to previous reasoning. Then, in this case, the disturbance of the inlet velocity could result only in the the change of axial velocities of surface points, which also visually leads to the absence of waves.

In reality, considering the flow is close to inviscid, each particular disk should have its own unique tangential velocity distribution which corresponds to the inlet velocity existed at the instant of time when this slice was right at the inlet, or a remembered inlet velocity. And each of these disks should retain its tangential velocity distribution as it moves from inlet area to the exit, see Figure 22.

Conclusively, to address these issues, the current single channel BEM code is being modified in such a way that the viscous effects are removed, and the liquid vortex is modeled as a collection of disks, each having its own tangential velocity distribution.

$\frac{D\phi}{Dt} =$	$\frac{1}{2} \left[\left(\frac{\partial\phi}{\partial z} + u_v \right)^2 + \left(\frac{\partial\phi}{\partial r} + v_v \right)^2 \right]$ <p>This is $\frac{1}{2}(u^2 + v^2)$ part in [24, eq.(4.12)], where u_v and v_v terms come from viscous vortex ring treatment [23, eqs.(3.55)].</p>
	$- \left[\left(\frac{\partial\phi}{\partial z} + u_v \right) u_v + \left(\frac{\partial\phi}{\partial r} + v_v \right) v_v \right]$ <p>This is $-\bar{u}_i \cdot \bar{u}_v$ part in [23, eq. (3.56)].</p>
	$-\frac{1}{2} \left(\frac{a_0^2 \Omega_0}{r} \right)^2$ <p>This is $-\frac{1}{2} w_v^2$ part in [24, eq.(4.13)].</p>
	$+2\psi \frac{\partial q}{\partial s} + \frac{2}{\text{Re}} \left(\frac{\partial^2 \phi}{\partial s^2} + \frac{1}{r} \frac{\partial \phi}{\partial r} \right)$ <p>These are weak viscous treatment terms from [25, eq.(7.7)].</p>
	$-P_g - \frac{k}{We} + \frac{Bo}{We} z$ <p>These are standard surface-wave problem terms [24, eq.(4.11)].</p>

Table 5. Term by term analysis of Bernoulli's equation.

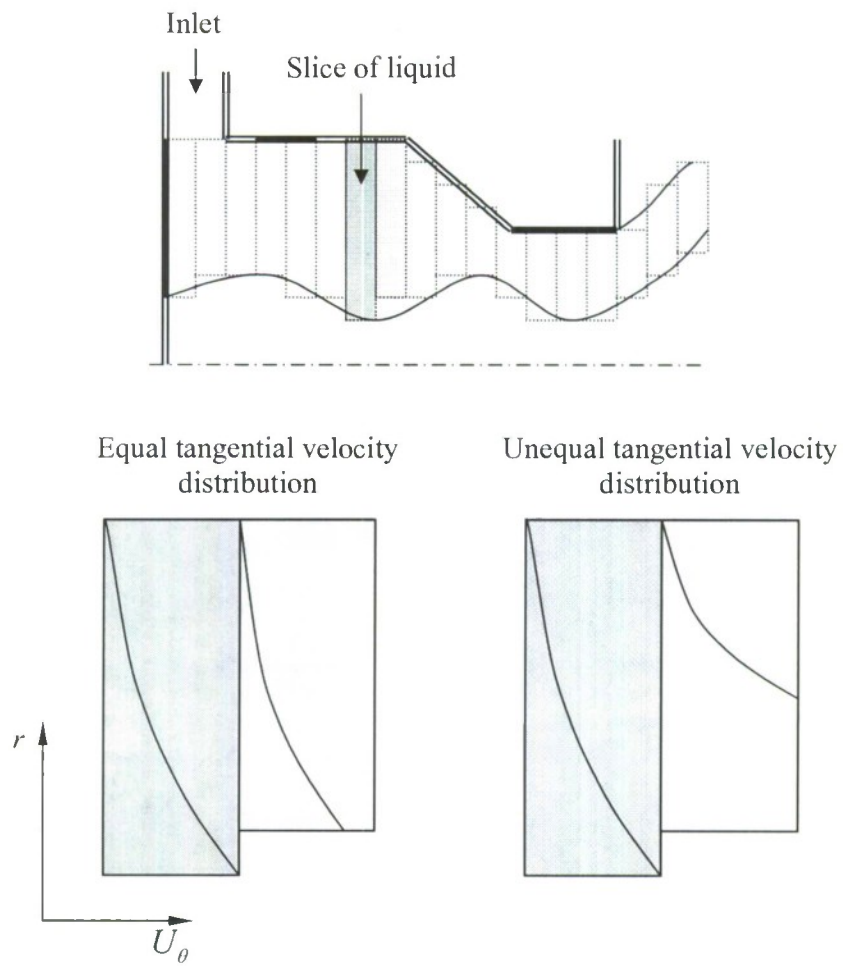


Figure 22. Disk representation of liquid column.

4. References

1. Bayvel, L., and Orzechowski, Z., *Liquid Atomization*, Taylor & Francis, Bristol, PA, 1993.
2. Bazarov, V.G., and Yang, V., "Liquid-Propellant Rocket Engine Injector Dynamics," *Journal of Propulsion and Power*, Vol. 14, No. 5, Sept.-Oct. 1998, pp. 797-806.
3. Yule, A.J., and Chinn, J.J., "Swirl Atomizer Flow: Classical Inviscid Theory Revisited," *ICLASS-94*, Rouen, France, July 1994.
4. Xue, J., Jog, M.A., Jeng, S.M., Steinhörsson, E., and Benjamin, M.A., "Influence of Geometry on the Performance of Simplex Nozzles under Constant Pressure Drop," *ILASS*, Madison, WI, 2002.
5. Park, H., and Heister, S.D., "Nonlinear Simulation of Free Surfaces and Atomization in Pressure Swirl Atomizers," *Physics of Fluids*, Vol. 18, No. 5, 2006, pp. 052103-052103-11.
6. Dash, S.K., Halder, M.R., Peric, M., and Som, S.K., "Formation of Air Core in Nozzles with Tangential Entry," *Journal of Fluids Engineering*, Vol. 123, 2001, pp. 829-835.
7. Bussman, M., Mostaghimi, J., and Chandra, S., "On a Three-Dimensional Volume Tracking Model of Droplet Impact," *Physics of Fluids*, Vol. 11, 1999, pp. 1406-1417.
8. Pasandideh-Fard, M., Bussman, M., Mostaghimi, J., and Chandra, S., "Simulating Droplet Impact on a Substrate Shape," *Atomization and Sprays*, Vol. 11, 2001, pp. 397-414.
9. Han, Z., Parrish, S., Farrell, P.V., and Reitz, R.D., "Modeling Atomization Processes of Pressure-Swirl Hollow-Cone Fuel Sprays," *Atomization and Sprays*, Vol. 7, 1997, pp. 663-684.
10. Bazarov, V.G., *Fluid Injector Dynamics*, Mashinostroenie Publication, Inc., Moscow, Russia, 1979.
11. Yoon, S.S., and Heister, S.D., "A Fully Nonlinear Primary Atomization," *15th Annual Conference on Liquid Atomization and Spray Systems (ILASS)*, held in Madison, Wisconsin, 2002, pp. 36-40.
12. Zhakarov, S.I., Richardson, R., and Heister, S.D., "Hydrodynamic Modeling of Swirl Injectors with Multiple Rows of Tangential Channels," *Joint Propulsion Conference*, Sacramento, CA, July 2006.
13. Park, H., and Heister, S.D., "A Numerical Study of Primary Instability on Viscous High-Speed Jets," *Computers and Fluids*, Vol. 35, No. 10, pp. 1033-1045.
14. Park, H., Yoon, S.S., and Heister, S.D., "A Nonlinear Atomization Model for Computation of Drop-Size Distributions and Spray Simulations," *International Journal for Numerical Methods in Fluids*, Vol. 48, No. 11, 2005, pp. 1219-1240.
15. Ponstein, J., "Instability of Rotating Cylindrical Jets," *Applied Scientific Research*, Vol. 8, No. 6, 1959, pp. 425-456.
16. Spangler, C.A., Hilbing, J.H., and Heister, S.D., "Nonlinear Modeling of Jet Atomization in the Wind-Induced Regime," *Physics of Fluids*, Vol. 7, No. 5, 1995, pp. 964-971.
17. Kim, D., Yoon, Y., and Han, P., "Effect of Flow Condition and Geometry on Flow Characteristics of a Swirl Injector," *16th Annual Conference on Liquid Atomization and Spray Systems*, Monterey, CA, May 2003.

18. Rump, K., and Heister, S.D., "Modeling the Effect of Unsteady Chamber Conditions on Atomization Processes," *Journal of Propulsion and Power*, Vol. 14, No. 4, 1998, pp. 576-579.
19. Yule, A. J., and Chinn, J. J., "Swirl Atomizer Flow: Classical Inviscid Theory Revisited", *ICLASS-94*, Rouen, France, July 1994
20. Taylor, G. I., "The Mechanics of Swirl Atomizers", *7th Int. Congress of Applied Mechanics*, Vol. 2., Sept 1948
21. Giffen, E., and Muraszew, A., "Atomization of Liquid Fuels", Chapman and Hall London, 1953
22. Lefebvre, A. H., "Atomization and Spray", Hemisphere, Washington 1989
23. Bayvel, L., and Orzechowski, A., "Liquid Atomization", Taylor and Francis, 1993
24. Khavkin, Y. I., "Theory and Practice of Swirl Atomizers", Taylor and Francis, 1989
25. Dumas, M., and Laster, R., "Liquid-Film Properties for Centrifugal Spray Nozzles", *Chemical Engineering Progress*, Vol. 49, No. 10, October, 1953.
26. Park, H., and Heister, S. D., "Nonlinear Simulation of Free Surfaces and Atomization in Pressure Swirl Atomizers", to appear, *Physics of Fluids*, 2006.
27. Reba, I., Brosilow, C., "Combustion Instability: Liquid Stream and Droplet Behavior. Part III: The Response of Liquid Jets to Large Amplitude Sonic Oscillations," WADC Technical Report 59-720, Wright Air Development Center, United States Air Force, 1960.
28. Harrje, D., Reardon, F. "Liquid Propellant Rocket Combustion Instability," NASA SP-194, 1972.
29. "Liquid Rocket Engine Injectors," NASA SP-8089, 1976.
30. Bazarov, V., Yang, V., "Liquid-Propellant Rocket Engine Injector Dynamics," *Journal of Propulsion and Power*, Vol. 14, No. 5, September-October 1998.
31. V. G. Bazarov and L.A. Lyul'ka, "Nonlinear Interactions in Liquid Propellant Rocket Engine Injectors", AIAA 98-4039, 1998.
32. Bazarov, V. G., "Liquid-Propellant Rocket Engine Injector Dynamics", *Journal of Propulsion And Power* Vol. 14, No. 5, Sept-Oct 1998
33. Bazarov, V. G., "Fluid Injectors Dynamics", Mashinostroenic Publication, Inc., Moscow, Russia, 1979
34. Vasin, A., et. al., United States Patent, US 6,244,041 B1, 12 June, 2001.
35. Yoon, S. S., and Heister, S. D., "A Fully Nonlinear Model for Atomization of High-Speed Jets," *Engineering Analysis with Boundary Elements*, V28, pp 345-357, 2004.
36. Park, H. B., "Flow characteristics of viscous high-speed jets in axial/swirl injectors", PhD Thesis Dept. of Aeronautics and Astronautics, Purdue University, 2005
37. Rump, K. M., and Heister, S. D., "Modeling the Effect of Unsteady Chamber Conditions on Atomization Processes," *Journal of Propulsion and Power*, V. 14, pp. 576-578, 1998.
38. Heister, S. D., Rutz, M., and Hilbing, J., "Effect of Acoustic Perturbations on Liquid Jet Atomization," *Journal of Propulsion and Power*, V. 13, No. 1, pp. 82-88, 1997.
39. Bazarov, V. G., "Fluid Injectors Dynamics", Mashinostroenic Publication, Inc., Moscow, Russia, 1979
40. Richardson, R., "Linear and Non Linear Dynamics of Swirl Injectors" PhD Thesis, Department of Aeronautics and Astronautics, Purdue University, August 2006
41. Miller J, K., "Experimental Study of Longitudinal Instabilities in a Single Element Rocket Combustor", MS Thesis, Department of Aeronautics and Astronautics, Purdue University, May 2005

42. L.S.Blackford, J. Choi, A. Cleary, E. D'Azevedo, J. Demmel, I.Dhillon, J. Dongarra, S.Hammarling, G. Henry, A. Petitet, K. Stanley, D. Walker, and R. C. Whaley. "ScaLAPACK Users' Guide". *Society for Industrial and Applied Mathematics*, 1997.
43. N. K. Rizk and A. H. Lefebvre, "Internal Flow Characteristics of Simplex Swirl Atomizer", *Journal of Propulsion and Power*, 6:528-533, 1986.
44. J. Cousin, S. J. Yoon and C. Dumouchel, "Coupling of Classical Linear Theory and Maximum Entropy Formalism for Prediction of Drop Size Distribution in Sprays: Application to Pressure-Swirl Atomizers", *Atomization and Sprays*, Vol. 6, pp. 601-622, 1996.
45. Yoon, S., "A Fully Nonlinear Model for Atomization of High Speed Jets", PhD thesis, Purdue University, 2002.

Appendices

Appendix A – Paper on Nonlinear Response of Swirl Injectors

Nonlinear Dynamic Response Modeling of a Swirl Injector

Renith Richardson¹, Hongbok Park², James V. Canino³, and Stephen D. Heister⁴
School of Aeronautics and Astronautics, Purdue University, West Lafayette, IN, 47907, USA

A fully nonlinear axisymmetric model has been utilized to characterize the dynamic response of a classical swirl injector and compared with the linear results of Bazarov and Yang. A Boundary Element Method (BEM) model has been developed to study the unsteady behavior under periodic inflow conditions or pulsating chamber pressure. The difference between pulsating the inlet velocity or the chamber pressure was insignificant, as the height of the wave on the liquid surface in vortex chamber is negligible when compared to the thickness of the liquid film. The amplitude response of the nonlinear model shows a significant deviation from the linear model after a certain frequency. A thorough analysis indicates that this phenomenon is dependent on the axial momentum of the liquid. Nonlinear effects appear to be minimal as the strong pressure gradients in the liquid film imposed by the swirling flow lead to relatively small surface waves even under large excitation conditions. The unsteady film formed by the atomizer is also tracked beyond the exit plane to evaluate the periodic formation of annular ligaments which are in turn assumed to form droplets using the linear analysis due to Ponstein.

Nomenclature

A	= Amplitude
a	= radius of nozzle
a_o	= radius to center of tangential chn.
B_o	= Bond number
D	= droplet diameter
ds	= grid space
FN	= Flow Number
f	= Frequency
G	= Green's function
g	= acceleration due to gravity
k	= wave number
L_n	= length of nozzle
L_v	= length of vortex chamber
N_D	= number of droplets
R_{in}	= radius to inlet channel
R_C	= radius of liquid surface
R_v	= radius of vortex chamber
r	= radial direction
s	= distance along the surface
SMD	= Sauter Mean Diameter
U	= jet speed

¹ Graduate Student, School of Aeronautics and Astronautics, Purdue University, AIAA Member.

² Graduate Student, School of Aeronautics and Astronautics, Purdue University, AIAA Member.

³ Graduate Student, School of Aeronautics and Astronautics, Purdue University, AIAA Member.

⁴ Professor, School of Aeronautics and Astronautics, Purdue University, 315 N. Grant Street, W. Lafayette, IN 47907, AIAA Associate Fellow

u	=	axial velocity
v	=	radial velocity
We	=	Weber number
z	=	axial direction
ΔP	=	pressure drop
Γ	=	vortex strength
β	=	surface slope
θ	=	direction of velocity
θ_D	=	cone half angle
ρ	=	density
σ	=	liquid surface tension
ϕ	=	velocity potential
κ	=	surface curvature
ω	=	growth rate

Subscripts

$(\)_D$	=	droplet property
$(\)_g$	=	gas property
$(\)_l$	=	liquid property
$(\)_t$	=	total or general solution
$(\)_r$	=	vortex-ring property

I. Introduction

A swirl injector or simplex/pressure-swirl atomizer is one of the more common devices used to atomize liquids. The hollow-cone simplex atomizer creates angular momentum by injecting the liquid tangentially into a vortex chamber. Since swirl injectors offer throttling advantages and give high thrust per element, they have been utilized in aerospace propulsion applications over the past sixty years. In particular, injectors of this type have seen substantial applications in rocket engines, particularly in engines developed in Russia. In propulsion applications, both static and dynamic characteristics of the injector have been of great interest to predict bulk performance and to understand instability mechanism related to the dynamic response of engines and their potential contributions or participation in combustion instabilities.

The steady-state performance of swirl atomizers has been addressed by a number of authors. Bayvel and Orzechowski¹ utilize the principle of maximum flow to solve for liquid film conditions within the injector. The approach has been used largely by Russian scientists and engineers studying simplex atomizers.² As a second theory, Yule-Chinn³ used axial momentum conservation principle to derive the equations of flow for a swirl injector without the critical assumption of the principle of maximum flow. While the utilization of the principle of maximum flow and axial momentum conservation are major differences between these two linear theories, predictions using the two approaches generally are in agreement.

More recently, nonlinear simulations have been conducted to assess the mean performance of the atomizers under a variety of flow and design conditions. Xue et al.⁴ and Park and Heister⁵ investigated the effect of geometric parameters on a simplex fuel atomizer; using the Arbitrary Lagrangian-Eulerian, and boundary element methods (BEM), respectively. Dash et al.⁶ studied formation of the air core in nozzles, Bussman et al.^{7,8} for pressure-swirl atomization in the near field and Han et al.⁹ for hollow-cone fuel sprays under steady inflow conditions.

There have been very few works in the literature that have focused on the dynamic aspects of these injectors. Pioneering efforts in this area are attributed to V. G. Bazarov, who developed the initial linear treatment in the 1970s¹⁰ and later published the work in a paper co-authored with V. Yang² in 1998. This latter contribution has provided a first glimpse of the complex dynamics of the simplex element for many readers in the Western world.

Since the element has a gas core, it responds to the instantaneous chamber pressure as this leads to changes in the pressure drop through the tangential channels. Waves are formed on the free surface in the vortex chamber due to oscillating mass flow at the inlet and these waves are at least partly reflected from the convergent section leading to the nozzle and the remaining is transmitted into the nozzle. Vorticity waves; comprised of regions of faster and slower swirling liquid, are also developed under unsteady chamber pressure conditions. The linear model accounts for these mechanisms in an inherently inviscid one-dimensional treatment resulting in a transfer function that relates pressure pulsations in the chamber or feed system to massflow pulsations delivered by the element.

In the present work, we apply an inviscid, axisymmetric BEM treatment to provide a nonlinear, multidimensional-flow capability for simulating swirl injector dynamics. The dynamic response of a single inlet

classical swirl injector is computed for a range of perturbation frequencies of the chamber pressure. Results are compared against the existing linear theory and the presence of nonlinear behavior, multidimensional effects and other phenomena are analyzed over a variety of operating conditions. As the BEM methodology permits computations beyond atomization events, studies are conducted to assess ligament and droplet sizes for unsteady inflow conditions. The model is described in the next section, followed by discussion of results and conclusions made from the study.

II. Model Description

Figure 1 provides a schematic of a simplex atomizer noting the fluid injection via tangential channels at the head end of the vortex chamber. The gas core develops naturally as a function of the vortex chamber diameter, inlet massflow and the degree of swirl imparted to the fluid via the pressure drop imposed from the injection manifold. The contraction to the nozzle facilitates acceleration and thinning of the film to provide a conical sheet that breaks up into a spray. Key dimensions and nomenclature are noted in Fig. 1 for application to the analysis and subsequent discussion.

Reference 11 provides a complete description of the basic model elements; only highlights will be presented here in the interest of brevity. An inviscid, incompressible, axisymmetric flow is presumed such that the flow dynamics are governed by Laplace's equation, $\nabla^2\phi = 0$. The boundary element method utilizes an integral representation of this equation to provide a connection between ϕ values on the boundary, the local geometry, and the local velocity normal to the boundary, $q = \partial\phi/\partial n$, as follows:

$$\alpha\phi(\vec{r}_i) + \int_S \left[\phi \frac{\partial G}{\partial \vec{n}} - qG \right] ds = 0 \quad (1)$$

where $\phi(\vec{r}_i)$ is the value of the potential at a point \vec{r}_i , S is the boundary of the domain, α is the singular contribution when the integral path passes over the "base point", and G is the free space Green's function corresponding to Laplace's equation. For an axisymmetric domain, the free space Green's function can be expressed in terms of elliptic integrals of the first and second kinds and is a function solely of the instantaneous surface geometry. For this reason, a discrete representation of Eq. (1) can be cast as a linear system of equations relating local ϕ and q values. In the discretization, both ϕ and q are assumed to vary linearly along each element, thereby providing formal second-order accuracy for the method. Since the resulting integrals do not have exact solutions in this case, Gaussian quadrature is used to maintain high accuracy of integration and preserve second-order accuracy overall.

While this governing equation is linear, nonlinearities in these free surface problems enter through the boundary condition at the interface. The unsteady Bernoulli equation provides a connection between the local velocity potential and the surface shape at any instant in time. Prior formulations¹¹ have provided a derivation of this result suitable for implementation in a Lagrangian surface tracking environment. For the swirling flow, modifications are required to account for the centrifugal pressure gradient created by the swirl. Without swirl, the dimensionless unsteady Bernoulli equation is as follows:

$$\frac{D\phi}{Dt} = \frac{1}{2}|\vec{u}_t|^2 - \vec{u}_t \cdot \vec{u}_v - P_g - \frac{\kappa}{We} + \frac{Bo}{We}z \quad (2)$$

where ϕ is the velocity potential and κ is the local surface curvature and the Weber number ($We = \rho U^2 a / \sigma$), Bond number ($Bo = \rho g a^2 / \sigma$) become the dimensionless parameters governing the problem. Physically, this result is a Lagrangian form suitable for use for fluid elements moving with the local velocity of the free surface. The terms on the RHS of the equation include the effect of dynamic pressure, local gas-phase pressure, and capillary and hydrostatic pressure contributions respectively. In Eq. (2), the total surface velocity, \vec{u}_t , can be computed via a superposition of the base axial flow in the injector (ϕ, \vec{u}) with a potential vortex (ϕ_v, \vec{u}_v). Letting u , v , and w represent axial, radial, and circumferential velocity components respectively, we may write:

$$\phi_t = \phi + \phi_v \quad u_t = u + u_v \quad v_t = v + v_v \quad w_t = w + w_v \quad (3)$$

Superposition of a potential vortex can be achieved by starting with the complex potential:

$$F\left(z = -\frac{i\Gamma}{2\pi} \log(z)\right) \quad (4)$$

where z is complex variable, Γ is vortex strength, and F is the complex potential.

The resulting velocity components for this flow are as follows:

$$u_v = 0, \quad v_v = 0, \quad w_v = \frac{\Gamma}{2\pi r} \quad (5)$$

This vortex is irrotational as known since $\vec{\omega} = \nabla \times \vec{u} = 0$, except at $\vec{r} = 0$. Using Eq. (5), the total velocity in Eq. (3) can be computed;

$$\begin{aligned} \frac{1}{2} |\vec{u}_t|^2 - \vec{u}_t \cdot \vec{u}_v &= \frac{1}{2} [(u + u_v)^2 + (v + v_v)^2 + (w + w_v)^2] &= \frac{1}{2} [u^2 + v^2 + w_v^2] - w_v \cdot w_v \\ &= \frac{1}{2} [u^2 + v^2 + w_v^2] - \frac{1}{2} w_v^2 \end{aligned} \quad (6)$$

where

$$\frac{1}{2} w_v^2 = \frac{1}{2} \left(\frac{\Gamma}{2\pi r} \right)^2 = \frac{1}{2} \left(\frac{2\pi a_0 U}{2\pi r} \right)^2 = \frac{1}{2} \left(\frac{a_0 U}{r} \right)^2 \quad (7)$$

Choosing the ideal tangential injection velocity (U), the orifice radius (a), and liquid density (ρ) as dimensions, the dimensionless result can be written as,

$$\frac{D\phi}{Dt} = \frac{1}{2} |\vec{u}|^2 - P_g - \frac{\kappa}{We} + \frac{Bo}{We} z - \frac{1}{2} \left(\frac{a_0}{a} \right)^2 \frac{1}{r^2} \quad (8)$$

where the Weber and Bond numbers are defined as above. Since we have nondimensionalized against the tangential injection velocity, U , the Rossby number does not appear explicitly in Eq. (8), but the last term on the RHS of the equation corresponds to the circumferential pressure developed by the potential vortex. In this context, the radial location of the center of the tangential channel, a_0 , defines the dimensionless strength of the vortical flow. The kinematic equation for motion of points on the free surface can be expressed:

$$\frac{Dz}{Dt} = \frac{\partial \phi}{\partial s} \cos \beta - q \sin \beta \quad \frac{Dr}{Dt} = \frac{\partial \phi}{\partial s} \sin \beta + q \cos \beta \quad (9)$$

where β is the local slope of the wave with respect to the horizontal direction. Equations (8) and (9) are integrated in time using a 4th-order Runge-Kutta scheme to provide the evolution of the velocity potential and the motion of the free surface.

The computational model was incorporated with oscillating chamber pressure rather than perturbing the inflow velocity to simulate a chamber pressure oscillation. This boundary condition will allow the mass flow in the inlet channels to adjust naturally to the instantaneous pressure within the vortex chamber. The pressure drop is assumed to be a sinusoidal function of time $\Delta P = \Delta P_{\text{Steady}} + \varepsilon \sin(\omega t)$, where steady state pressure drop is calculated from the initial conditions,¹² where the steady state pressure drop ΔP_{Steady} is calculated using initial conditions (Eq. 10).

$$\Delta P_{\text{Steady}} = \frac{q_{\text{mean}}^2 R_m^2}{2R_{C_{\text{Steady}}}^2} \quad (10)$$

The mass flow rates at the nozzle exit plane can be computed using is computed using the methodology described in Ref. 18 is used to calculate the velocity potential and its derivatives at the interior nodes. It involves the development of integral equation for Green's function followed by the integration and the calculation of the solution for unknown values of velocity potential and its derivatives. The derivative of the velocity potential is then used to calculate the nozzle exit mass flow rate.

For long integrations or resolution of highly distorted surfaces, points on the free surface will tend to bunch in regions of higher curvature as a result of the free-surface motion. For this reason, the points on the free surface are redistributed at each time step using a cubic spline fitting of the instantaneous shape. The Laplace equation is solved to update velocities and the process is marched forward in time. Formally, the resolution of the scheme is second-order in space and 4th-order in time, but surface curvature and capillary forces are resolved with 4th-order accuracy given a set of points defining the instantaneous shape.¹¹

As the surface forms a conical film when it exits the nozzle, instabilities result in the formation of annular ring-shaped ligaments. A pinching criteria is used wherein the ligament is physically separated from the parent surface if nodes on either side of the film lie within 2/3 grid space of each other. Prior studies^{13,14} using this criterion indicate an insensitivity to the resultant ligament size using this approach. The droplet diameter after pinch-off is calculated from the linear theory due to Ponstein.¹⁵ The growth rate, ω , was related to the wave number of the disturbance, k , as follows:

$$w^2 = \left[\frac{\sigma}{\rho a_r^3} (1 - k^2 a_r^2) + \left(\frac{\Gamma_r}{2\pi a_r^2} \right)^2 \right] (ka_r) \frac{I_1(ka_r)}{I_0(ka_r)} \quad (11)$$

where a_r and Γ_r are the radius and the circulation of the vortex-ring, respectively, and I_0 and I_1 are modified Bessel functions of 0th and 1st order. When $\Gamma_r = 0$, this result reduces to the classic Rayleigh result for instability of a liquid column. We have assumed that a_r is much smaller than the nozzle radius, a which requires $ka_r \leq 1.0$ for application of this analysis. The equivalent circular diameter of the ring-shaped ligaments is used to determine the appropriate a_r value for each ring. Using Ponstein's result, the k value that maximizes ω is determined for each ring pinched from the parent surface. Droplets are assumed to be formed instantaneously from this initial condition and the initial velocity and position of each droplet is determined assuming they are uniformly distributed about the circumference of the ring. The output from this computation is then used as the input of the droplet tracking program. Newton's 2nd law is applied to describe the motion of a droplet assuming aerodynamic drag to be the only external force acting on a droplet.

$$m_D \frac{d\vec{u}_D}{dt} = C_D \frac{1}{2} \rho_g (\vec{u}_g - \vec{u}_D) |\vec{u}_g - \vec{u}_D| A_D \quad (12)$$

where A_D is the projected area of a droplet ($\pi D^2/4$), m_D and \vec{u}_D are droplet mass and velocity, respectively. Recent calculations⁵ have shown good comparison with measured film thicknesses and some limited comparison with Sauter Mean Diameters from sprays formed from these atomizers.

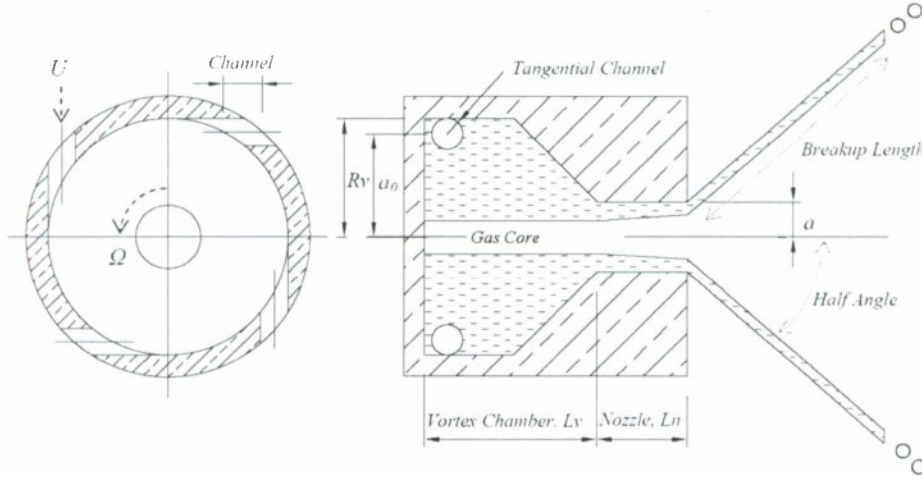


Figure 1. A classical swirl injector noting nomenclature used for design

5. Baseline Case Simulations

Figure 1 provides a to-scale representation of the baseline injector geometry that was analyzed. This monopropellant swirl injector design was derived using the procedure outlined in Ref. 1 to deliver 9.07E-2 kg/s of water at a pressure drop of 0.69 MPa. It has a nominal total spray angle of 90° and the film thickness computed to be approximately 0.43 mm at the nozzle exit. The injector geometry for this design is summarized in Table 1 below:

Table 1. Assumed Baseline Geometry for Swirl Atomizer Simulations

Radius to Center of Tangential Chn, a_o	= 3.226 mm
Radius of Nozzle, a	= 2.151 mm
Radius of Vortex Chamber, R_v	= 4.234 mm
Radius of Tangential Channel	= 0.643 mm
Length of Tangential Channel	= 1.516 mm
Length of Nozzle, L_n	= 1.500 mm
Length of Vortex Chamber, L_v	= 4.547 mm
No. of Inlet Channels	= 4
Inlet Velocity	= 17.50 m/s

Since the BEM computation assumes an axisymmetric domain, the inflow from the four tangential channels had to be approximated with a cylindrical passage having the same total inflow area. Using this approach, the inflow velocity is replicated. The length of the channel was set to replicate the overall flow time the fluid spends in the tangential channels. The liquid density of 1000 kg/m^3 , injection velocity of 17.50 m/s , and nozzle radius of 2.151 mm served as the basis for nondimensionalizing all other parameters.

Figure 2 shows a typical computational grid employed in the studies. The mass flow is specified on the inlet boundary or the pulsating chamber pressure condition is specified; nodes on solid walls are subject to the flow tangency condition ($q = 0$), and nodes of the free surface are subject to the Bernoulli condition derived in Eq. (8). The node lying at the free surface junction with the head-end of the vortex chamber is treated as a moving node such that the free surface remains perpendicular to the wall at this location. The grid spacing along the head-end of the vortex chamber is stretched/compressed to accommodate movement of the corner node. Using this treatment, the gas core radius evolves naturally as a simulation result from an arbitrary initial condition.

In Ref. 5, we compared nonlinear steady-state computations with the linear theory for a variety of parametric injector designs including the baseline geometry summarized in Table 1. Results were generated for various grids thereby demonstrating convergence and accuracy of the model. These grid tests showed no discernable difference in core radius, film thickness, velocities, and jet half angle, for the meshes studied from $ds = 0.020$ to 0.040 . Computed film thicknesses also show excellent agreement with experimental results and limited comparisons of computed drop sizes with measured data show good agreement. A typical number of nodes that evolve for subsequent calculations is 250 nodes with the grid space of $ds = 0.032$ but the number of points increases with time up to 900 nodes due to increased jet length. In addition, the simulation time for a dynamic response computation takes typically about 2 weeks on the 1.0 GHz Athlon CPU used in the modeling.

The steady-state results show surprisingly little nonlinear effects and the core radius, nozzle exit film thickness, and jet half angle were nearly identical for both the nonlinear calculation and the linear theory for a wide range of designs. The one exception to this result is for nozzles that are short; in this case the linear theory tends to over predict the spray half angle and under predict the film thickness relative to the model calculations. Table 2 shows the extent of agreement between the two BEM calculations (using perturbing inflow velocity and the other using pulsating chamber pressure incorporating Ref. 18 for solution at interior nodes) and the linear theory for the baseline conditions summarized previously. The minor differences between them are attributed to the limitations of the methods employed in calculating these parameters and to the accurate calculation of fluid properties at interior nodes rather than the difference in the specified boundary condition. This is further confirmed, as will be discussed in a later section, by the fact that the change in core radius in the vortex chamber due to fluctuating chamber pressure is negligible compared to the thickness of the liquid film.

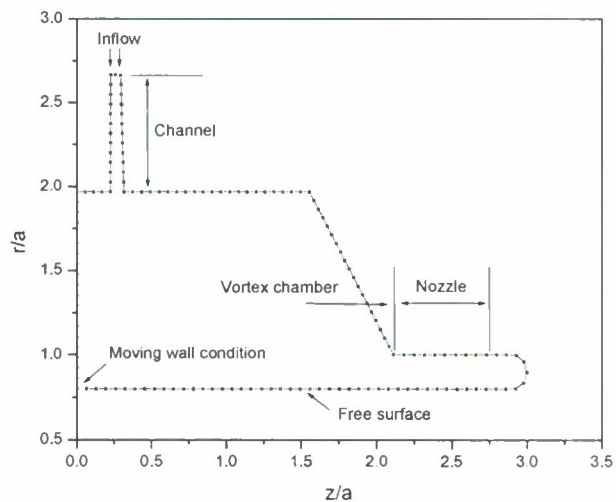


Figure 2. A 2-D axisymmetric grid system used to model a swirl injector.

Table 2. Calculated result comparison against the theoretical result of V.G. Bazarov¹⁰

		Theoretical result	BEM (perturbing inflow)	BEM (perturbing chamber pression)
Core radius (r_a)		0.707	0.705	0.706
Film thickness (h)		0.200	0.205	0.204
Half spray angle		45°	45.5°	45.5°
Total Velocity (m/s)	Nozzle entrance	-	20.7 (at wall) 11.7 (at free surface)	20.5 (at wall) 11.6 (at free surface)
	Nozzle exit	-	24.3 (at wall) 21.0 (at free surface)	24.3 (at wall) 21.03 (at free surface)
	Outside injector	36.09	36.12 ($z = 5.04$, $r = 2.78$)	36.10 ($z = 5.04$, $r = 2.78$)
Axial Velocity (m/s)	Inlet channel	17.50	17.50	17.56
	At nozzle center	17.37	17.45	17.51
	Outside injector	26.26	26.26	26.3

III. Results and Discussion

D. Static Characteristics Analysis

The geometry provided in Table 1 served as a baseline condition for the computations. In a steady chamber pressure condition, the radial/axial velocity profiles on both upper and lower fluid surfaces are compared against theoretical values in Fig. 3. Results tend to asymptotically approach the quasi-1-D theoretical values as one moves far away from corners. Figure 4 also shows the free surface shape inside the injector as well as the final jet shape (at $t^* = 12$) with shed droplets. The liquid core evolves naturally as a part of the calculation as does the cone angle formed by the conical sheet exiting the orifice. Under steady flow conditions, the shed droplets are moving in the same direction as the parent jet and their size distribution is almost constant. The computed flow properties for the steady injection case result in an SMD/a of 0.185, and a cone half angle of 46° with other statistical properties summarized in Table 3.

Figure 5 provides a 3-D visualization of the spray evolution and the jet core structure. The breakup length is nearly constant after $t^* = 5.0$ and shed droplets are tracked downstream with the direction angle of the parent jet. The overall spray is qualitatively similar with that of actual experimental images.¹⁶ The initial ligament pinching events lead to droplets that are dispersed somewhat from the final cone angle formed by the spray. This is an artifact of the initial conditions selected for the simulation and not necessarily representative of the chaotic startup observed during the chamber filling process of a real device.

Table 3. Statistical properties for a swirl injector

	Properties
SMD/a	0.185
N_D	1741
D_D/a	0.198
\bar{u}_D/U	1.21
\bar{v}_D/U	1.26
θ_D (°)	45.8

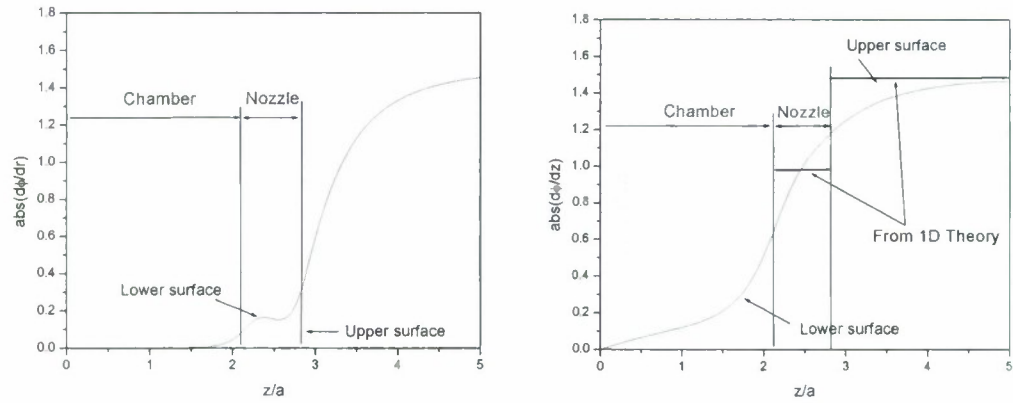


Figure 3. Radial (left) and axial (right) velocity profile along fluid surface in a classical swirl

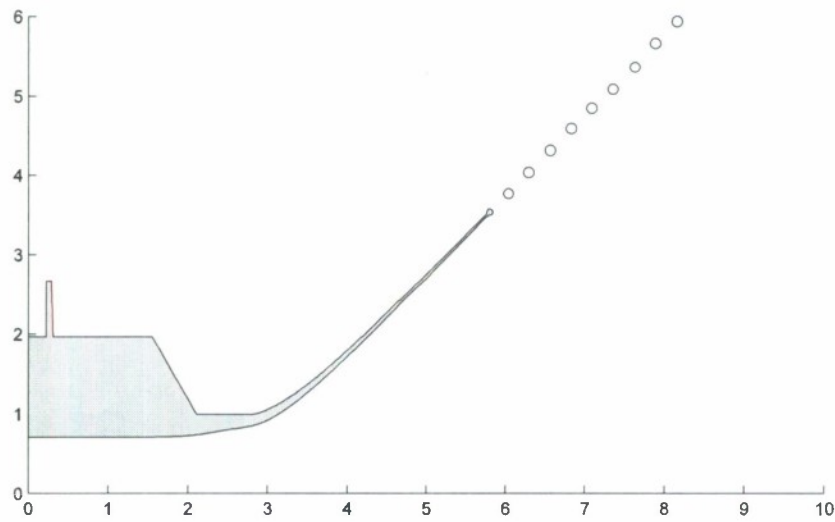


Figure 4. Final jet shape showing shed droplets for baseline swirl injector, at $t^* = 12.0$.

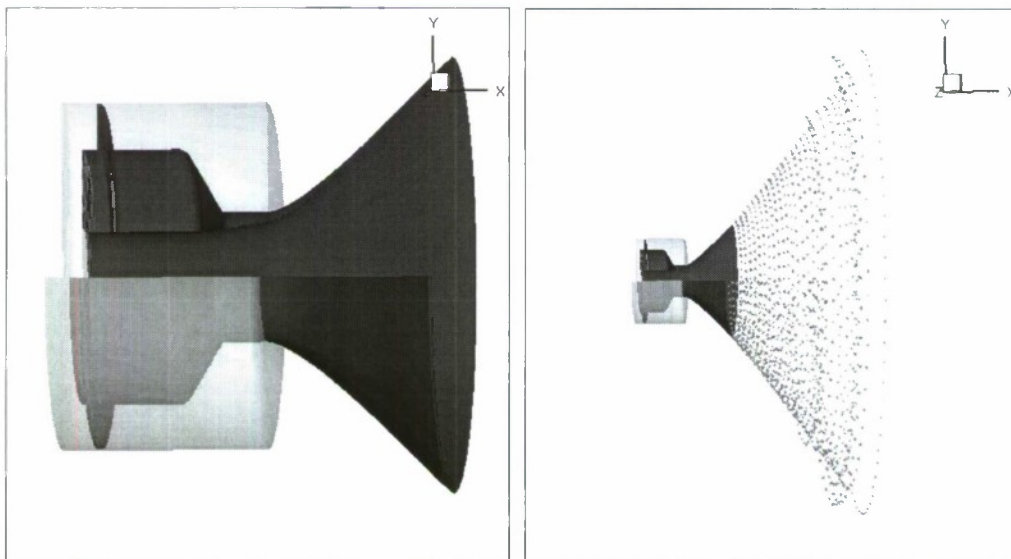


Figure 5. Dimensional view of the final jet shape computed for baseline conditions noted in

E. Behavior under Dynamic Injection

The dynamic response was studied for the injector geometry shown in Fig. 1 and Table 1 at the baseline injection velocity and pressure drop of 17.5 m/s and 0.69 MPa respectively. To compare results against the theoretical analysis of Bazarov & Yang,² the velocity was interrogated at a variety of locations in the film. Figure 6 shows locations for dynamic response analysis in our calculation. The detailed locations are as follows:

Pt 1:	U_{inp} :	$z = 0.258$,	$r = 2.665$	(at the channel inlet)
Pt 2:	U_{chamb} :	$z = 1.495$,	$r = 1.968$	(at the chamber wall)
Pt 3:	$U_{\text{noz,entr}}$:	$z = 2.113$,	$r = 1.000$	(at the wall of nozzle entrance)
Pt 4:	$U_{\text{noz,exit}}$:	$z = 2.798$,	$r = 1.000$	(at the wall of nozzle exit)
Pt 5:	U_{out} :	$z = 5.036$,	$r = 2.789$	(outside the nozzle)

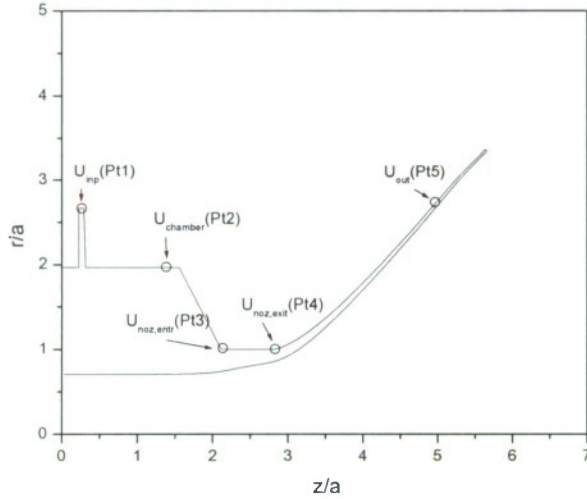


Figure 6. Selected locations for dynamic response analysis in a classical swirl injector.

(ϖ^*) for actual oscillation frequency (f) is as follows:

$$\varpi^* = \frac{a}{U} \varpi = \frac{a}{U} 2\pi f = \frac{2.151E-3}{17.5} \times 2\pi \times f = 7.7229E-4 \times f \quad (12)$$

Then, for a given input oscillation frequency, the injection velocity pulsation can be written:

$$F(\varpi^*) = A \sin(\varpi^* t^*) \quad (13)$$

where A is the amplitude of the massflow pulsation. In our study, the disturbance is prescribed as a fluctuation of the inflow velocity in the tangential channel, Eq. (13), or as perturbation of chamber pressure as seen in Eq. (14).

$$\Delta P = \Delta P_{\text{Steady}} + \varepsilon \sin(\omega t) \quad (14)$$

In addition, the inlet for the tangential channel is assumed as the circular cylinder in our axisymmetric simulation and its area is determined to have the same mass flow rate with the actual injector. In order to keep the constant area for the same mass flow rate throughout the tangential channel, the channel width at the tip and the root can be calculated:

$$W_{T,\text{tip}} = \frac{R_v}{R_v + L_T} W_{T,\text{root}}, \text{ where } W_{T,\text{root}} = \frac{4R_T^2}{2R_v} \quad (15)$$

Two distinct approaches have been used for simulation of unsteady flow conditions. Initially, we utilized a forced excitation via oscillation of the inlet massflow. Since the dynamics of the film thickness in the vortex chamber could lead to large amplitude surface waves, this process can in principle give results substantially different from the case where the gas pressure in the vortex chamber was oscillating in time. For this reason, a second approach was also investigated wherein the oscillation was imposed via an unsteady pressure in the vortex chamber. This latter approach is more realistic for dynamics induced by combustion chamber pressure variations, while the former approach is more representative for feed system based oscillations.

6. Dynamic Massflow Simulations

The dimensionless time in the computational domain is $t^* = U/a \cdot t$, so the dimensionless oscillation wave number

7. Dynamic Chamber Pressure Simulations

Here, the unsteady pressure drop across the film in the vortex chamber must be ascertained in order to determine the instantaneous pressure drop across the tangential channels. From the radial momentum equation, $\frac{V_\theta'^2}{R'} = \frac{1}{\rho'} \frac{\partial p'}{\partial R'}$, where for the potential vortex: $V_\theta' = \frac{\Gamma'}{2\pi R'}$. After integration, the dimensional pressure drop across the liquid film can be computed:

$$\Delta P_1' = -\frac{\rho' \Gamma'^2}{8\pi^2} \left(\frac{1}{R_{in}'^2} - \frac{1}{R_C'^2} \right)$$

So that the nondimensional pressure drop can be written:

$$\Delta P_1 = -\frac{\Gamma^2}{8\pi^2} \left(\frac{1}{R_{in}^2} - \frac{1}{R_C^2} \right)$$

Substituting nondimensional circulation $\Gamma = 2\pi R_{in} V_\theta = 2\pi R_{in} V_{in}$ we obtain:

$$\Delta P_1 = -\frac{R_{in}^2 V_{in}^2}{2} \left(\frac{1}{R_{in}^2} - \frac{1}{R_C^2} \right) = \frac{V_{in}^2}{2} \left(\frac{R_{in}^2}{R_C^2} - 1 \right) \quad (16)$$

Assuming a constant stagnation pressure in the manifold and neglecting viscosity losses, Bernoulli's equation gives the pressure drop across the inlet channel: $\Delta P_2 = \frac{V_{in}^2}{2}$.

So the total pressure drop across the injector is the sum of pressure drops across the liquid film and inlet channel:

$$\Delta P = \Delta P_1 = \Delta P_2 = \frac{V_{in}^2}{2} \frac{R_{in}^2}{R_C^2} \quad (17)$$

Knowing this pressure drop the inflow velocity can be computed as:

$$V_{in} = \sqrt{2\Delta P} \frac{R_C}{R_{in}} \quad (18)$$

Where the overall pressure drop in the system is assumed to be a sinusoidal function of time $\Delta P = \Delta P_{Steady} + \varepsilon \sin(\omega t)$. The steady state pressure drop is calculated from the initial conditions:

$$\Delta P_{Steady} = \frac{q_{mean}^2 R_{in}^2}{2R_C^2} \quad (19)$$

Figure 3 shows a typical computational grid employed in the studies. The initial pressure drop is computed from Eq. (12) based on the steady state solution for the core radius using constant inflow rate. This pressure drop plus perturbation is further converted to massflow on the inlet boundary using Eq. (13).

F. Simulations Assuming Forced Mass Flow Pulsations

A series of simulations were conducted using the unsteady massflow methodology outlined in Eqs. 12–15. An initial simulation was performed with a 10% massflow fluctuation ($A = 0.1$) at a frequency of 5000 Hz. At lower frequencies, the dynamic simulation can require long integration times in order to build up statistical properties for drop sizing. In order to save computational cost, this simulation was restarted from the steady state solution obtained at the time of $t^* = 5.0$ and integrated in time until quasi-periodic behavior was obtained. The input and nozzle exit velocity histories are overlaid for the period $10 < t^* < 20$ in Fig. 7. The phase lag and amplitude modulation of the input signal is evident from this comparison.

The dynamic response for a single cycle of the imposed oscillation is depicted at various points in the injector in Fig. 8. The unsteady part of the signal is plotted at each location in order to assess wave amplitude and phase shifts at various points in the flow path. In Fig. 8, the oscillation frequency and the amplitude, for the

plot on the left, were set as $f = 5000$ Hz and $A = 0.1$, respectively. The vortex chamber acts as an accumulator and changes in massflow cause very little variations in velocity at Pt. 2; the massflow variations lead to changes in the size of the vortex core in this region. At Pt. 3 (nozzle inlet), a very large lag is notable and the amplitude of the oscillation increases as the fluid accelerates into the contraction region. At the nozzle exit, the oscillation amplitude is diminished somewhat as the swirl velocity is increased. The signal actually appears to be leading the input at this location for the conditions studied—this unusual characteristic is unique to swirl injectors with large vortex chambers that can cause large lags in response. The amplitude of the signal is attenuated further at the nozzle exit and into the conical film with smaller phase lags noted in these regions due to the relatively shorter flow times characteristic of the nozzle and regions downstream.

The right plot of Fig. 8 shows the dynamic response for $f = 1000$ Hz and $A = 0.1$. At this lower frequency, the response lags the input much more modestly, and the overall trends in amplitude are preserved from the 5000 Hz case. As the flow times are more comparable to the oscillation period in this case, the overall lag of the injector is much more modest.

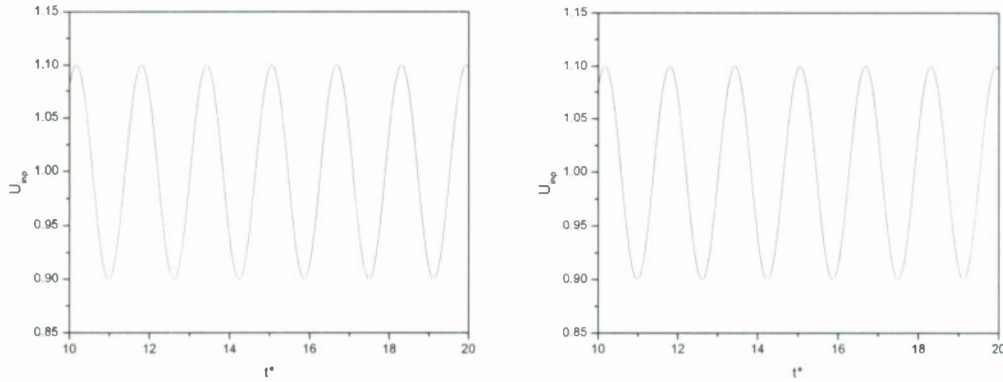


Figure 7. Raw input (left) and response (right) for initially disturbed inflow velocity; the oscillation frequency and the amplitude were set as $f = 5000$ Hz and $A = 0.1$, respectively.

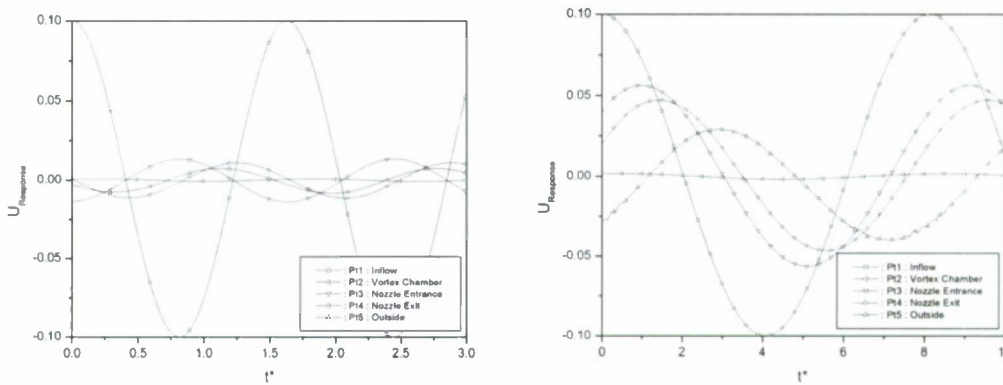


Figure 8. Dynamic response through a classical swirl injector, which was investigated in velocity response; the oscillation frequency and the amplitude where set as $f = 5000$ Hz, $A = 0.1$ (left), and $f = 1000$ Hz, $A = 0.1$ (right), respectively.

G. Parametric Studies Assuming Chamber Pressure Pulsations

The dynamic responses of a single channel swirl injector, whose parameters are given in Table 1 (baseline injector), was analyzed using the linear model developed by Bazarov and compared with the computational results at various frequencies. These responses are computed at the exit plane of nozzle of the swirl injector. A nondimensional time step of $dt = 0.0005$ along with a grid spacing of $ds = 0.032$ was used for each of these cases. An 8.4% perturbation of pressure, corresponding to a massflow pulsation of 3.5% across the injector was used in all our computations unless specified otherwise.

For the baseline injector operating at 0.69 MPa the amplitude response is shown in Fig. 9 and the corresponding phase shift associated with it shown in Fig. 10. The amplitude response predicted by the computational model is in close agreement with the linear results for frequencies less than 5 kHz. For frequencies larger than 5 kHz the BEM model predicts a sharp drop in the amplitude of the computed oscillation from that which is predicted by the linear theory, indicating that the injector is approximately stable at high forcing frequencies. The computed phase shift (Fig. 10) shows a similar behavior, noting a reasonable agreement with linear theory until the 5 kHz region, at which point we see a strong departure. A number of studies have been conducted to establish the cause of this departure from the linear theory as outlined below.

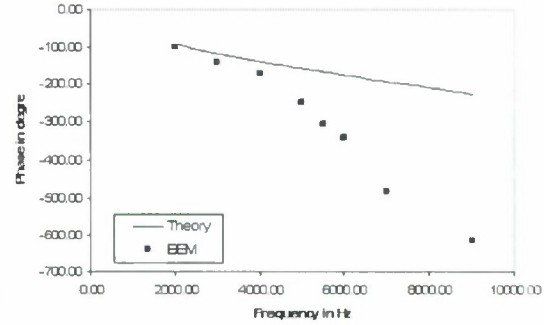
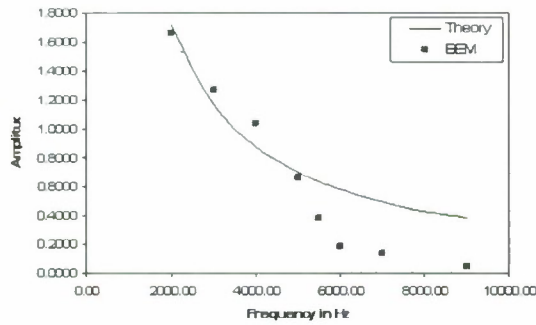


Figure 9. Amplitude response vs frequency; Figure 10. Phase shift in degrees vs. frequency, comparing linear theory with computational results.

The baseline injector operating at 1.38 MPa was considered in order to quantify the effect of steady state operating pressure on the BEM computed dynamics response deviation from the linear theory. The Weber number $We = 17,978$ and Reynolds number $Re = 53,171$ are changed accordingly. As pressure is doubled the injection velocity changes by a factor of $\sqrt{2}$, therefore $V_m = 24.75$ m/s .

1. Effect of mean injection velocity

The amplitude response (Fig. 11) of the 1.38 MPa baseline injector shows similar behavior as that of the original 0.69 MPa injector. The computational results start to deviate from the linear theory around 7 kHz; which is what one would expect in scaling velocities using the Bernoulli equation ($5 \text{ kHz} * \sqrt{2}$; 7 kHz). By plotting the amplitude of the response verses Strouhal number ($Sh_T = \frac{\omega L_c}{V_m}$) in Fig. 13, the two results lie on top of one another, indicating that the departure from linear theory is strongly dependent on the liquid injection velocity. The computed phase shift associated with these shows (Fig. 12) a similar trend as that of the 0.69 MPa injector except that the change in slope occurs at a frequency of 7 kHz.

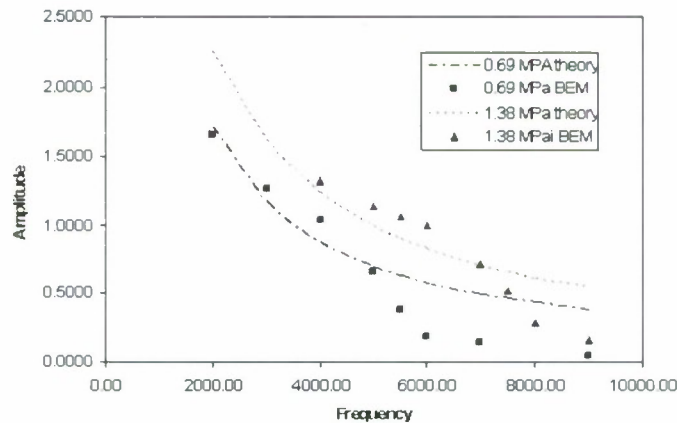


Figure 11. Amplitude response vs. frequency; comparing baseline swirl injector operating at 0.69 and 1.38 MPa.

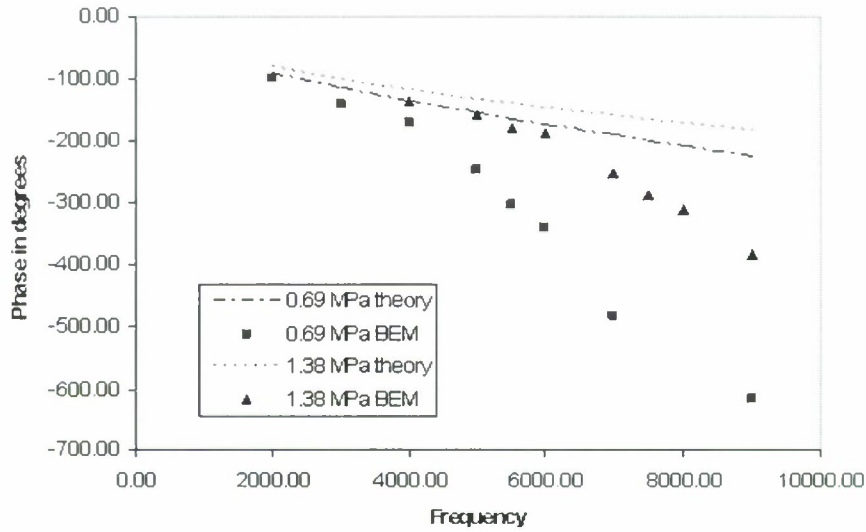


Figure 12. Phase shift in degrees vs. frequency; comparing baseline swirl injector operating at 0.69 and 1.38 MPa.

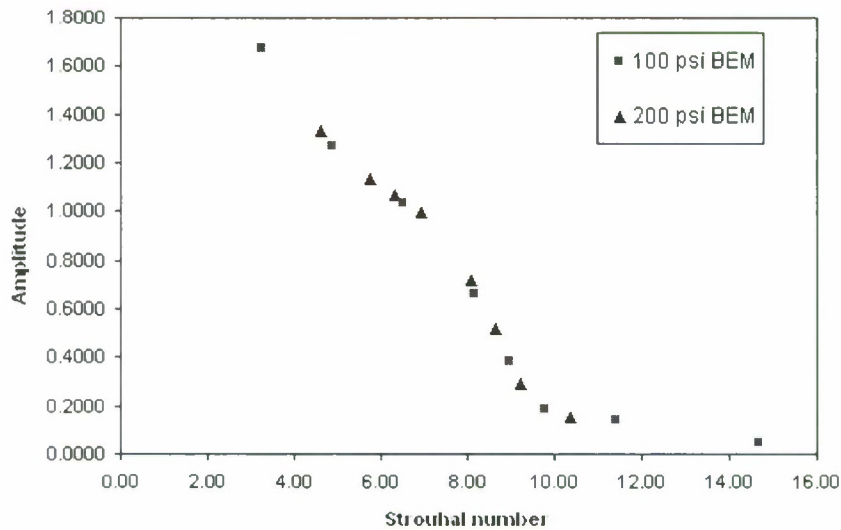


Figure 13. Amplitude vs. Strouhal number; comparing swirl injector operating at 0.69 and 1.38 MPa.

8. Nonlinearity of baseline injector

To determine whether the deviation in the amplitude response is dependent on nonlinear effects, the baseline injector at 0.68 MPa was perturbed at 3 different frequencies to as much as 90% of the mean pressure drop. Figure 14 shows the scaling of the massflow perturbation as a function of the amplitude of the pressure perturbation indicating a very linear dependence over the wide range of imposed unsteady pressure signals. Even at 7 kHz which lies on the non-agreeing side of the frequency range the swirl injector exhibits linear behavior. For this reason, nonlinear effects do not appear to be the cause of the difference between the linear theory and the BEM computations.

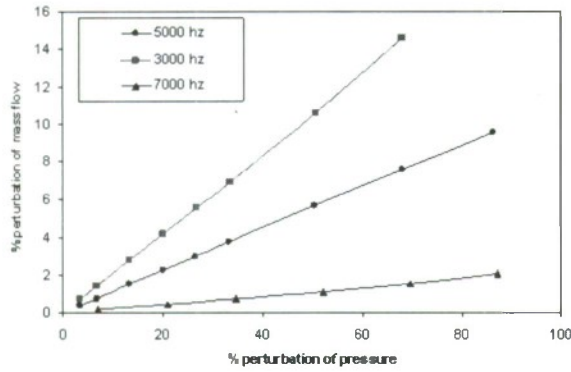


Figure 14. Graph illustrating the lack of non linear effects.

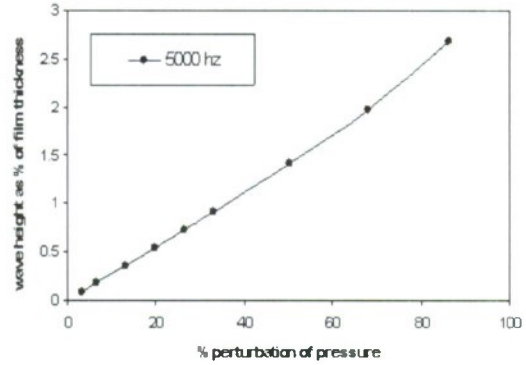


Figure 15. Change in wave height on the free surface for varying perturbing pressures.

The lack of nonlinear effects can be partly explained by the lack of any significant change in the wave height in the vortex chamber when compared to the liquid film thickness (Fig. 15). A perturbation of up to 90% of the mean pressure drop results in the liquid thickness changing by less than 3%. For this reason, there is little difference between an imposed massflow pulsation vs. an imposed chamber pressure perturbation as the vortex chamber responds very similarly in either case.

9. Effect of the inlet channel location and width

One of the main differences of the BEM model as compared to an actual swirl injector is the way the inlet channels are modeled. The tangential inlets of the actual swirl injector are modeled as 2-D axisymmetric radial inlet such that the mass flows are matched. A series of simulations were conducted to determine the effect this difference in modeling would have on the overall response of the swirl injector. The location of the inlet channel was moved very close to the head end of the vortex chamber (from 10.6% to 1.5% of the vortex chamber length), keeping all other parameters fixed at baseline injector values. The amplitude and phase response are shown in Fig. 16 & Fig. 17 respectively. The minor discrepancies in the magnitude of the amplitude response can be attributed to the different inlet location resulting in a different pattern of reflecting surface waves in the vortex chamber. However, the amplitude and phase rolloff (relative to the linear theory) at 5 kHz is still readily apparent.

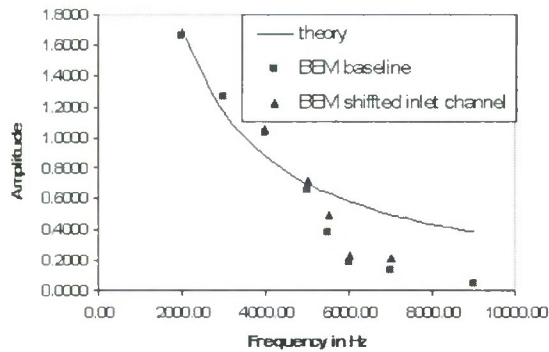


Figure 16. Effect of amplitude response by moving the tangential location closer to head end of vortex chamber.

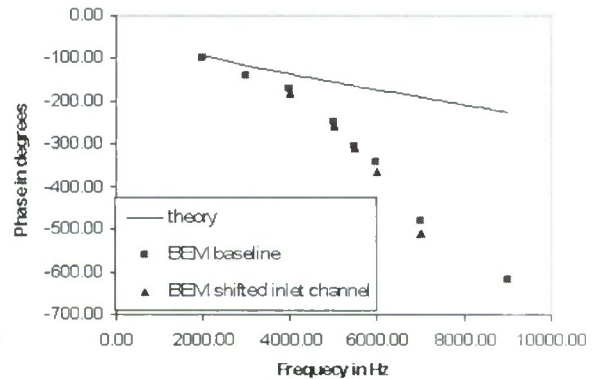


Figure 17. Effect of phase shift response by moving the tangential location closer to head end of vortex chamber.

The width of the inlet channel (W_7) was increased by an order of magnitude keeping massflow constant in order to assess the effect of this variable. Figures 18 and 19 depict the amplitude and phase response for this case as compared the baseline injector. Increasing the width reduces the inlet velocity by a corresponding factor, therefore any dependence on the artificially imposed radial velocity would be revealed. The amplitude response (Fig. 18) for the 10 times wider inlet channel shows a similar trend as before with the deviation from linear theory near 5 kHz. The lower magnitude of response is due to the lower pressure drop across the inlet channels (the injector response is defined as the ratio of nondimensional mass flow perturbation to pressure perturbation). The phase shift associated shows trends as seen before (Fig. 19). For this reason, the axisymmetric modeling of the discrete number of inlet channels does not explain the discrepancies between the BEM results and the theoretical results.

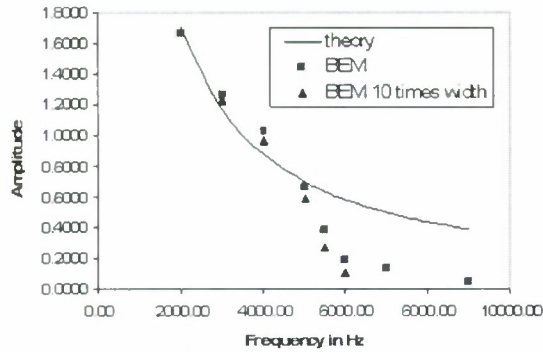


Figure 18. Comparison of amplitude response of the baseline injector with increased inlet channel width W_T while maintaining same mass flow rate.

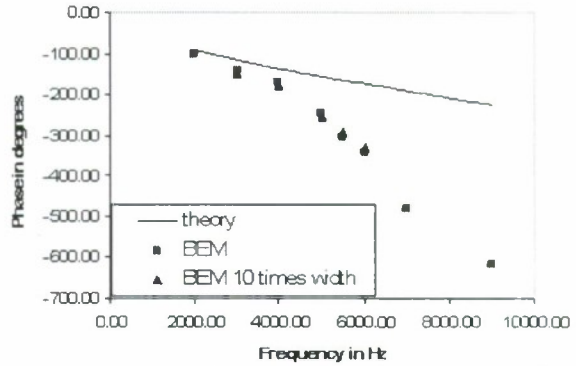


Figure 19. Comparison of phase shift response of the baseline injector with increased inlet channel width W_T while maintaining same mass flow rate.

10. Effect of the varying vortex chamber length

The length of the vortex chamber of the baseline injector was varied from 25–200% to check for multidimensional effects. As Fig. 20 shows, when the length of vortex chamber becomes larger than the liquid thickness ($L_v/h \approx 1$) the amplitude response is no longer dependant on the length of the vortex chamber. Since all previously discussed computations were performed for L_v/h greater than unity, they are free from any significant multidimensional effect.

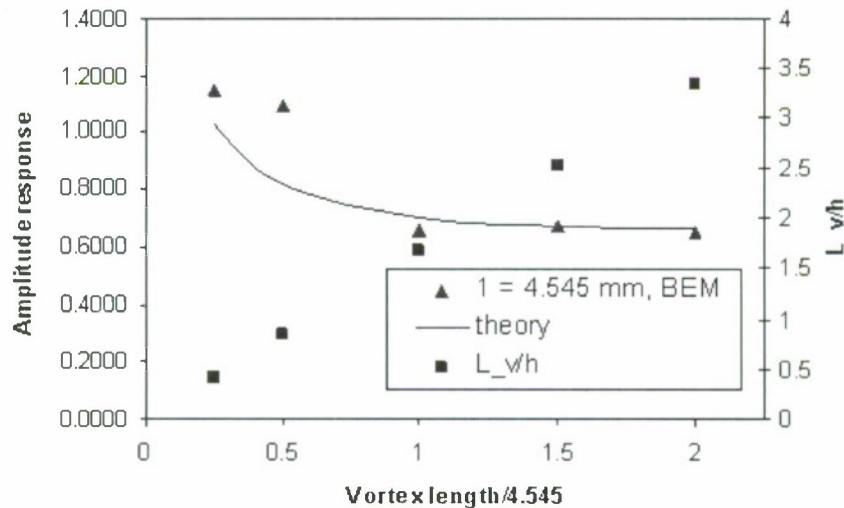


Figure 20. Amplitude responses of various baseline injectors with varying vortex length L_v .

11. Summary of parametric studies

These studies indicate that there are substantial differences between the 2-D computations and the 1-D linear theory over a range of frequencies and that the differences are not attributable to inlet channel modeling or location, nonlinear effects, or multidimensional effects. The one parameter that does indicate a strong scaling is the inlet flowrate or tangential channel injection velocity, and our belief is that the momentum required to turn the tangential entry flow into the axial direction plays a strong role in the differences that are observed. The linear theory does not account for this momentum exchange, and since it would presumably occur over a finite time, there is an opportunity for it to cause an additional lag in the system thereby explaining the observed amplitude/frequency dependence of the multidimensional simulation results. The flow turning phenomenon would presumably scale with injection velocity, i.e., higher injection velocities lead to faster turning and this trend is replicated in the parametric studies. The length scale associated with the turning is much more difficult to assess. We have looked at a number of length scales including the width of the channels, length of the vortex chamber and nozzle and the height of the film, but the overall scaling does not appear to be accurately replicated

considering any of these lengths. Obviously, this important finding needs further research to confirm the hypothesis we put forward.

II. Effect on Drop Size Distributions

A series of simulations were conducted using an imposed massflow pulsation in order to assess the influence on droplet statistics under unsteady injection conditions. Table 4 shows statistical property variation for various oscillation amplitudes at a frequency of $f = 5000$ Hz. Figure 21 shows trends in drop size and number of drops as the pulsation amplitude is increased showing that increased amplitude pulsations lead to formation of smaller droplets. The theory that droplet vaporization/combustion rates can increase under unsteady conditions has long been considered in the combustion instability community and for classical swirl injectors, the recent calculations show merit to this hypothesis. Jet breakup length decreases with oscillation amplitude, which means that the breakup occurs faster before the jet is sufficiently developed. Interestingly, the cone angle also increases in this case since axial velocity decreases largely with increasing amplitude.

The resultant spray development under unsteady inflow conditions is depicted in Fig. 22, for $f = 5000$ Hz, $A = 0.1$, and $t^* = 20.0$. The alternate grouping of droplets (Klystron effect) attributed to alternating regions of faster/slower fluid is readily apparent. Because we have considered a case where axial and radial velocities are nearly equal (cone angle of 90 degrees), the pulsations do not lead to substantial "bushiness" in the cone, but other cone angles may produce larger fluctuations in this quantity under unsteady conditions.

Table 4. Statistical properties according to the oscillation amplitude, $f = 5000$ Hz

Amplitude	$A = 0.0$	$A = 0.5$	$A = 0.1$	$A = 0.3$
SMD/a	0.185	0.179	0.174	0.165
N_D	1741	1910	2104	2948
D_D/a	0.198	0.197	0.198	0.186
\bar{u}_D/U	1.21	1.20	1.17	0.93
\bar{v}_D/U	1.26	1.22	1.24	1.26
θ_D°	45.80	45.47	46.71	53.64

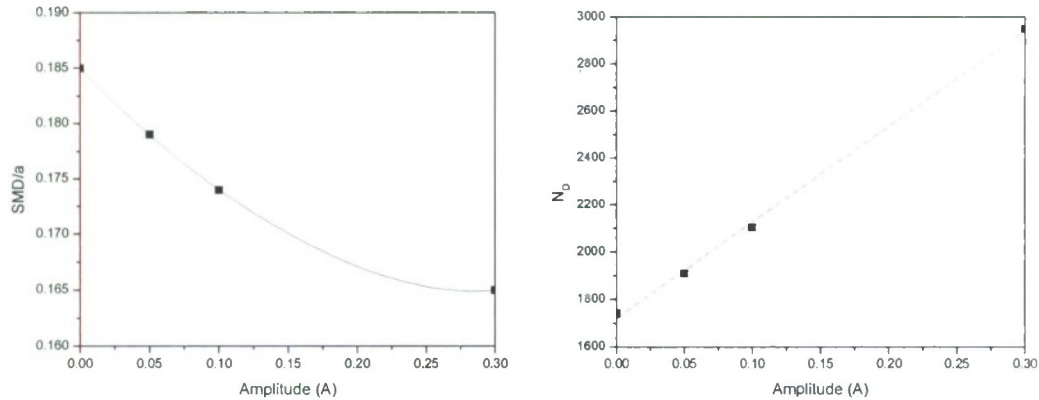


Figure 21. Droplet size (left) and total number of droplets (right) variation with the oscillation amplitude in dynamic response analysis of a classical swirl injector, $f = 5000$ Hz.

IV. Conclusions

A fully nonlinear model based on the boundary element method has been developed to assess the dynamic response of classical swirl injectors. Forced excitation (pulsations of inlet flow) and sympathetic excitation from oscillating downstream/combustion chamber pressure simulations have been conducted to ascertain the nonlinear, multidimensional response function of the injector over a relevant frequency range. In addition, the model has been used in concert with a linear stability analysis for ring breakup to assess droplet fields and drop sizes produced under unsteady injection conditions.

While at low excitation frequencies, the multidimensional nonlinear BEM computations agrees well with the 1-D linear theory, at moderate frequencies, there is a substantial departure in the two treatments with the

nonlinear results giving lower amplitude and larger phase-shifted response. A number of inquiries were made to assess this behavior and the channel width/location, vortex chamber length, and pulsation magnitude (nonlinear effects) were all ruled out as potential contributors. The rolloff behavior is strongly correlated with the injection velocity and it is believed that the time and momentum exchange to create flow turning from tangential to axial direction in the vortex chamber plays a role in explaining discrepancies between the two models.

The dynamic response seems to contain very little nonlinear character and the massflow pulsations scale linearly with imposed pressure perturbation magnitude. For this reason, we see little differences between an imposed massflow pulsation and a sympathetic excitation via an unsteady downstream pressure. The vortex chamber serves as an accumulator in either case and the dynamic flowrate resulting from either excitation produces very similar results. The pulsations in inlet flow are mainly manifested in vorticity waves within the vortex chamber and the overall pulsations in the free surface are quite modest—at least for the geometries and flow conditions studied.

A series of simulations were conducted to assess spray statistics under unsteady inflow conditions. These simulations indicated a strong nonlinear dependence of droplet sizes/SMD values that tended to decrease as the amplitude of the oscillation was increased. Visualizations of the resultant droplet field indicated a prominent Klystron effect with clustering of droplets into discrete regions with a wavelength directly attributable to the pulsation frequency. The unsteady injection conditions led to a reduction in the film breakup length as well.

Appendix A. Theoretical result for dynamics of a swirl injector

V. G. Bazarov's model² provides the theoretical analysis method for dynamic response of the classical injector as shown in Fig. 1. In this model, the tangential channel, the vortex chamber and the nozzle are analyzed independently and then combined to give the overall transfer function of the swirl injector. Then the dynamic response of the classical swirl injector obtained by the 1-Dimensional theoretical model is shown in Fig. A.1 and A.2. Here the analyzed injector has 0.69 MPa pressure drop with pure water and jet speed through inlet is $U = 17.5$ m/s as mentioned early. These results show the interesting characteristic of swirl injectors to provide either amplification or damping of the input disturbance. There is minimal phase shift at very low frequencies, which indicates that the whole swirling liquid responds as a rigid body. As frequency increases, there is an increasing phase shift along with decreasing magnitude of the response. The analysis result provides a good comparison with our calculated result by using BEM code. The theoretically predicted response is shown in Fig. A.1, which is obtained for pressure pulsation in the feed system.

$$\Pi_{\Sigma} = \frac{Q'_n / Q_n}{\Delta P' / \Delta P} \quad (A.1)$$

where Π_{Σ} is defined as the response function of the swirl injector, $\Delta P'$ is the pressure pulsation across the injector, and Q'_n which is the mass flow fluctuation at the nozzle exit. As Π_{Σ} is complex, both the phase and magnitude of the response can be deduced from it. Figure A.2 shows the theoretically predicted dynamic characteristic through each injector component. Thus the combined result of Fig. A.2 gives total characteristics shown in Fig. A.1.

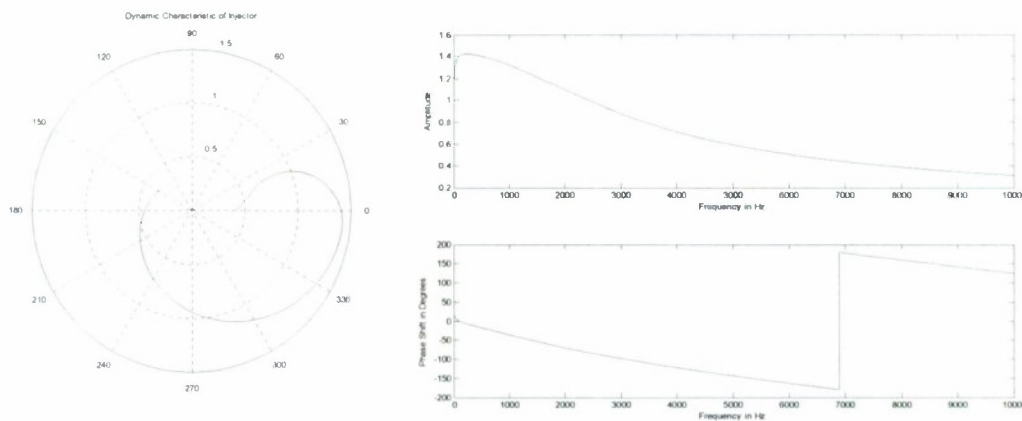
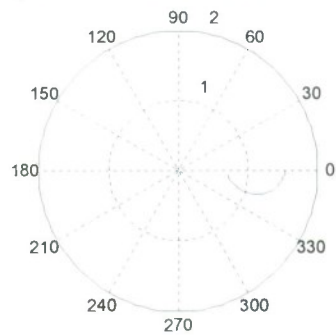
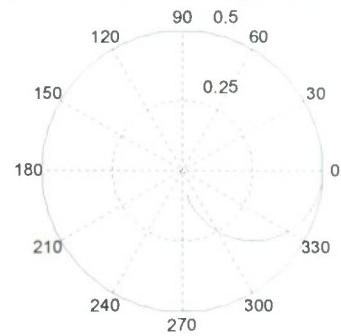


Figure A.1. Theoretically predicted response of a classical swirl injector.

Dynamic Characteristic of Vortex Chamber



Dynamic Characteristic of Tangential Channel



Dynamic Characteristic of Nozzle

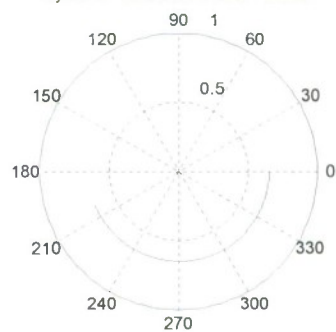


Figure A.2. Theoretically predicted dynamic responses for each injector component.

Acknowledgments

The authors greatly acknowledge the support of the Air Force Office of Scientific Research (Grant number F49620-03-1-0025) with program manager Dr. Mitat Birkan.

References

- ¹Bayvel, L., and Orzechowski, Z., *Liquid Atomization*, Taylor & Francis, Bristol, PA, 1993.
- ²Bazarov, V.G., and Yang, V., "Liquid-Propellant Rocket Engine Injector Dynamics," *Journal of Propulsion and Power*, Vol. 14, No. 5, Sept.-Oct. 1998, pp. 797-806.
- ³Yule, A.J., and Chinn, J.J., "Swirl Atomizer Flow: Classical Inviscid Theory Revisited," *ICLASS-94*, Rouen, France, July 1994.
- ⁴Xue, J., Jog, M.A., Jeng, S.M., Steinhilber, E., and Benjamin, M.A., "Influence of Geometry on the Performance of Simplex Nozzles under Constant Pressure Drop," *ILASS*, Madison, WI, 2002.
- ⁵Park, H., and Heister, S.D., "Nonlinear Simulation of Free Surfaces and Atomization in Pressure Swirl Atomizers," *Physics of Fluids*, Vol. 18, No. 5, 2006, pp. 052103-052103-11.
- ⁶Dash, S.K., Halder, M.R., Peric, M., and Som, S.K., "Formation of Air Core in Nozzles with Tangential Entry," *Journal of Fluids Engineering*, Vol. 123, 2001, pp. 829-835.
- ⁷Bussman, M., Mostaghimi, J., and Chandra, S., "On a Three-Dimensional Volume Tracking Model of Droplet Impact," *Physics of Fluids*, Vol. 11, 1999, pp. 1406-1417.
- ⁸Pasandideh-Fard, M., Bussman, M., Mostaghimi, J., and Chandra, S., "Simulating Droplet Impact on a Substrate Shape," *Atomization and Sprays*, Vol. 11, 2001, pp. 397-414.
- ⁹Han, Z., Parrish, S., Farrell, P.V., and Reitz, R.D., "Modeling Atomization Processes of Pressure-Swirl Hollow-Cone Fuel Sprays," *Atomization and Sprays*, Vol. 7, 1997, pp. 663-684.
- ¹⁰Bazarov, V.G., *Fluid Injector Dynamics*, Mashinostroenie Publication, Inc., Moscow, Russia, 1979.
- ¹¹Yoon, S.S., and Heister, S.D., "A Fully Nonlinear Primary Atomization," *15th Annual Conference on Liquid Atomization and Spray Systems (ILASS)*, held in Madison, Wisconsin, 2002, pp. 36-40.
- ¹²Zhakarov, S.I., Richardson, R., and Heister, S.D., "Hydrodynamic Modeling of Swirl Injectors with Multiple Rows of Tangential Channels," *Joint Propulsion Conference*, Sacramento, CA, July 2006.
- ¹³Park, H., and Heister, S.D., "A Numerical Study of Primary Instability on Viscous High-Speed Jets," *Computers and Fluids*, Vol. 35, No. 10, pp. 1033-1045.

- ¹⁴Park, H., Yoon, S.S., and Heister, S.D., "A Nonlinear Atomization Model for Computation of Drop-Size Distributions and Spray Simulations," *International Journal for Numerical Methods in Fluids*, Vol. 48, No. 11, 2005, pp. 1219-1240.
- ¹⁵Ponstein, J., "Instability of Rotating Cylindrical Jets," *Applied Scientific Research*, Vol. 8, No. 6, 1959, pp. 425-456.
- ¹⁶Spangler, C.A., Hilbing, J.H., and Heister, S.D., "Nonlinear Modeling of Jet Atomization in the Wind-Induced Regime," *Physics of Fluids*, Vol. 7, No. 5, 1995, pp. 964-971.
- ¹⁷Kim, D., Yoon, Y., and Han, P., "Effect of Flow Condition and Geometry on Flow Characteristics of a Swirl Injector," *16th Annual Conference on Liquid Atomization and Spray Systems*, Monterey, CA, May 2003.
- ¹⁸Rump, K., and Heister, S.D., "Modeling the Effect of Unsteady Chamber Conditions on Atomization Processes," *Journal of Propulsion and Power*, Vol. 14, No. 4, 1998, pp. 576-579.

Appendix B – Paper on Nonlinear Response of Multichannel Swirl Injectors

Hydrodynamic Modeling of Swirl Injectors with Multiple Rows of Tangential Channels

Sergey I. Zakharov⁵, Renith Richardson⁶ and Stephen D. Heister⁷
Purdue University, West Lafayette, IN, 47906

Analytic and nonlinear computations have been conducted to study the dynamics of swirl injectors utilizing multiple rows of tangential inlet channels. The study is motivated by the fact that the use of multiple rows of inlets provides a mechanism for wave cancellations within the vortex chamber of the injector, thereby reducing injector response when compared with a single row device. The existing linear inviscid theory has been amended to account for the additional wave interactions arising from two rows of channels within the chamber. In addition, a boundary element method technique has been utilized to study nonlinear aspects of the problem. Results are presented for numerous frequencies in order to characterize the overall response of this injector type.

Nomenclature

Bo	=	Bond number
D_{ij}	=	doublet matrix element
G	=	Green's function
P	=	pressure
q	=	normal velocity
R_v	=	vortex chamber radius
R_{in}, a_o	=	inlet radius of tangential channel
R_c	=	gas core radius
R_n, a	=	nozzle radius
L_T	=	length of tangential channel
L_x	=	length between two inlets
L_n	=	length of nozzle
V_{in}	=	Inlet velocity
r	=	radial direction
s	=	distance along the surface
S_{ij}	=	source matrix element
u	=	axial velocity
v	=	radial velocity
We	=	Weber number
z	=	axial direction
α	=	singular contribution in integral Laplace eq. (Eq. 1)
β	=	surface slope
Γ	=	circulation
κ	=	surface curvature
ϕ	=	velocity potential, phase shift
σ	=	liquid surface tension
ρ	=	density
Π	=	response function
ω	=	angular velocity
ξ	=	equation of a surface wave

⁵ Graduate Research Assistant, School of Aeronautics & Astronautics, 315 N. Grant St., Student Member

⁶ Graduate Research Assistant, School of Aeronautics & Astronautics, 315 N. Grant St., Student Member

⁷ Professor, School of Aeronautics & Astronautics, 315 N. Grant St., Associate Fellow.

Λ = initial amplitude of wave

Subscript

n	=	nozzle
v, vc	=	vortex chamber
T	=	tangential channel
k	=	head end
a	=	inlet 'a'
b	=	inlet 'b'
sw	=	surface waves
vw	=	vorticity waves

Superscript

'	=	dimensional quantity
\wedge	=	perturbation quantity
$-$	=	mean quantity

I. Introduction

THE injector plays a critical role in defining the performance and stability limits of a liquid rocket engine and remains as the one component that lacks predictive tools and design models that aren't based largely/entirely on the behavior of prior designs. The vast majority of prior instability problems have been solved chiefly by making modifications to the injector; it is the component that designers can most readily use to affect the stability characteristics of the engine. The state-of-the-art in injector design relies heavily on empirical data from past designs and linear/empirical models of atomization, secondary atomization, and mixing processes.

The classical theory of the steady-state operation of swirl injectors has been published in numerous contexts¹⁻⁷. These theoretical treatments generally assume a linearized, inviscid flow and provide simple relationships for injector exit conditions (film height, velocity, and conc angle) as a function of fluid parameters and injector design. The results of these models have been compared to experiment and tend to agree well for low-viscosity fluids. Most recently, a nonlinear treatment has been developed to provide additional insight into the steady operation of these devices⁸. While there is still fundamental understanding lacking for viscous and non-Newtonian fluids, the steady operation of the swirl injector is fairly well understood at present.

The dynamics of swirl injectors have been much less studied. In combustion systems, the injector can participate as an active element and this has motivated the limited analyses that have been conducted. Simple drilled orifice response has been characterized in the 1960's and 1970's⁹⁻¹¹ using linear models. Because many of their liquid rocket engines employed this injector type, the Russians were one of the early developers of theories related to the dynamics of swirl injectors. Much of the published work stemming from these efforts is due to Dr. V. Bazarov and his collaborators¹²⁻¹⁵. In these works, the waves formed in the vortex chamber due to unsteady flowrate interact with the convergent section forming the nozzle and transmit pulsations of massflow as a result of either forced excitation or passive excitation via an unsteady downstream pressure. Recently, a patent appeared for the injector style used in many of the Russian booster engines¹⁶. This patent revealed a design implementing two rows of tangential inlet channels feeding an open nozzle design injector in which the vortex chamber has the same internal diameter as the nozzle section. The design permits wave cancellations at selected frequencies where the wavespeed and row spacing provide a destructive interference of waves generated from the two rows of inlets. This design approach can be attractive to reduce injector response at known acoustic frequencies for a given combustor design.

The motivation of the current study is to amend the linear theory to account for this design feature and to construct a nonlinear model as a basis for comparison with the linear results. Both tools are then applied to a candidate injector design to evaluate its performance over a range of frequencies. The following sections provide descriptions of the computational model, the analytic tool, and results from exercising these tools for a given injector design.

II. Computational Model

A. BEM Method for a Swirling flow

Figure 1 provides a schematic of a classical simplex atomizer noting the fluid injection via tangential channels at the head end of the vortex chamber. The gas core develops naturally as a function of the vortex chamber diameter, inlet massflow and the degree of swirl imparted to the fluid. The contraction to the nozzle facilitates acceleration and thinning of the film to provide a conical sheet that breaks up into a spray. Key dimensions and nomenclature are noted in Fig. 1 for application to the analysis and subsequent discussion.

Yoon and Heister¹⁷ and Park¹⁸ provide a complete description of the basic model elements; only highlights will be presented here in the interest of brevity. An inviscid, incompressible, axisymmetric flow is presumed such that the flow dynamics are governed by Laplace's equation, $\nabla^2\phi = 0$. The boundary element method utilizes an integral representation of this equation to provide a connection between ϕ values on the boundary, the local geometry, and the local velocity normal to the boundary, $q = \partial\phi/\partial n$, as follows:

$$\alpha\phi(\vec{r}_i) + \int_S \left[\phi \frac{\partial G}{\partial \hat{n}} - qG \right] ds = 0 \quad (1)$$

where $\phi(\vec{r}_i)$ is the value of the potential at a point \vec{r}_i , S is the boundary of the domain, α is the singular contribution when the integral path passes over the "base point", and G is the free space Green's function corresponding to Laplace's equation. For an axisymmetric domain, the free space Green's function can be expressed in terms of elliptic integrals of the first and second kinds and is a function solely of the instantaneous surface geometry. For this reason, a discrete representation of Eq.(1) can be cast as a linear system of equations relating local ϕ and q values. In the discretization, both ϕ and q are assumed to vary linearly along each element, thereby providing formal second-order accuracy for the method. Since the resulting integrals do not have exact solutions in this case, Gaussian quadrature is used to maintain high accuracy of integration and preserve second-order accuracy overall.

While this governing equation is a linear, nonlinearities in these free surface problems enter through the boundary condition at the interface. The unsteady Bernoulli equation provides a connection between the local velocity potential and the surface shape at any instant in time. Prior formulations^{17,18} have provided a derivation of this result suitable for implementation in a Lagrangian surface tracking environment. For the swirling flow, modifications are required to account for the centrifugal pressure gradient created by the swirl. The dimensionless unsteady Bernoulli equation is as follows,

$$\frac{D\phi}{Dt} = \frac{1}{2}|\vec{u}_t|^2 - \vec{u}_t \cdot \vec{u}_v - P_g - \frac{\kappa}{We} + \frac{Bo}{We}z \quad (2)$$

where ϕ is the velocity potential and κ is the local surface curvature and the Weber number ($We = \rho U^2 a / \sigma$) and Bond number ($Bo = \rho g a^2 / \sigma$) become the dimensionless parameters governing the problem. Physically, this result is a Lagrangian form suitable for use for fluid elements moving with the local velocity of the free surface. The terms on the RHS of the equation include the effect of dynamic pressure, local gas-phase pressure, capillary, and hydrostatic pressure contributions respectively. In Eq.(2), the total surface velocity, \bar{u}_t , can be computed via a superposition of the base axial flow in the injector (ϕ, \bar{u}) with a potential vortex (ϕ_v, \bar{u}_v). Letting u, v, w represent axial, radial, and circumferential velocity components respectively, we may write:

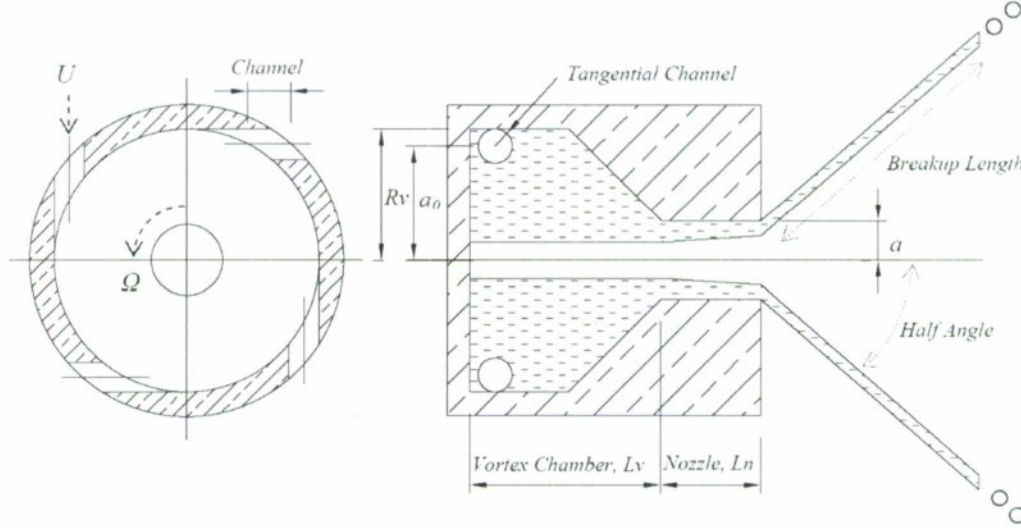


Figure 1. A classical swirl injector noting nomenclature used for design variables

$$\phi_t = \phi + \phi_v \quad u_t = u + u_v \quad v_t = v + v_v \quad w_t = w + w_v \quad (3)$$

Superposition of a potential vortex can be achieved by starting with the complex potential:

$$F(z) = -\frac{i\Gamma}{2\pi} \log(z) \quad (4)$$

where z is complex variable, Γ is vortex strength, and F is the complex potential. The resulting velocity components for this flow are as follows,

$$u_v = 0, \quad v_v = 0, \quad w_v = \frac{\Gamma}{2\pi r} \quad (5)$$

This vortex is irrotational as known since $\bar{\omega} = \nabla \times \bar{u} = 0$, except at $\bar{r} = 0$. Using Eq.(5), the total velocity in Eq.(3) can be computed;

$$\begin{aligned} \frac{1}{2} |\bar{u}_t|^2 - \bar{u}_t \cdot \bar{u}_t &= \frac{1}{2} [(u + u_v)^2 + (v + v_v)^2 + (w + w_v)^2] &= \frac{1}{2} [u^2 + v^2 + w^2] - w_v \cdot w_v \\ &- [(u + u_v) \cdot u_v + (v + v_v) \cdot v_v + (w + w_v) \cdot w_v] &= \frac{1}{2} [u^2 + v^2] - \frac{1}{2} w_v^2 \end{aligned} \quad (6)$$

where

$$\frac{1}{2} w_v^2 = \frac{1}{2} \left(\frac{\Gamma}{2\pi r} \right)^2 = \frac{1}{2} \left(\frac{2\pi a_0 U}{2\pi r} \right)^2 = \frac{1}{2} \left(\frac{a_0 U}{r} \right)^2 \quad (7)$$

Choosing the ideal injection velocity (U), the orifice radius (a), and liquid density (ρ) as dimensions, the dimensionless result can be written as,

$$\frac{D\phi}{Dt} = \frac{1}{2} |\bar{u}|^2 - P_g - \frac{\kappa}{We} + \frac{Bo}{We} z - \frac{1}{2} \left(\frac{a_0}{a} \right)^2 \frac{1}{r^2} \quad (8)$$

where the Weber and Bond numbers are defined as above. In addition, the $[u^2 + v^2]$ of base flow is simplified as $|\vec{u}|^2$. Since we have nondimensionalized against the tangential velocity, U , the Rossby number does not appear explicitly in Eq.(8), but the last term on the *RHS* of the equation corresponds to the circumferential pressure developed by the potential vortex. In this context, the radial location of the center of the tangential channel, a_o , defines the dimensionless strength of the vortical flow. The kinematic equation for motion of points on the free surface can be expressed:

$$\frac{Dz}{Dt} = \frac{\partial \phi}{\partial s} \cos \beta - q \sin \beta \quad \frac{Dr}{Dt} = \frac{\partial \phi}{\partial s} \sin \beta + q \cos \beta \quad (9)$$

where β is the local slope of the wave with respect to the horizontal direction. Equations (8) and (9) are integrated in time using a 4th-order Runge-Kutta scheme to provide the evolution of the velocity potential and the motion of the free surface.

For long integrations or resolution of highly distorted surfaces, points on the free surface will tend to bunch in regions of higher curvature as a result of the free-surface motion. For this reason, the points on the free surface are redistributed at each time step using a cubic spline fitting of the instantaneous shape. The Laplace equation is solved to update velocities and the process is marched forward in time. Formally, the resolution of the scheme is second-order in space and 4th-order in time, but surface curvature and capillary forces are resolved with 4th-order accuracy given a set of points defining the instantaneous shape. More details regarding the numerical procedure can be found in Yoon and Heister.¹⁷

B. Oscillating Pressure Boundary Conditions and Domain Discretization

The computational model was upgraded to address the more realistic condition involving an oscillating chamber pressure. This boundary condition will allow orifice massflows to adjust naturally to the instantaneous pressure within the vortex chamber. In order to implement these physics into BEM code we need to know how inflow responds to changes in chamber pressure. This can be done using a potential vortex approximation.

From the radial momentum equation, $\frac{V_o'^2}{R'} = \frac{1}{\rho'} \frac{\partial p'}{\partial R'}$, there for the potential vortex: $V_o' = \frac{\Gamma'}{2\pi R'}$

After integration the dimensional pressure drop across the liquid film can be computed using the following equation:

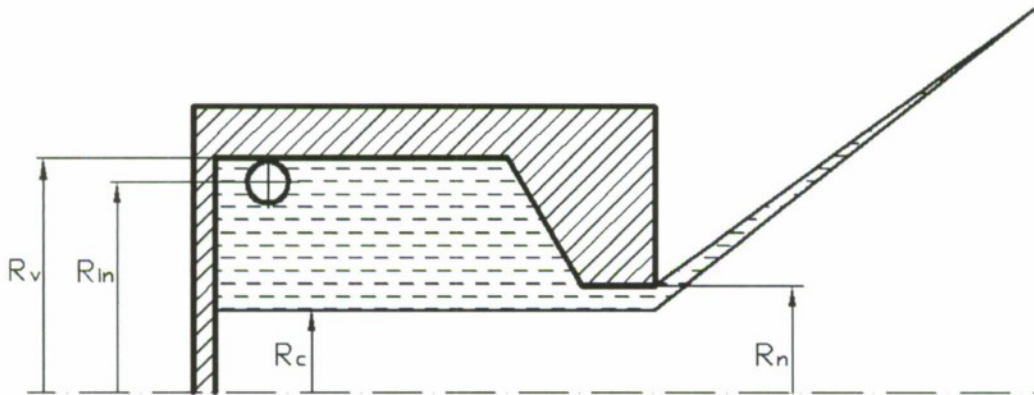


Figure 2. Schematic of a classical swirl injector

$$\Delta P_1' = -\frac{\rho \Gamma'^2}{8\pi^2} \left(\frac{1}{R_m'^2} - \frac{1}{R_c'^2} \right)$$

So that the nondimensional pressure drop can be written:

$$\Delta P_1 = -\frac{\Gamma^2}{8\pi^2} \left(\frac{1}{R_m^2} - \frac{1}{R_c^2} \right)$$

Substituting nondimensional circulation $\Gamma = 2\pi R_{in} V_{\theta} = 2\pi R_{in} V_{in}$ we obtain:

$$\Delta P_1 = -\frac{R_{in}^2 V_{in}^2}{2} \left(\frac{1}{R_{in}^2} - \frac{1}{R_C^2} \right) = \frac{V_{in}^2}{2} \left(\frac{R_{in}^2}{R_C^2} - 1 \right) \quad (10)$$

Assuming a constant stagnation pressure in the manifold and neglecting viscosity losses, Bernoulli's equation gives us pressure drop across the inlet channel: $\Delta P_2 = \frac{V_{in}^2}{2}$

So the total pressure drop across injector is the sum of pressure drops across the liquid film and inlet channel:

$$\Delta P = \Delta P_1 + \Delta P_2 = \frac{V_{in}^2}{2} \frac{R_{in}^2}{R_C^2} \quad (11)$$

Knowing this pressure drop inflow velocity can be computed as:

$$V_{in} = \sqrt{2\Delta P} \frac{R_C}{R_{in}} \quad (12)$$

Where pressure drop is assumed to be a sinusoidal function of time $\Delta P = \Delta P_{Steady} + \varepsilon \sin(\omega t)$, where steady state pressure drop is calculated from the initial conditions:

$$\Delta P_{Steady} = \frac{q_{mean}^2 R_{in}^2}{2R_{C_steady}^2} \quad (13)$$

Figure 3 shows a typical computational grid employed in the studies. Initial pressure drop is computed from Eq. (12) based on steady state solution for the core radius using constant inflow rate. This pressure drop plus perturbation is further converted to massflow on the inlet boundary using Eq. (13). This approach is used for both channels so each of them sees different pressure drop depending on the local core radius. Nodes on solid walls are subject to the flow tangency condition ($q=0$), and nodes of the free surface are subject to the Bernoulli condition derived in Eq.(8). The node lying at the free surface junction with the head-end of the vortex chamber is treated as a moving node such that the free surface remains perpendicular to the wall at this location. The grid spacing along the head-end of the vortex chamber is stretched to accommodate movement of the corner node.

C. Solution at interior nodes

Outflow rates in the nozzle can be computed using velocities at two boundary points and assumption of linear velocity profile. However this approach is not accurate and results in up to a 3% error based on numerical experiments. In order to improve the accuracy we need to know velocity profile what requires to use an additional approach in order to get interior velocities. As in the solution for conditions at nodes on the boundary, the solution at interior nodes is made up of the following parts: the development of integral equation for the Green's function, the integration and the calculation of the solution for unknown values of velocity potential and it's derivatives.

To compute φ on the interior points equation (1) can be rearranged to give

$$\varphi_i = \frac{1}{4\pi} \int_{\Gamma} \left[\varphi \frac{\partial G}{\partial n} - qG \right] d\Gamma \quad (14)$$

After discretization it becomes:

$$2\pi\varphi_i = D_{i,j}\varphi_j - S_{i,j}q_j \quad (15)$$

Where i denotes interior nodes and j denotes nodes on the boundary. For any individual interior node D and S become row vectors known from the solution on the boundary, so φ can be found from this equation.

In order to find velocities we need to compute derivatives $\frac{\partial \phi}{\partial z}$ and $\frac{\partial \phi}{\partial r}$ which

can be evaluated by analytical differentiation of equation (14) with respect to z and r . New integrals, resulting from the differentiation of the Green's function in the z, r directions, result from this process. Ref. 19 and Ref. 20 provide a detailed discussion of the methodology employed to discretize these integrals.

After upgrading the code with this methodology, the axial velocity profile at the nozzle exit plane can be defined and integrated to provide the overall massflow produced by the device at a given instance in time. Evaluation of this approach, using simple trapezoidal quadrature to integrate the velocity profile, shows that computed time averaged inflow and outflow differ by less than 0.1% using approximately the same grid spacing for both exterior and interior nodes. Since we need to place interior nodes only along a radial line in the nozzle where liquid film is very thin, the number of additional nodes was about 10-15 in comparison to more than 300 surface nodes. Along with the fact that matrix inversion is not required on the interior, effect on computational time was negligible but accuracy increased more than an order in magnitude.

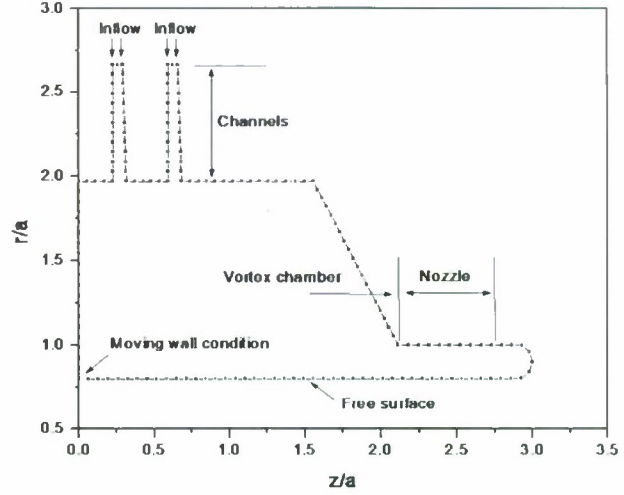


Figure 3. A grid system having two inlet channels

Along with the fact that matrix inversion is not required on the interior, effect on computational time was negligible but accuracy increased more than an order in magnitude.

III. Analytical Model

A. Single channel

The linear model of the pressure swirl atomizer consists of 3 components namely, tangential channels, vortex chamber and nozzle. This analytical model was used to analyze the injector shown in Figure 1 and was developed by Bazarov².

The tangential channels are modeled as a pressure atomizer whose length is much less than the wavelength of oscillation.

$$\Pi_T = \frac{V_T}{\Delta P_T} = \frac{1}{2} \frac{1 - \frac{i\omega L_T}{V}}{\left[1 + \left(\frac{i\omega L_T}{V}\right)^2\right]} = \frac{1}{2} \frac{1 - iSh_T}{1 + Sh_T^2} \quad (16)$$

Where Π_T is defined as response of tangential channel and $Sh_T = \frac{\omega L_T}{V}$ as Strouhal number of tangential channel.

There are two phenomena being considered in the vortex chamber. Firstly the oscillations in liquid flow rate in tangential channels \dot{m}_T , produces 'Surface Waves' in the vortex chamber which propagates back and forth as it reflects from the entrance of the nozzle. Secondly we have what are called 'Vorticity Waves' which refers to the fluid regions swirling with different velocities due to \dot{V}_T in the vortex chamber. The vorticity waves strongly depends on radial velocity in the vortex chamber. The pressure drop in the vortex chamber ΔP_{vc} is the vector sum of the pressure drop due to surface waves ΔP_{v-sw} and vorticity waves ΔP_{v-vw} .

The nozzle is assumed to be short and any losses (no pressure or viscous losses) in it are neglected. The thickness of liquid through it is considered to be constant, so any effect due to 'vorticity waves' is negligible.

There is only phase shift in the surface waves when it travels through the nozzle of length L'_n given by $\psi_n = \frac{\omega L'_n}{V'_{wn}}$. Therefore the response of the nozzle would be

$$\Pi_n = \frac{\hat{m}'_n}{\hat{m}'_{vn}} = (1 - \Pi) e^{-i\psi_n} \quad (17)$$

Where \hat{m}'_n & \hat{m}'_{vn} are mass flow rate fluctuations in the nozzle and near the nozzle entrance respectively. Π is the reflection coefficient i.e. the percentage of wave which reflects back from the contraction leading up to the nozzle. Combining the individual responses of the components gives the response of the swirl injector (Eq.18). A more thorough description can be found in Bazarov²¹.

$$\Pi_{total} = \frac{\hat{m}'_n / \hat{m}'_n}{\Delta P' / \Delta P'} = \frac{R_v^2}{a} \frac{\Pi_T \Pi_{vn-sw} \Pi_n}{1 + 2\Pi_T (\Pi_{k-sw} + \Pi_{v-vr})} \quad (18)$$

Here a is a geometric parameter and $\Delta P'$ is the pressure drop across the swirl injector. The total response Π_{total} is complex; hence both amplitude and phase can be deduced from it.

B. Modified model for dual channel injector

Consider a swirl injector with two rows of tangential injectors separated from each other by a distance L_x (Figure 4). We assume that the response of the tangential channels and nozzle are unchanged (with respect to single row of inlets) with the introduction of another row of inlet. Also the any modification needed due to the 'vorticity' effect in the vortex chamber is neglected as it is found to be negligible. However the interaction of the surface waves in the vortex chamber has to be accounted for. See Richardson²² for a detailed analysis of a two channel swirl injector.

The phase shift associated with the distance between the two inlet channels L_x is given by,

$$\phi_x = \frac{\omega L'_x}{V'_{wv}} \quad (19)$$

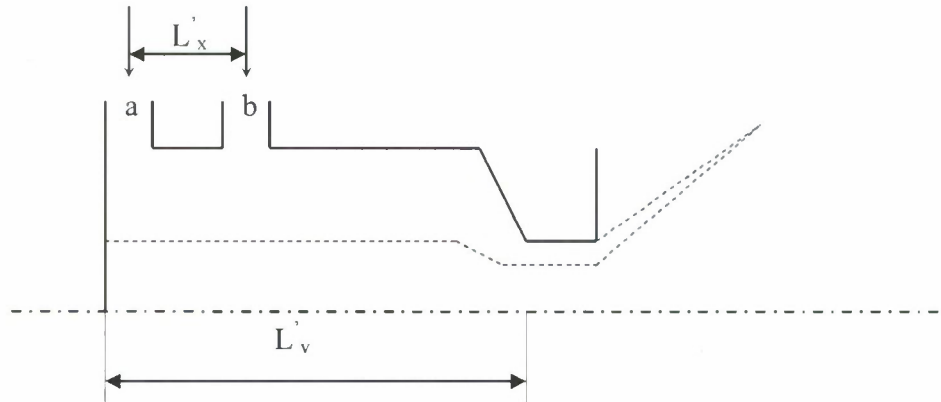


Figure 4. A classical swirl injector with two inlets at locations 'a' & 'b' separated by a distance L_x

Where angular velocity, $\omega = 2\pi f$ and V'_{wv} is the wave velocity in the vortex chamber.

We can use the principle of superposition to examine the influence of reflected waves in the vortex chamber of any arbitrary length. Let us consider an initial wave in the vortex chamber at inlet 'a' given by

$$\xi_{vh_1} = \Lambda_a e^{i\omega t} \quad (20)$$

Where Λ_a is the initial height of the wave due to the perturbation in the inlet 'a'. Near the nozzle this wave travels a distance of L'_v (length of Vortex Chamber) and becomes,

$$\xi_{vm_1} = \Lambda_a e^{i(\omega t - \phi_v) - \nu \phi_v} \quad (21)$$

Where ϕ_v the shift angle is associated with traveling L'_v distance and $\nu \phi_v$ is the reduction in the amplitude due to viscosity ν . A part of this wave gets reflected which is given by,

$$(\xi_r)_{vm_1} = \Pi \Lambda_a e^{i(\omega t - \phi_v) - \nu \phi_v} \quad (22)$$

Where Π is the reflection coefficient. This reflected wave changes in the following manner when it travels a length L'_v to reach the closed end of the Vortex Chamber

$$\xi_{vm_2} = \Pi \Lambda_a e^{i(\omega t - 2\phi_v) - 2\nu \phi_v} \quad (23)$$

This wave is reflected completely from the closed end and reaches the nozzle,

$$\xi_{vm_2} = \Pi \Lambda_a e^{i(\omega t - 3\phi_v) - 3\nu \phi_v} \quad (24)$$

The reflected wave will be,

$$(\xi_r)_{vm_2} = \Pi^2 \Lambda_a e^{i(\omega t - 3\phi_v) - 3\nu \phi_v} \quad (25)$$

And so the waves reflect back and forth until their amplitudes become negligibly small.

Using the principle of superposition we have the following wave near the closed end of the vortex chamber,

$$\xi_{vh} = \Lambda_a \sum_{n=0}^{\infty} \Pi^n e^{i(\omega t - 2n\phi_v) - 2n\nu \phi_v} \quad (26)$$

Near the nozzle,

$$\xi_{vm} = \Lambda_a \sum_{n=0}^{\infty} \Pi^n e^{i(\omega t - (2n+1)\phi_v) - (2n+1)\nu \phi_v} \quad (27)$$

Similarly we can derive equations for surface waves in the vortex chamber due to the perturbations in the inlet channel 'b'.

Then, using the principle of superimposition we can compute the wave near the head end of vortex chamber as follows

$$\xi_{vh} = \Lambda_a \sum_{n=0}^{\infty} \Pi^n e^{i(\omega t - 2n\phi_v) - 2n\nu \phi_v} + \Lambda_b \sum_{n=0}^{\infty} \Pi^n e^{i(\omega t - 2n\phi_v + \phi_v) - 2n\nu \phi_v + \nu \phi_v} \quad (28)$$

Similarly near the nozzle inlet we have

$$\xi_{vm} = \Lambda_a \sum_{n=0}^{\infty} \Pi^n e^{i(\omega t - (2n+1)\phi_v) - 2n\nu \phi_v} + \Lambda_b \sum_{n=0}^{\infty} \Pi^n e^{i(\omega t - (2n+1)\phi_v + \phi_v) - (2n+1)\nu \phi_v + \nu \phi_v} \quad (29)$$

The above two equations are used in computing the response of the dual channel injector in conjunction with Eq.(18).

IV. Results

A. Single channel

A single channel swirl injector was analyzed using the linear model and compared with computational results generated by BEM code described in section II using oscillation pressure boundary conditions. A general but realistic injector was chosen whose design parameters are given in Table I. A time step of 0.0003 along with

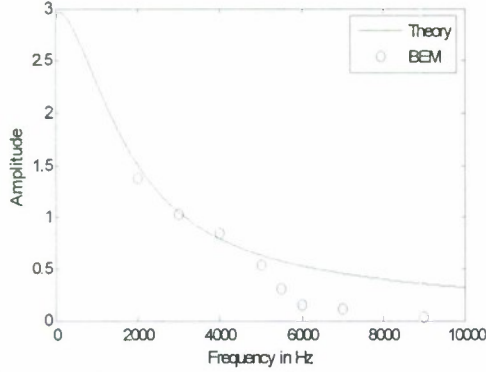


Figure 5. Amplitude vs Frequency

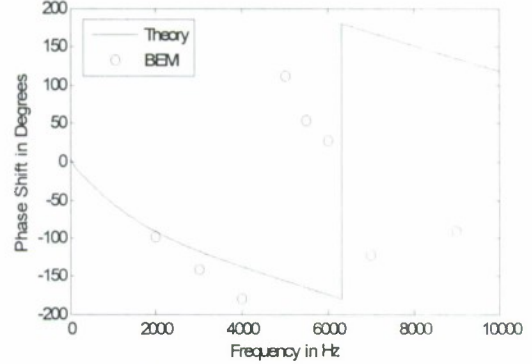


Figure 6. Phase angle vs Frequency

a nodal spacing of 0.032 was used. Each computation was allowed to run for 15 sec which took approximately 4 days of CPU time. The nodal spacing and time step are optimized for reducing run time without affecting the output. See Richardson²² for details.

Inlet radius of tangential channel	$R'_{in} = 0.1270$ in
Radius of nozzle	$R'_n = 0.085$ in
Radius of vortex chamber	$R'_v = 0.1667$ in
Radius of tangential channel	$R'_T = 0.0253$ in
Length of tangential channel	$L'_T = 0.0597$ in
Length of nozzle	$L'_n = 0.059$ in
Length of vortex chamber	$L'_v = 0.179$ in
No of inlet channels	$n = 4$
Inlet velocity	$V'_T = 690$ in/s

Table 1. Design parameters of single channel swirl injector

The amplitude predicted by linear theory is in close agreement with computational results for frequency range < 5 kHz (Figure 5.) However at higher frequencies the computations predict a much more stable injector. Possible causes could be the time taken to turn the flow from the tangential channel to vortex chamber (90° turn) and associated phase shift for this. From Figure 6 we see that the change in phase between theoretical and BEM code results are higher after ~ 5 kHz. Another probable cause could be non-linear effects playing more significant role in the stability of the injector at higher frequencies of operation.

B. Dual Channel results

A dual channel swirl injector was analyzed using the modified linear model and compared with computational results generated by BEM code described in section II using oscillation pressure boundary conditions. An injector currently being tested by Miller²³ at Purdue University was used as basis for this study (Table 2).

Inlet radius of tangential channel	$R'_{in} = 0.454$ in
Radius of nozzle	$R'_n = 0.454$ in
Radius of vortex chamber	$R'_v = 0.454$ in
Radius of tangential channel	$R'_T = 0.0175$ in
Length of tangential channel	$L'_T = 0.359$ in
Length of nozzle	$L'_n = 0.0$ in
Length of vortex chamber	$L'_v = 0.4767$ in
Length between two channels	$L'_x = 0.0999$ in
No of inlet channels	$n = 8$
Inlet velocity	$V'_T = 913$ in/s

Table 2. Design parameters of a dual channel swirl injector

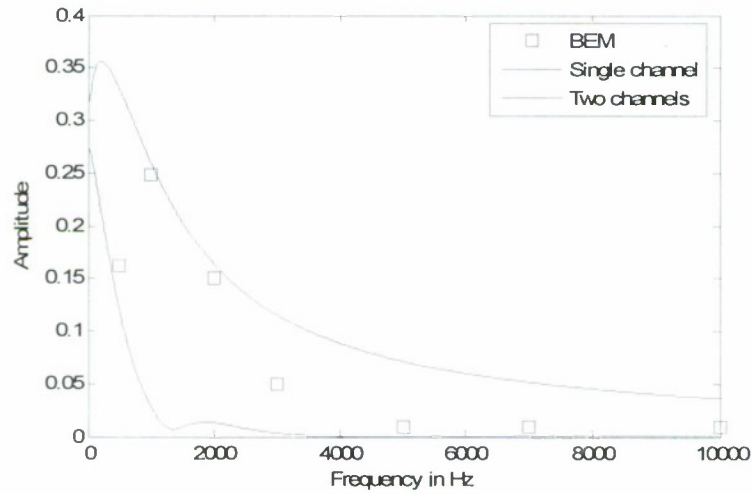


Figure 7. Amplitude vs Frequency for dual channel swirl injector

Since the injector to be analyzed is an 'open' injector that is the radius of vortex chamber and nozzle being equal further modification where required to the existing model. The effect due to reflection coefficient Π was eliminated (set to a very small value) and the nozzle length was set to an insignificant value. The flow was shared equally among both the inlet channels.

The linear model shows a local minima around 1344 Hz (Figure 7,8). This frequency corresponds to the distance between the two inlets $L_x = 0.1$ in. The amplitude of response is never greater than unity; this is a feature of the 'open' injector which makes it more attractive option over the 'classical' swirl injector. The dual channel injector is much more stable than the single inlet design due to the destructive interference of the surface waves in the vortex chamber. The computational results seem bounded by the single and dual channel analytical analysis for the same design parameters.

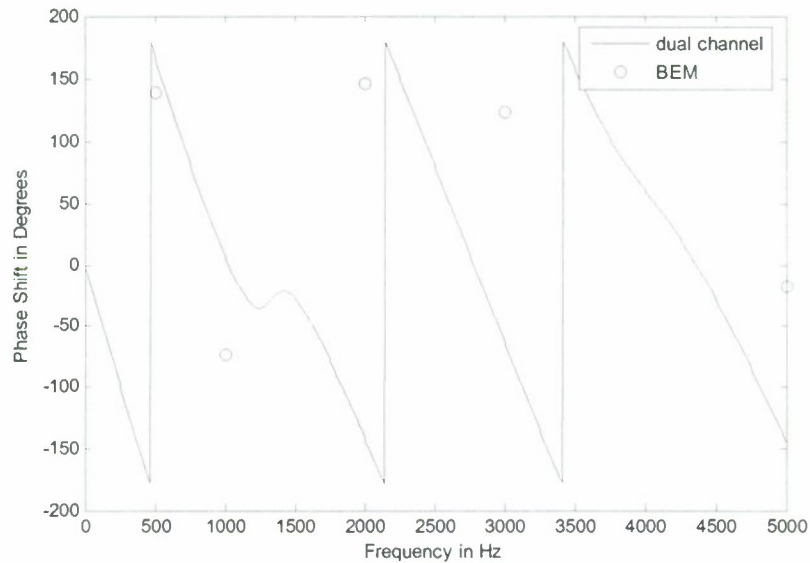


Figure 8. Phase shift vs frequency for dual channel injector

At low frequencies (< 1000 Hz) the interference of surface waves is more prominent owing to longer wavelengths and fewer waves in the vortex chamber. However at higher frequencies the computational model shows a diminishing effect of the two channel inlet probably due to decreasing wavelengths of the surface waves and probably the simple dual channel analysis seems inadequate to capture all the phenomena in the vortex chamber. Also the non-linear effects are not being accounted for in the theoretical model.

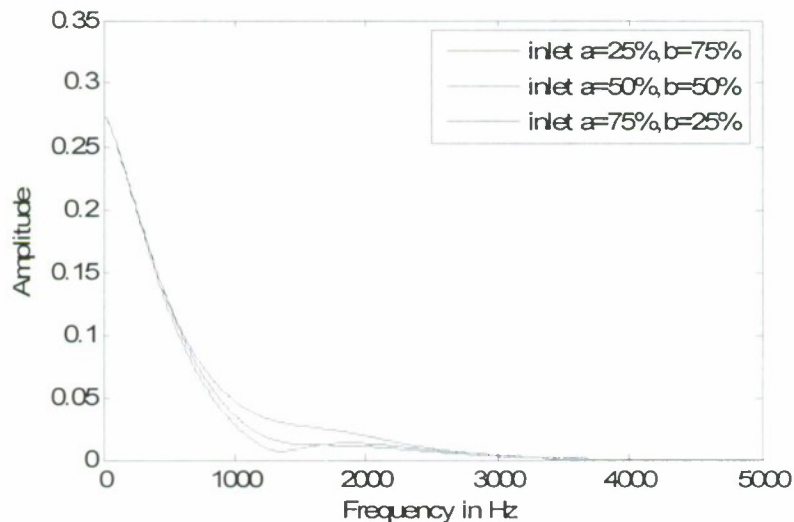


Figure 9. Amplitude vs frequency for different combinations of flow through the two

The amount of mass flow rate (Fig. 9) was varied among the two sets of inlets. A 50-50 split shows to be the most stable combination with clear local minima at 1344 Hz. Other combinations are a little less stable than the 50-50 split and also don't show any clear local minima.

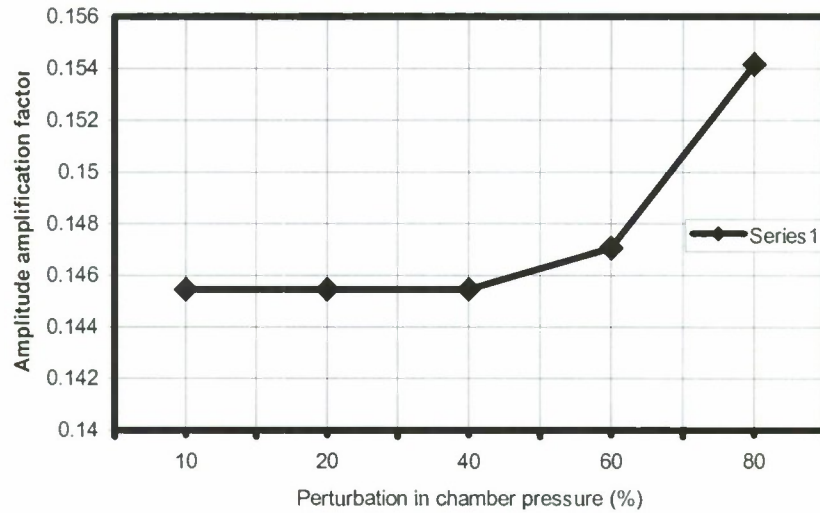


Figure 10. Amplitude vs perturbation

Fig. 10 shows BEM results for amplitude amplification factor (ratio of outflow to inflow perturbation magnitudes) as a function of chamber pressure perturbations for the frequency of 2000 Hz. As we can see even 80% perturbation causes nonlinearity of just above 5%.

Conclusion

The dynamics of swirl injectors utilizing multiple rows of inlet channels have been addressed using linear theory and nonlinear axisymmetric boundary element method calculations. The use of multiple inlet channels is believed to provide a mechanism to cancel waves and hence injector unsteadiness at specific frequencies. Computations have been conducted for a candidate design over the relevant frequency range to assess the overall phase and amplitude response of these injectors. For designs making use of a single row on inlet channels, the linear theory and the nonlinear BEM results agree quite well at low frequencies, with substantial departure in both amplitude and phase at higher frequencies. This departure is theorized to be due to flow turning within the vortex chamber that is not presently considered in the linear model. The two-channel results show much greater disparity as the complex wave interactions are not all considered in the modified linear model. In addition, the disparity in results may also be attributed to flow turning effects that alter the phasing of the waves emanating from the two injection regions. Additional study is required to further illuminate this issue. Finally, a series of BEM computations were conducted to assess the effect of perturbation amplitude on the response of the device, i.e. nonlinear effects. The results show that high amplitude forcing is required to cause a substantial departure from the linear result.

Acknowledgments

The authors gratefully acknowledge the support of AFOSR Contract F49620-03-1-0025 under program manager, Dr. Mitat Birkan for their support of this work.

References

1. Yule, A. J., and Chinn, J. J., "Swirl Atomizer Flow: Classical Inviscid Theory Revisited", *ICLASS-94*, Rouen, France, July 1994
2. Taylor, G. I., "The Mechanics of Swirl Atomizers", *7th Int. Congress of Applied Mechanics*, Vol. 2., Sept 1948
3. Giffen, E., and Muraszew, A., "Atomization of Liquid Fuels", Chapman and Hall London, 1953
4. Lefebvre, A. H., "Atomization and Spray", Hemisphere, Washington 1989
5. Bayvel, L., and Orzechowski, A., "Liquid Atomization", Taylor and Francis, 1993
6. Khavkin, Y. I., "Theory and Practice of Swirl Atomizers", Taylor and Francis, 1989
7. Dumas, M., and Laster, R., "Liquid-Film Properties for Centrifugal Spray Nozzles", *Chemical Engineering Progress*, Vol. 49, No. 10, October, 1953.
8. Park, H., and Heister, S. D., "Nonlinear Simulation of Free Surfaces and Atomization in Pressure Swirl Atomizers", to appear, *Physics of Fluids*, 2006.
9. Reba, I., Brosilow, C., "Combustion Instability: Liquid Stream and Droplet Behavior. Part III: The Response of Liquid Jets to Large Amplitude Sonic Oscillations," WADC Technical Report 59-720, Wright Air Development Center, United States Air Force, 1960.
10. Harrje, D., Reardon, F. "Liquid Propellant Rocket Combustion Instability," NASA SP-194, 1972.
11. "Liquid Rocket Engine Injectors," NASA SP-8089, 1976.
12. Bazarov, V., Yang, V., "Liquid-Propellant Rocket Engine Injector Dynamics," *Journal of Propulsion and Power*, Vol. 14, No. 5, September–October 1998.
13. V. G. Bazarov and L.A. Lyul'ka, "Nonlinear Interactions in Liquid Propellant Rocket Engine Injectors", AIAA 98-4039, 1998.
14. Bazarov, V. G., "Liquid-Propellant Rocket Engine Injector Dynamics", *Journal of Propulsion And Power* Vol. 14, No. 5, Sept-Oct 1998
15. Bazarov, V. G., "Fluid Injectors Dynamics", Mashinostroic Publication, Inc., Moscow, Russia, 1979
16. Vasin, A., et. al., United States Patent, US 6,244,041 B1, 12 June, 2001.
17. Yoon, S. S., and Heister, S. D., "A Fully Nonlinear Model for Atomization of High-Speed Jets," *Engineering Analysis with Boundary Elements*, V28, pp 345-357, 2004.
18. Park, H. B., "Flow characteristics of viscous high-speed jets in axial/swirl injectors", PhD Thesis Dept. of Aeronautics and Astronautics, Purdue University, 2005
19. Rump, K. M., and Heister, S. D., "Modeling the Effect of Unsteady Chamber Conditions on Atomization Processes," *Journal of Propulsion and Power*, V. 14, pp. 576-578, 1998.
20. Heister, S. D., Rutz, M., and Hilbing, J., "Effect of Acoustic Perturbations on Liquid Jet Atomization," *Journal of Propulsion and Power*, V. 13, No. 1, pp. 82-88, 1997.
21. Bazarov, V. G., "Fluid Injectors Dynamics", Mashinostroic Publication, Inc., Moscow, Russia, 1979
22. Richardson, R., "Linear and Non Linear Dynamics of Swirl Injectors" PhD Thesis, Department of Aeronautics and Astronautics, Purdue University, August 2006
23. Miller J, K., "Experimental Study of Longitudinal Instabilities in a Single Element Rocket Combustor", MS Thesis, Department of Aeronautics and Astronautics, Purdue University, May 2005

Appendix C – Paper on Linear Stability of Compound Jets

On the Linear Stability of Compound Capillary Jets

Maksud (Max) Ismailov* and Stephen D. Heister†

School of Aeronautics and Astronautics, Purdue University, W. Lafayette, IN

Abstract

Compound capillary jets are utilized in the manufacturing of coated tablets in the pharmaceutical industry, or to produce well managed ink drops in the printing industry. Differences in densities, surface tensions, and radii between the inner and outer liquids cause complex instability behavior of the compound jet, and present an interesting atomization problem. The present study contributes to previous works on inviscid compound jets by establishing an alternative, simplified approach to the dispersion relation, where the surface disturbances of two liquids are assumed to be in phase and proportional to each other, and the flow is treated as irrotational. The drop sizes are evaluated, treating the compound jet at the breakup as a single jet with radius equal to the radius of the outer liquid, where the breakup is assumed to happen when the most unstable flow disturbance is developed. The density, surface tension, and radius ratios are varied parametrically to assess their influence on the stability and drop sizes formed. Overall, this methodology provides means for quick preliminary analysis of compound jets.

* Corresponding author, Graduate Research Assistant

701 W. Stadium Ave., Armstrong Hall #3130, West Lafayette, IN 47907, USA, mismailo@purdue.edu

† Professor, 701 W. Stadium Ave., West Lafayette, IN 47907, USA

Introduction

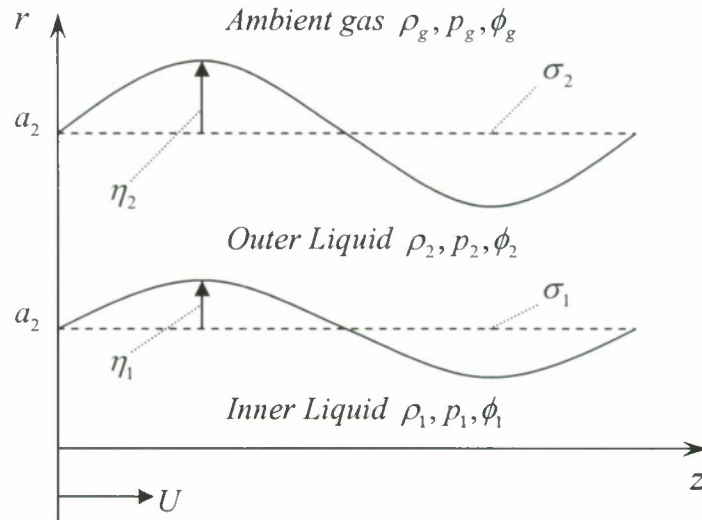


Figure 1. Compound jet schematic

A compound jet schematically shown on Figure 1 is comprised of two liquid jets, where the inner jet indicated by subscript 1 is surrounded by a thin annular outer jet denoted by subscript 2. Each jet has its own density ρ , pressure distribution p , viscosity (not shown), etc. This jet configuration can be achieved, if a high speed liquid is injected through a nozzle into another still or slowly moving liquid. Hertz and Hermanrud [9] (Figures 4 and 5b) observed that due to shear stresses, the inner liquid decelerates and the outer accelerates, and the latter forms a thin annular layer around the inner one. Generally, the compound jet is injected into the ambient quiescent medium having much lower density than both liquids. Two interfaces are developed, the first one being between the inner and the outer liquids, and the second one being between the outer liquid and the ambient gas, with surface tensions σ_1 and σ_2 respectively. Due to natural or artificial flow disturbances, the liquids of the compound jet experience fluctuations η_1 and η_2 around the mean injection radii a_1 and a_2 .

This type of jets is used in printing and pharmaceutical industries. Hertz and Hermanrud [9] and the research group [2] experimentally showed that under certain set of property ratios of two liquids, such as ratios of densities, radii, or interfacial surface tensions, the compound jet can break up into fairly consistent structures, where the clusters of roughly monodisperse inner liquid drops are wrapped by fragments of the outer liquid. In printing, a train of ink drops contained in a long thread of outer liquid (Figure 3 of [2]) is obtained, and electrical field is applied to deflect the drops to the required points on the paper [10]. Similarly, in pharmacy, tablet capsules with an equal number of medicine drops inside them are manufactured (Figure 9 of [2]). The monodispersity of inner drops provides means for the better control of ink drop trajectories or for more precise mass calculation of the active ingredient in the tablet.

Since the liquids have distinct densities, velocities, and surface tensions on both interfaces, the flow disturbances cause the occurrence of capillary jet instability. This problem is similar to the Kelvin-Helmholtz instability [8] but retains its distinct features. Kelvin-Helmholtz instability considers two plain parallel streams moving with two different velocities, infinitely wide in the direction perpendicular to the flow, and sharing one single interface between them. In contrast, the liquids of the compound jet move with equal velocities and have finite dimensions, circular geometry, and one additional interface exists between the outer liquid and the surrounding gas.

There are many publications concerned with the temporal capillary instability of compound jets. Among them, the linear analyses of Sanz and Meseguer [15] and Chaunan and Maldarelli [5] treating the compound jet as inviscid are relevant to this study and are paid closer attention.

Sanz and Meseguer [15] assume that the flow is axisymmetric and purely one-dimensional, where the velocities and pressures depend on the axial coordinate only. Their mass conservation equation is based

on the notion that, if a fluid element is followed as it flows in the lagrangian frame of reference, the Reynolds's transport theorem [7] can be applied to its cross-sectional area chosen as the property that is

conserved, which results in $\frac{\partial r_j^2}{\partial t} + \frac{\partial}{\partial z}(u_j r_j^2) = 0$, named as Cosserat jet equations in [3]. (To make the

comparison of our study to their publication clearer, the original equations used by them will be written in our notation.) Since the flow is considered to be simply axial, their momentum equation is given

by $\frac{\partial u_j}{\partial t} + u_j \frac{\partial u_j}{\partial z} = -\frac{1}{\rho_j} \frac{\partial p_j}{\partial z}$. Furthermore, they consider that the deviations of liquids from their

corresponding mean levels f_1 and f_2 are independent from each other, and the surface radii at each axial location can be calculated as $r_1 = a_1 + \varepsilon f_1$ and $r_2 = a_2 + \varepsilon f_2$, where ε is a small number. By setting the problem in this way, Sanz and Meseguer [15] arrive at a fourth order algebraic equation for the growth rate ω that generates four roots for each value of the wave-number k . Also, they obtain an equation relating f_1 and f_2 to each other and given by amplification factor

$$A = \frac{f_1}{f_2} = \frac{1}{a_1/a_2} \left[1 + \frac{1 - (a_1/a_2)^2}{2\omega^2} (k^4 - k^2) \right] \text{ implying that the disturbances on each interface can be}$$

either in phase, when $A > 1$, which is termed as stretching mode of flow disturbances, or out of phase, when $A < 1$, termed as squeezing mode. These two modes are shown on Figure 2 of [6]. However, Sanz and Meseguer [15] demonstrate that the majority of compound jet disturbances propagate in phase

with $A > 1$. Next, giving the temporal development of the radii of both interfaces by $r_1 = a_1 - \varepsilon f_1 e^{\omega t}$

and $r_2 = a_2 - \varepsilon f_2 e^{\omega t}$ they investigate the cases when one of them vanishes, while the other retains a finite value, or the case when $r_1 = r_2 \neq 0$ which happens once the free surface touches the interface. All three cases are qualitatively shown on Figure 7a-c of [13]. The instance when either of the jets reaches the axis of symmetry is defined as the breakup. From comparing the times of breakup of both jets Sanz and Meseguer [15] draw conclusions about which one of them breaks first.

Chauan and Maldarelli [5] are using momentum and continuity equations that are represented in

the nondimensional form as $\beta_i \frac{D\bar{v}_i}{Dt} = -\nabla P_i$ and $\nabla \cdot \bar{v}_i = 0$, where β_i are the nondimensional density

ratios. This system of equations is then converted into Fourier-Laplace domain to solve for the velocities

and surface deformations, by using the Fourier-Laplace transforms $\hat{f}(k) = \int_{-\infty}^{\infty} f(z) e^{-ikz} dz$

and $\tilde{f}(s) = \int_0^{\infty} f(t) e^{-st} dt$. Then, the pressure is found to be given by $\tilde{P} = A_i I_0(kr) + B_i K_0(kr)$, which

causes the Bessel's functions to emerge in the solution. Next, the solution is inverted back into the time and space domain going through the procedure of converting the Fourier-Laplace line integrals into Bromwich contour integrals. Finally, their dispersion equation is given by $\det(a) = 0$, where a is a size 4 matrix

with elements containing wave-number k , growth rate s , and Bessel's functions. Also, the surface distortions are given as functions of a and initial conditions, which are not proportional to each other.

Similarly to the work by Sanz and Meseguer [15], their dispersion equation generates two pairs of symmetric s roots for each k value, two of which are negative, and the other two positive. The positive roots lead to the occurrence of stretching and squeezing modes shown on Figure 5 of their paper [5].

Chauan and Maldarelli [5] show that the stretching mode is possible for wavelengths greater than the inner jet circumference, whereas the squeezing mode exists for wavelengths greater than the outer jet circumference, while the stretching mode growth rates are larger than the squeezing mode growth rates for all wavelengths. If we consider that the disturbances with larger growth rates prevail, then this is in

agreement with the conclusion of Sanz and Meseguer [15] declaring that most of the compound jets have a stretching mode of motion. Subsequently, they conclude that if the compound jet breaks up similarly to a single jet when the disturbances correspond to k_{\max} and s_{\max} , the stretching mode will make the inner jet break first, thus generating drops of inner liquid inside the outer, followed by the breakup of the outer jet. This reasoning implies that this mode is responsible for the creation of clusters of inner liquid drops in the outer liquid segments as seen in practice and described above.

In contrast to these works, in this study, which is linear as well, we use the potential flow

equations $\nabla^2 \phi_j = 0$ and $\frac{\partial \phi_j}{\partial t} + \int \frac{dp_j}{\rho} + \frac{1}{2} \nabla \phi_j \cdot \nabla \phi_j - G = F(t)$ which allow for radial movement of

liquids [7]. Also, the surface deformations η_1 and η_2 are calculated to be directly proportional to each other, as will be shown below. This means that the disturbances are assumed to be strictly in phase and moving in stretching mode. This is in good agreement with the fact that the compound jets tend to this type of mode, as explained above. Application of the normal mode analysis to these equations yields the solution also involving Bessel's functions as in [5] but does not require the mechanism of forward and backward Fourier-Laplace transforms. The dispersion relation obtained is a second order algebraic equation, producing only two growth rates for each respective disturbance wavelength, where the positive and real one is selected for instability analysis. The jet breakup is considered as a situation when the disturbance with maximum growth rate is applied, following Rayleigh's approach. In this study we are interested in the breakup of the outer liquid only, which characterizes the breakup of the compound jet as a whole. Since the stretching mode is assumed, the outer liquid drops will contain some amount of inner liquid drops. The outer liquid drop sizes are evaluated by assuming that the drop volume is equal to the volume of cylindrical segment having length equal to the wavelength of the most unstable disturbance. Taken all together, this methodology allows making fast preliminary analysis of the compound jet stability behavior. On the other hand, due to the lack of two additional roots, this algorithm lacks the ability to explicitly predict the type of mode of disturbances (stretching or squeezing), or which of the jets will break up first. Next, because of neglected viscosity, the influence of viscosity ratios on stability is not assessed. Lastly, owing to the linear character of this study, the formation of satellite droplets can not be assessed.

Numerous publications on compound jets, such as [13], [16], [6], and [1], take the viscosity of liquids into account and provide detailed investigation of how the variation of density, surface tension, and radius ratios affects the jet instability. To illustrate the diversity of the methods employed to compute the compound jets, some of the flow equations of these authors and the approaches they used to solve them are shown here. Radev and Tchavdarov [13] use the linearized fluid motion equations in the form

$$\frac{\partial \tilde{u}_j}{\partial t} + U \frac{\partial \tilde{u}_j}{\partial z} = -\frac{1}{\rho_j} \nabla \tilde{p}_j + \frac{\mu_j}{\rho_j} \nabla^2 \tilde{u}_j \text{ and } \nabla \cdot \tilde{u}_j = 0, \text{ where } U \text{ is the bulk jet speed and } \mu_j \text{ the}$$

viscosity. Then, applying the boundary conditions they end up with an eigenvalue problem for the Orr-

Sommerfeld equation $i\alpha \text{Re}_1 (1-c)(L-\alpha^2)\phi_j = \frac{\mu_j \rho_1}{\rho_j \mu_1} (L-\alpha^2)^2 \phi_j$ which is solved numerically to

get the dispersion relation. Shkadov and Sisoiev [16] employ Navier-Stokes equations, including gravity, as governing equations for the compound jet flow. They rewrite the linearized governing equations and boundary conditions in terms of the new variables $w_1 = u$, $w_2 = -iv$, $w_3 = \eta p$, and $w_4 = \eta u'$. To get the dispersion relation, the resulting problem is solved numerically by assuming that these variables can be

represented by a series of the form $w_{k(n)}^{(1)} = \sum_{m=0}^{\infty} w_{k(n)(m)}^{(1)} \eta^m$, where $k = 1, \dots, 4$ and $n = 1, 2$. Chanan and

Maldarelli [6] in their paper for viscous compound jets also use Navier-Stokes equations for the flow description, where the velocities are expressed through the stream function as

$$u_i = \frac{1}{r} \frac{\partial \Psi_i}{\partial z} \text{ and } w_i = -\frac{1}{r} \frac{\partial \Psi_i}{\partial r}. \text{ The governing equations and boundary conditions are converted again}$$

into Fourier-Laplace domain to obtain the equation

for $\Psi_i(r) = A_i r I_1(kr) + B_i r K_1(kr) + D_i r I_1(\beta_i r) + E_i r K_1(\beta_i r)$, where k is the wave number and β_i is the term depending on viscosity. The dispersion relation is then represented by an 8 by 8 matrix equation. Afterwards, it is transformed back into time and space domain. Bian and Mashayek [1] developed a one-dimensional nonlinear numerical model for the viscous compound jet simulations, where they are able to accurately track the liquid surface evolution of both jets. The flow equations are solved by utilizing the spectral method. In addition to previous authors, they provide the sizes of main and satellite drops occurring at different property ratios of the two liquids.

Assumptions

In experiment by Hertz and Hermanrud [9], both jets were injected at constant flow rates. Some distance far from the nozzle, the flow became laminar and one-dimensional with a negligible mixing at the interface between two liquids, and the liquids acquired approximately same velocity equal to the bulk velocity of the compound jet denoted here as U . This flow behavior continued until the moment when disturbances grew to large magnitudes. Hence, to model the jet, we can consider infinitely long, immiscible liquid columns of radii a_1 and a_2 , laminar, axial, steady base flow, and choose a frame of reference moving with speed U that is represented by the cylindrical coordinate system having radial and axial coordinates r and z respectively. This allows us to operate with merely perturbed flow velocities and pressures instead of dealing with the total ones in our calculations. Following the reasoning on instability of Drazin and Reid [8] for the Reynolds's experiment on the pipe flow, we can assume that in the experiment by Hertz and Hermanrud [9], the disturbances to both liquids were essentially caused by imperfections of the nozzle wall or by small flow rate fluctuations, which permits us to assume that the magnitudes of velocity or liquid surface disturbances are small. Historically, beginning with Rayleigh [14], they were treated as sinusoidal, which is also the case for this study. For the case of a single jet, Rayleigh [14] concluded that the most unstable disturbances are axisymmetric. Thinking of each interface of the compound jet as a free surface of a single jet of corresponding size, we will similarly consider that the disturbances and the resulting flow are axisymmetric and the flow parameters may depend on r , z and time t . Chandrasekhar [4] (Figure 129) showed that for single jets, compared to the inviscid flow case, the presence of viscosity decreases the growth rates and most unstable wave numbers of disturbances, but the qualitative dependence of them from each other does not change. Taking this into account, we limit the scope of this study to an inviscid case. Lighthill [12] shows that in the system with only small disturbances to the flow field, the vorticity does not change with time. Then, since we initially postulate inviscid flow, we can assume that the flow remains irrotational for all time and introduce the velocity potentials ϕ_1 and ϕ_2 [7]. In the experiments by Hertz and Hermanrud [9] the flow remained laminar in the range of compound jet speeds U from 5 to 40 m/s, which are high enough to neglect forces associated with gravity, though not sufficient to cause large aerodynamic drag. For the sake of simplicity, the ambient medium is treated as quiescent vacuum gas with zero density ρ_g . Hence, we can neglect any other body forces, except equilibrium forces due to inertia and pressure gradients. Since the flow disturbances are small, the capillary speeds of disturbances are lower than the compound jet velocity. As Keller, Rubinow, and Tu [11] have shown, this fact along with the choice of the frame reference described above allows us to limit the instability analysis in this study to the temporal case. Observing that U were much smaller than speed of sound and supposing that the liquids of the compound jet retained constant densities in the basic flow, we can consider incompressible flow overall. Rayleigh [14] has shown that the disturbance with maximum growth rate dominates over others. Thus, we can assume that the jet breaks up into liquid segments only when such most unstable disturbance has developed and the jet oscillates with the frequency equal to the frequency of this disturbance.

Governing equations

Consider an axial location where small, in phase surface disturbances are introduced, Figure 1. This causes the inner interface to be raised to the new level η_1 above a_1 and the outer free surface to be

raised to the new level η_2 above a_2 . Then, the cross-sectional area of the inner jet is changed

by $dA_1 = \pi \left((a_1 + \eta_1)^2 - a_1^2 \right)$ which is approximately equal to

$$dA_1 \cong 2\pi a_1 \eta_1 \quad (1.1)$$

The area change of the outer jet is $dA_2 = \pi \left((a_2 + \eta_2)^2 - a_2^2 \right) - \pi \left((a_1 + \eta_1)^2 - a_1^2 \right)$. It is counted from η_1 since the inner interface is already deflected, and can be approximated by

$$dA_2 \cong 2\pi (a_2 \eta_2 - a_1 \eta_1) \quad (1.2)$$

Since the surface deformations are assumed to be small, then we can assume that

$$dA_1 = dA_2 \quad (1.3)$$

After combining equations(1.1), (1.2) and (1.3), we get a relation between surface elevations of the upper and inner liquid

$$\eta_2 = 2 \frac{a_1}{a_2} \eta_1 \quad (1.4)$$

This shows that the surface elevations η_1 and η_2 are proportional to each other, which allows to assume stretching mode of the disturbance propagation.

Consider the fluid motion along the inner interface and the outer free surface where the points have radial coordinates $r = a_i + \eta_i$, where $i = 1, 2$ are the indices denoting each interface. Conservation of mass equations for the perturbed incompressible, axisymmetric flow in the cylindrical coordinate system moving

with bulk compound jet speed are given by $\frac{\partial u_j}{\partial z} + \frac{1}{r} \frac{\partial}{\partial r} (r v_j) = 0$, where $j = 1, 2$ are the indices

denoting each liquid. Assuming irrotational flow and introducing the disturbance velocity potentials for two

liquids by $u_j = \frac{\partial \phi_j}{\partial z}$ and $v_j = \frac{\partial \phi_j}{\partial r}$ [7], we can rewrite these equations as

$$\frac{\partial^2 \phi_j}{\partial z^2} + \frac{1}{r} \frac{\partial \phi_j}{\partial r} + \frac{\partial^2 \phi_j}{\partial r^2} = 0 \quad (1.5)$$

We can use the unsteady Bernoulli equation $\frac{\partial \phi}{\partial t} + \int \frac{d\hat{p}}{\rho} + \frac{1}{2} \nabla \phi \cdot \nabla \phi - G = F(t)$ to describe the

irrotational motion of a fluid particle along the streamlines [7], in this case the inner interface and the outer free surface. If we neglect the body forces G and absorb the time constant $F(t)$ into ϕ , this equation provides the dynamic boundary conditions for both interfaces

$$\frac{\partial \phi_j}{\partial t} + \int \frac{d\hat{p}_j}{\rho_j} + \frac{1}{2} \nabla \phi_j \cdot \nabla \phi_j = 0 \quad (1.6)$$

where the pressure integrals represent the change between current and initial pressures $\int d\hat{p}_j = p_j - P_j$.

When the flow is undisturbed, the surface curvatures are equal to the initial jet radii. Thus, the initial and current interfacial pressure jumps can be written as follows:

$$\text{Inner interface} \quad P_1 - P_2 = \frac{\sigma_1}{a_1} \quad p_1 - p_2 = \sigma_1 K_1 \quad (1.7)$$

$$\text{Free surface} \quad P_2 - P_g = \frac{\sigma_2}{a_2} \quad p_2 - p_g = \sigma_2 K_2 \quad (1.8)$$

The corresponding axisymmetric surface curvatures [17] can be found as

$$K_i = \frac{1}{(a_i + \eta_i) \left[1 + \left(\frac{\partial(a_i + \eta_i)}{\partial z} \right)^2 \right]^{1/2}} - \frac{\frac{\partial^2(a_i + \eta_i)}{\partial z^2}}{\left[1 + \left(\frac{\partial(a_i + \eta_i)}{\partial z} \right)^2 \right]^{3/2}} \quad (1.9)$$

The condition that a fluid particle at the interface will remain on interface for all time serves as kinematic boundary condition [7]. In axisymmetric case, for two liquids we have

$$\frac{\partial \phi_j}{\partial r} = \frac{\partial \eta_i}{\partial t} + \frac{\partial \phi_j}{\partial z} \frac{\partial \eta_i}{\partial z} \quad (1.10)$$

The system of equations(1.5)-(1.10) poses a nonlinear problem that is hard to solve. However, since the surface disturbances η_i are small, the amplitude of motion and surface slopes $\frac{\partial \eta_i}{\partial z}$ are small as well. Assuming that the disturbance frequencies are not high, we can suppose that the velocity disturbances $u_j = \frac{\partial \phi_j}{\partial z}$ and $v_j = \frac{\partial \phi_j}{\partial r}$ are small as well. Hence, this problem can be solved by linearization around points with radial coordinates $r = a_i$. In this case, the derivatives in equations(1.5)-(1.10) can be expanded in Taylor series around points $r = a_i$, and only the first order terms can be retained since all other terms are products of higher order derivatives with small quantities η_i ,

$$\begin{aligned} \frac{\partial \phi_j}{\partial \beta}(z, a_i + \eta_i, t) &= \frac{\partial \phi_j}{\partial \beta}(z, a_i, t) + \eta_i \frac{\partial^2 \phi_j}{\partial \beta^2}(z, a_i, t) + \dots \cong \frac{\partial \phi_j}{\partial \beta}(z, a_i, t) \\ \frac{\partial^2 \phi_j}{\partial \beta^2}(z, a_i + \eta_i, t) &= \frac{\partial^2 \phi_j}{\partial \beta^2}(z, a_i, t) + \eta_i \frac{\partial^3 \phi_j}{\partial \beta^3}(z, a_i, t) + \dots \cong \frac{\partial^2 \phi_j}{\partial \beta^2}(z, a_i, t) \end{aligned}$$

where β can be r or z [7]. Then, the linearized continuity equations at $r = a_i$ are given by

$$\frac{\partial^2 \phi_j}{\partial z^2} + \frac{1}{r} \frac{\partial \phi_j}{\partial r} + \frac{\partial^2 \phi_j}{\partial r^2} = 0 \quad (1.11)$$

Neglecting $\nabla \phi_j \square \nabla \phi_j$ in (1.6) as a sum of squares of small quantities of the form $\left(\frac{\partial \phi_j}{\partial \beta} \right)^2$, the dynamic boundary conditions can be rewritten as

$$\rho_j \frac{\partial \phi_j}{\partial t} = P_j - p_j$$

At the inner interface and the outer free surface the subtraction of these equations gives

$$\text{At } r = a_1 + \eta_1 \quad \rho_1 \frac{\partial \phi_1}{\partial t} - \rho_2 \frac{\partial \phi_2}{\partial t} = (P_1 - P_2) - (p_1 - p_2) \quad (1.12)$$

$$\text{At } r = a_2 + \eta_2 \quad \rho_2 \frac{\partial \phi_2}{\partial t} - \rho_g \frac{\partial \phi_g}{\partial t} = (P_2 - P_g) - (p_2 - p_g) \quad (1.13)$$

In the expression for curvatures (1.9) we can assume that $1 \square \left(\frac{\partial \eta_i}{\partial z} \right)^2$, and keeping terms up to first order

terms in the binomial expansion $\frac{1}{(a_i + \eta_i)} = \frac{1}{a_i} - \frac{\eta_i}{a_i^2} + \dots$, we can simplify them to

$$K_i = \frac{1}{a_i} - \frac{\eta_i}{a_i^2} - \frac{\partial^2 \eta_i}{\partial z^2} \quad (1.14)$$

Next, plugging (1.7), (1.8) into (1.12), (1.13) respectively, using (1.14), and assuming quiescent vacuum gas for the ambient with $\phi_g = 0, \rho_g = 0$, we arrive at the linearized dynamic boundary conditions for the inner interface and the outer free surface written respectively as follows:

$$\text{At } r = a_1 \quad \rho_1 \frac{\partial \phi_1}{\partial t} - \rho_2 \frac{\partial \phi_2}{\partial t} = \sigma_1 \left(\frac{\eta_1}{a_1^2} + \frac{\partial^2 \eta_1}{\partial z^2} \right) \quad (1.15)$$

$$\text{At } r = a_2 \quad \rho_2 \frac{\partial \phi_2}{\partial t} = \sigma_2 \left(\frac{\eta_2}{a_2^2} + \frac{\partial^2 \eta_2}{\partial z^2} \right) \quad (1.16)$$

Neglecting $\frac{\partial \phi_j}{\partial z} \frac{\partial \eta_i}{\partial z}$ terms in (1.10) as products of small quantities gives the linearized kinematic boundary conditions

$$\text{At } r = a_1 \quad \frac{\partial \phi_1}{\partial r} = \frac{\partial \phi_2}{\partial r} = \frac{\partial \eta_1}{\partial t} \quad (1.17)$$

These conditions also reflect the fact that the vertical velocity components of two liquids meeting at the boundary should be equal.

This study assumes flow disturbances have sinusoidal shape and grow only temporally [11].

Because of that, they can be represented as Fourier waves $\phi_j = F_j(r) \exp(\omega t + ikz)$ in order to solve the system of equations(1.11), (1.15)-(1.17). Plugging them into continuity equation (1.11) results in Bessel's equation for the unknown function of the radius $F_j(r)$

$$r^2 \frac{\partial^2 F_j(r)}{\partial r^2} + r \frac{\partial F_j(r)}{\partial r} - k^2 r^2 F_j(r) = 0$$

For each liquid this equation gives a solution in terms of Bessel's functions

$F_j(r) = C_1^{(j)} I_0(kr) + C_2^{(j)} K_0(kr)$, where $C_1^{(j)}$ and $C_2^{(j)}$ are unknown constants to be defined for each liquid. Disturbances should vanish at the jet axis, therefore $C_2^{(1)}$ must be zero since $\lim_{r \rightarrow 0} K_0(kr) = \infty$.

After that, the velocity potentials can be rewritten as

$$\text{For } 0 < r < a_1 \quad \phi_1 = C_1^{(1)} I_0(kr) \exp(\omega t + ikz) \quad (1.18)$$

$$\text{For } a_1 < r < a_2 \quad \phi_2 = \left(C_1^{(2)} I_0(kr) + C_2^{(2)} K_0(kr) \right) \exp(\omega t + ikz) \quad (1.19)$$

Similarly, due to sinusoidal shape and relation(1.4), the surface deformations are given by

$$\text{At } r = a_1 \quad \eta_1 = \eta_0 \exp(\omega t + ikz) \quad (1.20)$$

$$\text{At } r = a_2 \quad \eta_2 = 2 \frac{a_1}{a_2} \eta_0 \exp(\omega t + ikz) \quad (1.21)$$

Substituting the velocity potential ϕ_1 (1.18) and surface deformation η_1 (1.20) into the first kinematic boundary condition at $r = a_1$ (1.17) we get

$$C_1^{(1)} = \frac{\eta_0 \omega}{k} \frac{1}{I_1(ka_1)} \quad (1.22)$$

Plugging the velocity potential ϕ_2 (1.19) and surface deformation η_1 (1.20) into the second kinematic boundary condition at $r = a_1$ (1.17) results in

$$C_1^{(2)} = \frac{\eta_0 \omega + C_2^{(2)} K_1(ka_1)}{I_1(ka_1)} \quad (1.23)$$

Inserting the velocity potential ϕ_2 (1.19) and surface deformation η_2 (1.21) into the dynamic boundary condition at $r = a_2$ (1.16) and using the recently obtained expression for $C_1^{(2)}$ yields

$$C_2^{(2)} = \frac{2 \frac{a_1}{a_2} \frac{\eta_0 \sigma_2}{\rho_2 \omega} \left(\frac{1}{a_2^2} - k^2 \right) - \frac{\eta_0 \omega}{k} \frac{I_0(ka_2)}{I_1(ka_1)}}{K_1(ka_1) \frac{I_0(ka_2)}{I_1(ka_1)} + K_0(ka_2)} \quad (1.24)$$

Finally, after inserting both velocity potentials ϕ_1 (1.18), ϕ_2 (1.19) and surface deformation η_1 (1.20) into the dynamic boundary condition at $r = a_1$ (1.15), we obtain the intermediate expression relating all parameters of the problem

$$\rho_1 \omega \left[C_1^{(1)} I_0(ka_1) \right] - \rho_2 \omega \left[C_1^{(2)} I_0(ka_1) + C_2^{(2)} K_0(ka_1) \right] = \sigma_1 \left[\frac{\eta_0}{a_1^2} + (ik)^2 \eta_0 \right]$$

Dispersion equation and drop size evaluation

Substituting of constants $C_1^{(1)}$, $C_1^{(2)}$ and $C_2^{(2)}$ defined by equations (1.22)-(1.24) into the last expression and rearranging results in the dispersion equation of the form

$$\omega^2 = k \frac{-2 \frac{a_1}{a_2} \sigma_2 \left(\frac{1}{a_2^2} - k^2 \right) \frac{E}{D} - \sigma_1 \left(\frac{1}{a_1^2} - k^2 \right)}{\rho_2 \left(A - B \frac{E}{D} \right) - \rho_1 A} \quad (2.1)$$

where the functions A, B, D, E are defined as follows:

$$A = \frac{I_0(ka_1)}{I_1(ka_1)} \quad B = \frac{I_0(ka_2)}{I_1(ka_1)}$$

$$D = K_1(ka_1) \frac{I_0(ka_2)}{I_1(ka_1)} + K_0(ka_2) \quad E = K_1(ka_1) \frac{I_0(ka_1)}{I_1(ka_1)} + K_0(ka_1)$$

Dispersion relation given by (2.1) provides two symmetric real roots when both numerator and denominator are simultaneously positive or negative. The positive root represents the growth rate ω that makes the disturbance grow in time as it moves with the bulk jet velocity U . In case when numerator and denominator have opposite signs the roots are complex and conjugate to each other, the disturbances are sinusoidal and stable, and do not grow in time. Because there are only two roots, this dispersion relation reflects the stability behavior of the compound jet as if it was one single jet with sizes equal to those of the outer jet. It can not provide information on the stability of inner and outer jets taken separately from each other as in [5] and [15].

Let us investigate the situation when the outer liquid is removed and the compound jet reduces to a single jet. The absence of the outer liquid implies that $\rho_2 = 0, \sigma_2 = 0, a_2 = a_1$. This causes the functions

A, B, D, E to simplify to $A = B = \frac{E}{D} = 1$. Consequently, the dispersion equation becomes

$$\omega^2 = k \frac{-\sigma_1 \left(\frac{1}{a_1^2} - k^2 \right)}{-\rho_1 A} = \frac{\sigma_1}{\rho_1 a_1^3} (1 - k^2 a_1^2) k a_1 \frac{I_1(k a_1)}{I_0(k a_1)}$$

which is Rayleigh's equation for a single jet of radius a_1 [14].

The dependence of positive growth rates from wave numbers does have a maximum at which the most unstable disturbance occurs. As was shown by Sanz and Meseguer [15] and Chaunan and Maldarelli [5], the assumption of stretching mode of disturbances implies that the inner jet always breaks up first followed by the breakup of the outer jet, which means that in this study the point $(k_{\max}, \omega_{\max})$ corresponds to the breakup of the outer jet already containing the drops of inner liquid. Following Rayleigh's approach, we assume that the drops are formed at the crests of disturbance waves, moving with the period equal to the wavelength $\lambda_{\max} = \frac{2\pi}{k_{\max}}$. Since the liquids of the compound jet are incompressible and disturbance waves develop from the initially undisturbed flow, the volume of the jet between crests is equal to the volume of undisturbed cylindrical jet segment having radius a_2 and length λ_{\max} . Assuming the liquid between crests is spent entirely to form a drop, because this model cannot account for the formation of smaller satellite drops, and that due to the surface tension on the free surface σ_2 it will attain a spherical shape, we

have $\pi a_2^2 \lambda_{\max} = \frac{4}{3} \pi r_d^3$ which gives

$$r_d = \left(\frac{6 \pi a_2^2}{4 k_{\max}} \right)^{\frac{1}{3}} \quad (2.2)$$

Nondimensionalization of equations (2.1) and (2.2) can be made by choosing a_2 as length scale and $\left(\frac{\rho_2 a_2^3}{\sigma_2} \right)^{\frac{1}{2}}$ as time scale. The relation of dimensional wave numbers and growth rates to their

nondimensional values denoted by star is given by $k = \frac{k^*}{a_2}$ and $\omega = \omega^* \left(\frac{\rho_2 a_2^3}{\sigma_2} \right)^{-\frac{1}{2}}$ respectively. Let radius, surface tension, and density ratios be defined as

$$\alpha = \frac{a_2}{a_1} \quad s = \frac{\sigma_2}{\sigma_1} \quad d = \frac{\rho_2}{\rho_1}$$

Following that, the nondimensional form of the dispersion equation is given by

$$(\omega^*)^2 = k^* \frac{-\frac{2}{\alpha} [1 - (k^*)^2] \frac{E}{D} - \frac{1}{s} [\alpha^2 - (k^*)^2]}{A - B \frac{E}{D} - \frac{A}{d}} \quad (2.3)$$

where the functions A, B, D, E are rewritten in the following form:

$$A = \frac{I_0(k^*/\alpha)}{I_1(k^*/\alpha)} \quad B = \frac{I_0(k^*)}{I_1(k^*/\alpha)}$$

$$D = K_1 \left(k^* / \alpha \right) \frac{I_0(k^*)}{I_1(k^*)} + K_0(k^*) \quad E = K_1 \left(k^* / \alpha \right) \frac{I_0(k^* / \alpha)}{I_1(k^* / \alpha)} + K_0(k^* / \alpha)$$

Likewise, given that $r_d = r_d^* a_2$ and $k = \frac{k_{\max}^*}{a_2}$, we can rewrite equation (2.2) as

$$r_d^* = \left(\frac{6 \pi}{4 k_{\max}^*} \right)^{1/3} \quad (2.4)$$

Further in this study, the nondimensional quantities will be written without superscript *.

Parametric study and comparison of results

In this section the influence of radius α , density d , and surface tension s ratios on the jet stability and on the drop sizes formed is investigated.

Figures 2 and 3 show how the surface tension and radius ratios affect the jet stability and are compared to analogous Figures 8 and 10 of [5], showing same results plotted for the stretching mode of disturbances. The nondimensionalization scales used by Chaunan and Maldarelli [5] were a_1 for length and

$\left(\frac{\rho_1 a_1^3}{\sigma_1} \right)^{1/2}$ for time, while the radius, surface tension, and density ratios were defined in the same way as

α, s, d respectively. Let the growth rates and wave numbers nondimensionalized by their scaling factors be denoted by superscript C . Then, they are related to the same quantities in this study by

$\omega_C^* = \omega^* \left(\frac{d \alpha^3}{s} \right)^{-1/2}$ and $k_C^* = k^* \frac{1}{\alpha}$. Figures 2 and 3 are plotted with ω_C^* on the vertical axis and k_C^* on

the horizontal without showing superscript *.

Figure 2 shows that, as the surface tension of the outer liquid increases, there is a general trend towards the lower most unstable wave numbers, or lower frequencies of the disturbances. Also, the range of unstable wavelengths becomes shorter. These tendencies can be explained by the fact that at higher frequencies the surface gets more deformed, thus causing higher curvatures and the resulting surface tension to act stronger and damp these high frequency oscillations.

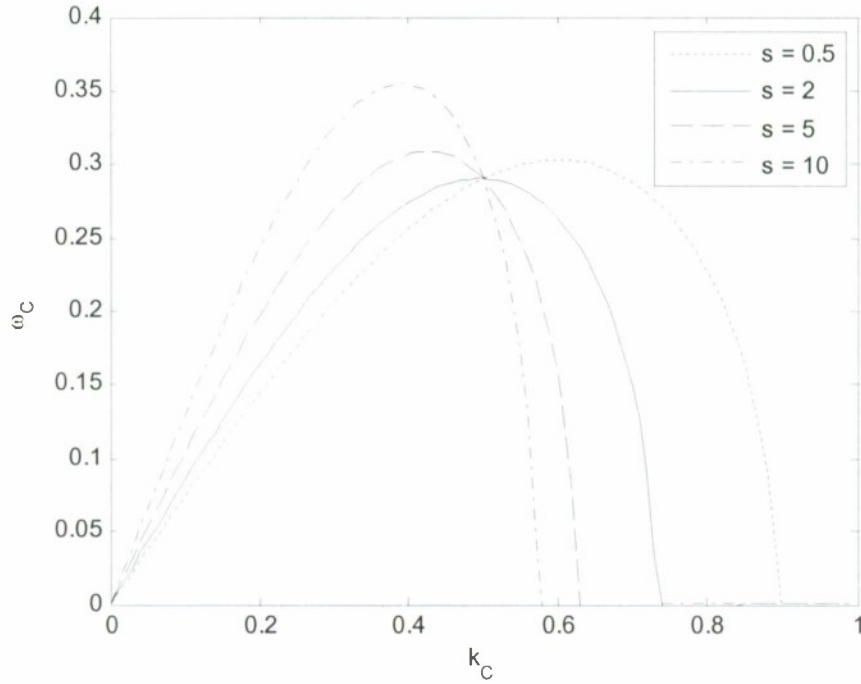


Figure 2 Effect of surface tension ratio on stability variation with $d = 1$, $\alpha = 2$.
(Compare to Figure 8 of [5])

For the growth rate we can observe three types of behavior. The peak of the growth rates first decreases when s takes values from less than 1 up to 1.6 (some curves are not shown here), then stays approximately at the level equal to the peak of $s = 2$ curve, and finally increases for values $s > 2$. This can be viewed in the following way. Since s is the ratio of surface tensions, then by fixing σ_1 we increase σ_2 as s gets larger. Next, we can represent the disturbances in the form $\phi_j = \hat{\phi}_j \exp(\omega t + ikz)$ and $\eta_j = \hat{\eta}_j \exp(\omega t + ikz)$, where $\hat{\phi}_j$ depend on k and ω through equations (1.22)-(1.24), and we assume that $\hat{\eta}_j$ are fixed. Inserting them into the boundary conditions (1.15) and (1.16) we obtain

$$\text{At } r = a_1 \quad \omega \left(\rho_1 \hat{\phi}_1 - \rho_2 \hat{\phi}_2 \right) = \sigma_1 \hat{\eta}_1 \left(\frac{1}{a_1^2} - k^2 \right) \quad (2.5)$$

$$\text{At } r = a_2 \quad \omega \rho_2 \hat{\phi}_2 = \sigma_2 \hat{\eta}_2 \left(\frac{1}{a_2^2} - k^2 \right) \quad (2.6)$$

Here the term $\rho_j \hat{\phi}_j$ implicitly characterizes the momentum of the liquid. In all three cases considered, k_{\max} decreases while σ_2 increases. The first and second cases, where ω_{\max} decreases and then stays nearly constant, are possible when $\rho_2 \hat{\phi}_2$ grows, and $\rho_1 \hat{\phi}_1$ grows faster than $\rho_2 \hat{\phi}_2$. The last case, where k decreases and ω_{\max} rises, is achievable when $\rho_2 \hat{\phi}_2$ does not change much, and $\rho_1 \hat{\phi}_1$ grows. This means that, when both liquids have growing momentums, there is a net decrease of the most unstable growth rates, whereas, in the situation when only the inner liquid gains momentum, there is a net increase of the maximum growth rates.

Comparing Figure 2 to Figure 8 of [5], we can see that their curves with $s = 0.5, 2$ have one maximum growth rate, while the ones with $s = 5, 10$ have two maximum growth rates. However, the peak

values are similar on both figures. On their figure, when s is increased from 0.5 to 2, the maximum growth rate decreases slightly without noticeable change in the most unstable wave numbers, and, when s is increased from 5 to 10, the maximum on the right shifts toward lower growth rates and higher wave numbers, whereas, the maximum on the left shifts towards higher growth rates and lower wave numbers. Conclusively, except for the maximums on the right of the curves with $s = 5, 10$, their curves have similar trends.

Next, we consider the effect of the radius ratio variation on the jet stability (Figure 3). We can observe that at values of α from 10 to approximately 4.5 (the curves with values of α different from shown on Figure 3 are not illustrated) the peak of the growth rate decreases and shifts to lower wave numbers. Then, from $\alpha \approx 4.5$ to $\alpha \approx 2.5$ the shifting to the left continues with the value of maximum staying at about 0.25. Finally, the peak starts to grow with moving towards higher wave numbers. Correspondingly, the range of unstable wave numbers first shortens, then widens.

The observed phenomena can be interpreted as follows. When the radius ratio is high, the volume of the outer jet is much bigger, and its inertia dominates over the surface tension forces on both interfaces, which leads to high growth rates and wide range of unstable wave numbers. The decrease of its radius to $\alpha = 4..2.5$ results in less volume and higher lateral curvatures, so that the surface tension on both interfaces starts to compete with inertia and decreases the growth rates and the wave number ranges. In contrast, when the growth rates start to grow at $\alpha < 2.5$, the inertia of the inner jet starts to be the prevailing factor. After that, the thinner the layer of the outer liquid becomes, the less resistance it poses for the inner jet to grow. Accordingly, the range of unstable frequencies also expands. Comparing Figure 3 to Figure 10 of [5], we can conclude that the growth rates behave in the same way, have similar peak values, but the range of unstable wave numbers on their figure does not change.

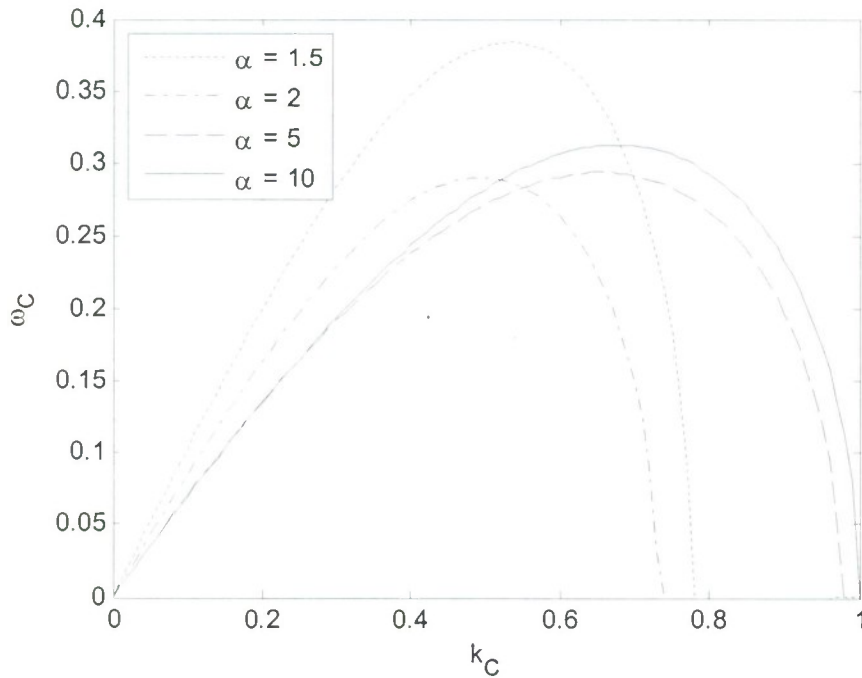


Figure 3 Effect of radius ratio on stability variation with $d = 1, s = 2$.
(Compare to Figure 10 of [5])

In order to evaluate the case when the density ratio is varied, we compare the results on Figure 4 of this study to those on Figures 3 a, b, c of [15]. These figures show the distribution of the maximum growth rates for three different density ratios $d = 0.5, 1.0, 2.0$ respectively, where the surface tension ratio is fixed and the radius ratio changes, or vice versa. Sanz and Meseguer [15] use the same length and time scales, so the comparison can be made without converting the growth rates and wave numbers.

However, their ratio parameters are inverses of s, d, α . Hence, we can choose one point ($\sigma = 0.7, R = 0.7$) on all of their three plots, equal to ($s = 1.4, \alpha = 1.4$) in our system, and compare the maximum growth rates and wave numbers at this point to those calculated in this study (Table 1). This table shows good agreement between the maximum growth rates and growing discrepancy between the most unstable wave numbers for increasing density ratios.

	Fig 4		Figs.3a,b,c of [15]	
	$1/k_{\max}$	ω_{\max}	$1/k_{\max}$	ω_{\max}
$d = 0.5$	1.23	0.39	1.25	0.40
$d = 1$	1.25	0.55	1.20	0.55
$d = 2$	1.27	0.76	1.17	0.75

Figure 4 shows increasing growth rates, as the density of the outer liquid increases when the inner liquid density is fixed, while the most unstable wave numbers move slightly to the left. In reality, the jet should be more stable, if the outer liquid becomes denser and heavier, since the flow disturbances have to move more mass. However, in this study, the time scale itself depends on the density ratio, and the relation

between the dimensional and nondimensional growth rates can be rewritten as $\omega = \omega^* \left(\frac{d\rho_1 a_2^3}{\sigma_2} \right)^{-1/2}$,

where the factor $\left(\frac{d\rho_1 a_2^3}{\sigma_2} \right)^{1/2}$ grows faster than ω^* . Thus, to examine the expected behavior, we can

choose, for example, $\rho_1 = 1000 \frac{kg}{m^3}$, $\sigma_1 = 0.074 \frac{N}{m}$, and $a_1 = 0.005m$ and plot the dimensional growth rates and wave numbers (index *dim*) for the same s, α, d (Figure 5). On both figures (4 and 5) we can see that the range of unstable wave numbers almost does not change, which follows because there are no changes in radii or surface tensions leading to the damping of high frequencies.

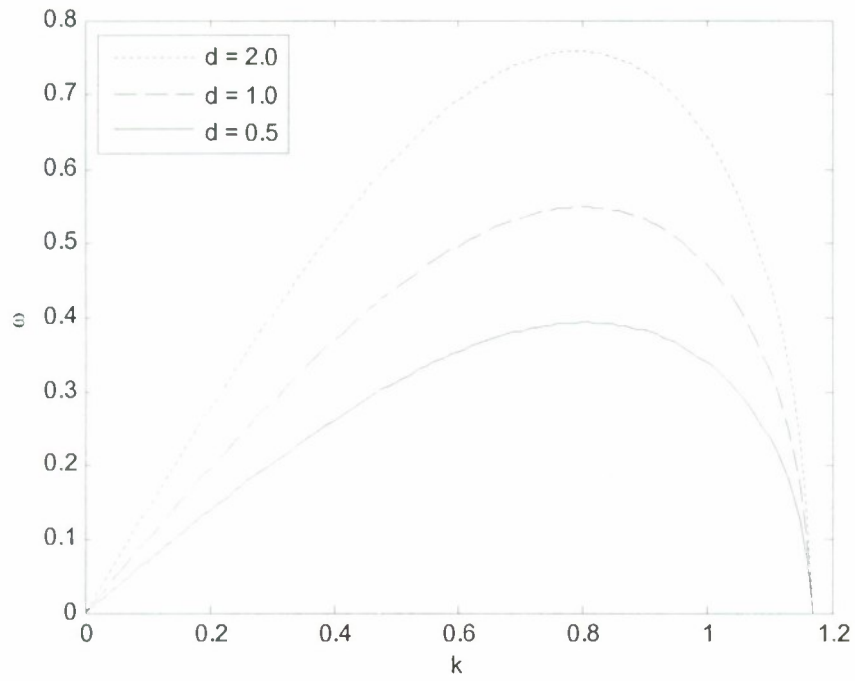


Figure 4 Effect of density ratio on stability variation with $s = 1.4, \alpha = 1.4$.
 (Compare to Figure 3a of [15])

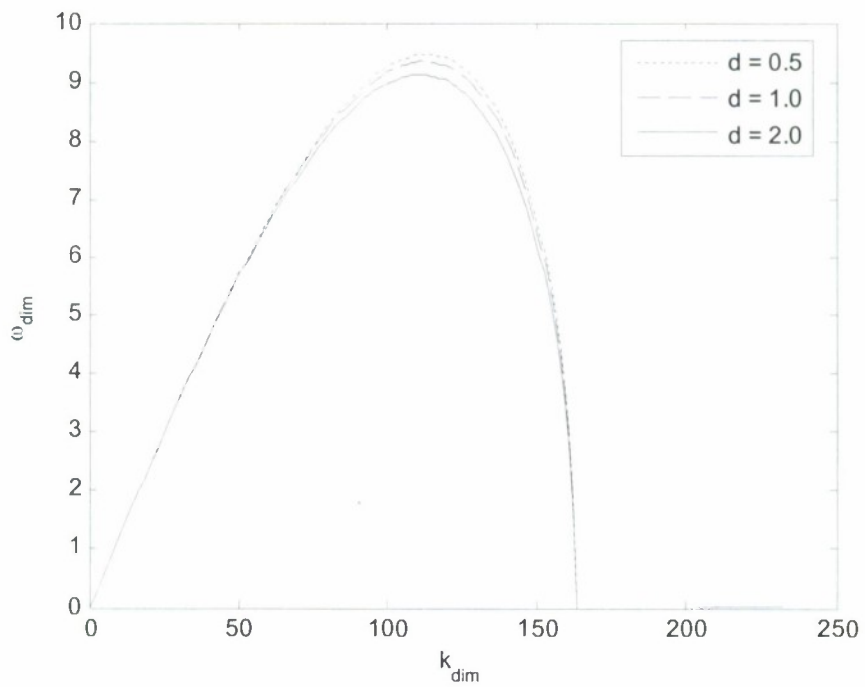


Figure 5 Dimensional growth rates and wave numbers at varying density with $s = 1.4, \alpha = 1.4$.

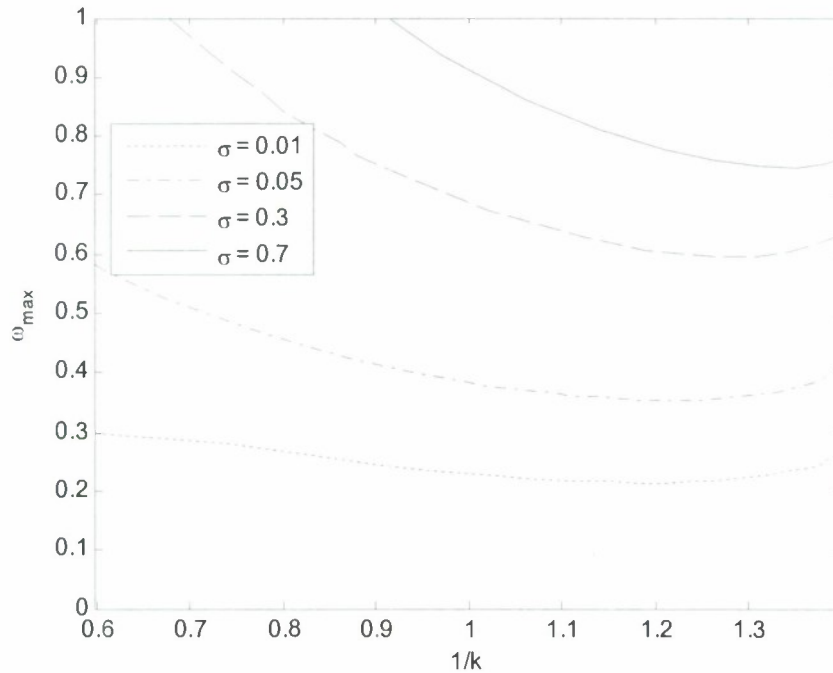


Figure 6 Maximum growth rates at varying surface tension and radius ratios for $\alpha = 1..10$.
(Compare to Figure 3a of [15])

Analogous to Figure 3a of [15], we may plot a conclusive chart (Figure 6) containing the graphs of the maximum growth rates at different surface tension ratios given by $\sigma = \frac{\sigma_1}{\sigma_2} = \frac{1}{s}$, while each of them is calculated for the given range of radius ratios. After comparing these figures, we can see that the curves on Figure 6 with $\sigma = 0.7$ and $\sigma = 0.3$ have minima, while their curves with same σ values do not. Their $\sigma = 0.3$ curve lies lower and intersects the left axis at about 0.95. Next, their curves with $\sigma = 0.05$ and $\sigma = 0.01$ start with lower values on the left axis and terminate on the curve ABC indicating the region where no solution exists. On contrary, these last curves on our plot do continue until intersection with the right axis.

Overall, the differences in results of this study when comparing to the works by Sanz and Meseguer or Chaunan and Maldarelli can be essentially attributed to the differences in dispersion relations and the roots that are generated from them.

Next, we consider the influence of property ratios on the drop sizes based on (2.4) and compare the results to those on Figures 3 c, d, and e of [1]. Their nondimensional length and time scales and property ratios of the liquids are defined in the same way as in this study.

On Figure 7, we can see that the drop radius increases slightly when the density ratio grows, regardless of the surface tension ratio, which is due to the effects shown on Figures 2 and 4. At $d = 1$ and $\alpha = 2$ Figure 3c of [1] gives drop sizes ranging from 1.25 to 2.0. It is not a single number but a distribution of sizes because each wave number produces drops of certain size due to their nonlinear model. The lines for different values of s are almost coincident on their plot. On the contrary, in this study, we consider that drops are created only at the most unstable wave numbers. Thus, we can compare the drop sizes at the wave numbers equal to the most unstable ones and at $d = 1$ (Table 2). While their drop sizes are slightly smaller, there is acceptable agreement between them.

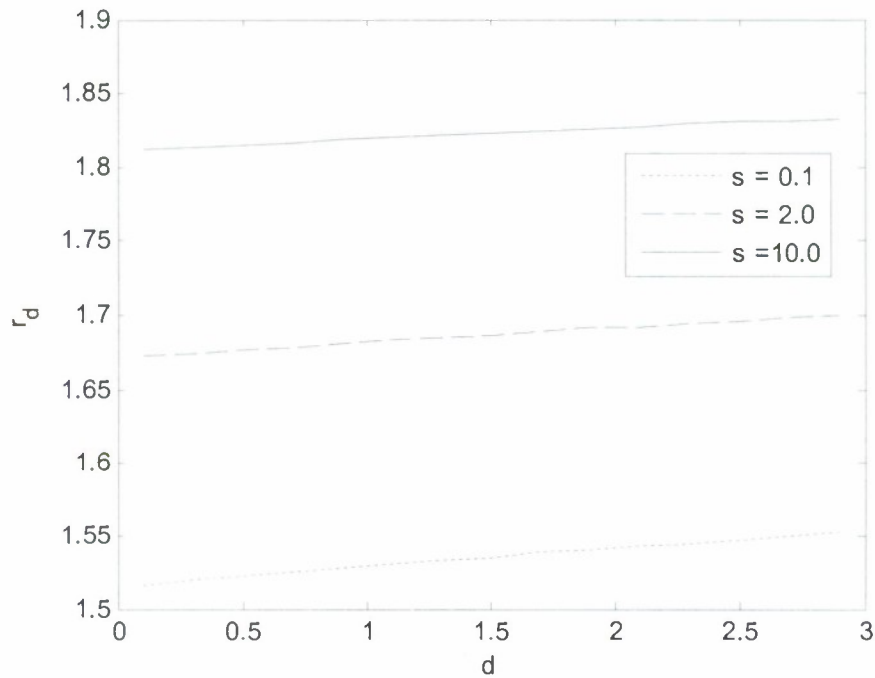


Figure 7 Effect of density ratio on drop sizes at fixed surface tension ratios with $\alpha = 2$.
(Compare to Figure 3c of [1])

	k_{\max}/α	r_d (Fig.7)	r_d (Fig.3c [1])
$s = 0.1$	0.66	1.52	≈ 1.4
$s = 2.0$	0.50	1.67	≈ 1.5
$s = 10.0$	0.39	1.82	≈ 1.7

As the surface tension ratio grows (Figure 8), we can observe a gradual increase in drop sizes at all density ratios. Similarly, calculating the most unstable wave numbers and drop sizes at $s = 2$, we can compare this figure to Figure 3d (Table 3). Again, their curves for different d values almost overlap. Table 3 shows that their drop sizes are smaller like in Table 2. This may be attributed to the fact that some of the liquid volume is spent on forming the satellite droplets, which can not be addressed in this study.

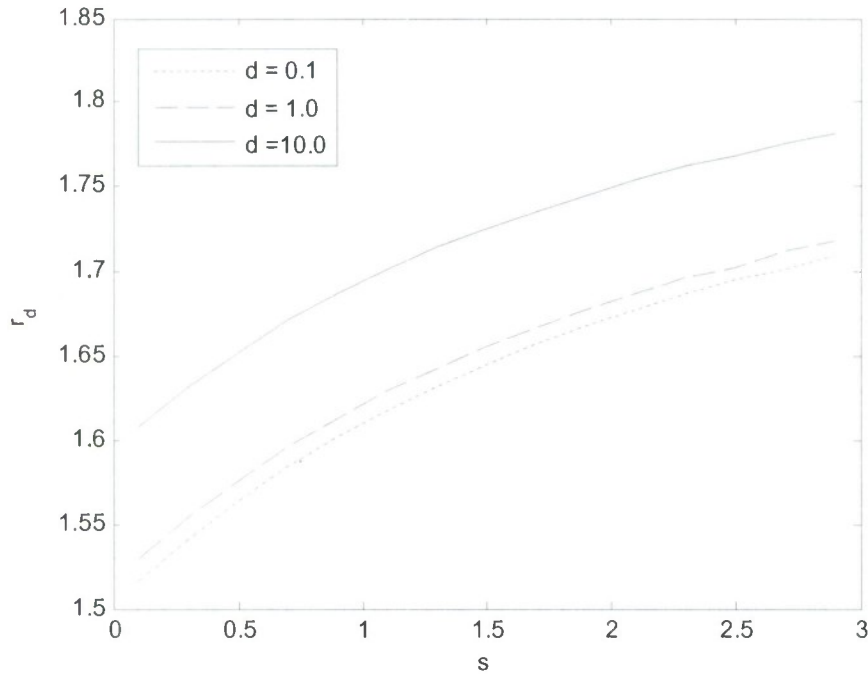


Figure 8 Effect of surface tension ratio on drop sizes at fixed density ratios with $\alpha = 2$.

	k_{\max}/α	r_d (Fig.8)	r_d (Fig.3d [1])
$d = 0.1$	0.50	1.67	≈ 1.5
$d = 1.0$	0.50	1.68	≈ 1.5
$d = 10.0$	0.44	1.75	≈ 1.6

On Figure 9, we can see that for small size ratios $\alpha = 1.5, 2.0$ the drop sizes vary appreciably, but as the size ratio becomes high they change a little. This means that the effect of larger thickness of the outer liquid dominates over changes in the surface tension. Accordingly, this behavior can be used in cases when the liquids are varied, but the desired size is expected to be almost same. On the other hand, high size ratios are not be used in printing or pharmacy, due to [2] and [9].

We can compare this figure to Figure 3e of [1] (Table 4). Table 4, in contrast, shows bigger and smaller drop sizes in their case. In $\alpha = 1.5$ case, when the outer liquid radius is still comparable to the radius of the inner one, the bigger drop size on their figure can be explained from the point of view that more liquid is taken to form drop than there is in a cylindrical segment with length λ_{\max} . In the case where $\alpha = 5$, it was not clear from their Figure 3e which of the bottom curves has $\alpha = 5$, and for Table 3 an asymptotic value of one of them at $k = 3.28$ was taken. For this case there is an appreciable difference in the drop sizes.

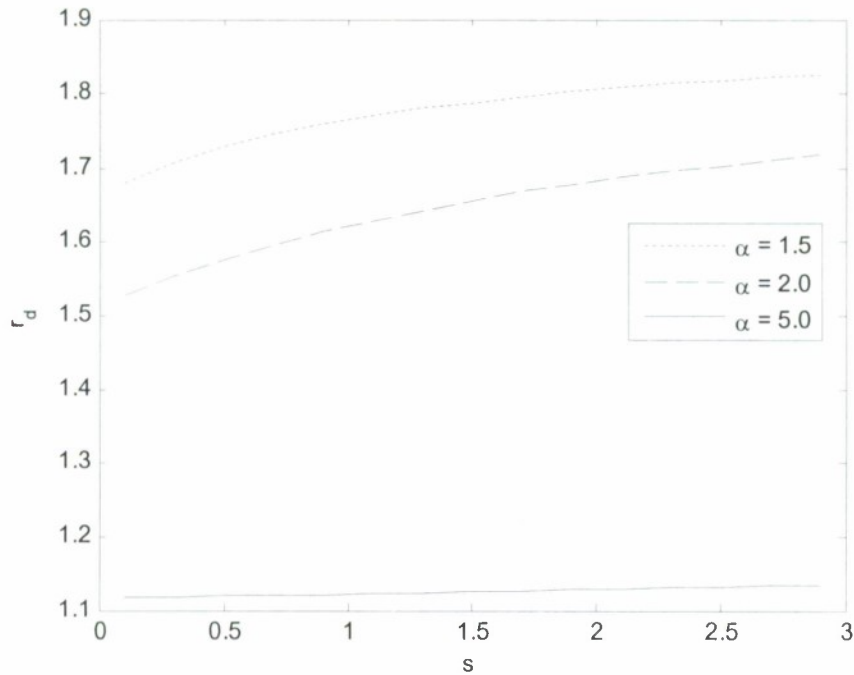


Figure 9 Effect of surface tension ratio on drop sizes at fixed radius ratios with $d = 1$.

	k_{\max}	r_d (Fig.9)	r_d (Fig.3e [1])
$\alpha = 1.5$	0.80	1.81	≈ 2.0
$\alpha = 2.0$	0.99	1.68	≈ 1.5
$\alpha = 5.0$	3.28	1.13	≈ 0.5

Overall, the comparison of the drop sizes shows an acceptable agreement with the paper by Bian and Mashayek [1] within 15% difference. This may attributed to the fact that their model is nonlinear and takes viscosity into account.

Conclusions

In this study an inviscid linear model has been developed to analyse the temporal instability behavior of compound jets. The difference of this model in comparison with inviscid models of other authors is in the way the governing equations are setup and solved. In contrast to other works, the dispersion equation obtained here is a second order algebraic equation producing only two symmetric roots, which makes it simpler to use in computations.

Based on Rayleigh's approach to evaluate the sizes of drops formed from a single jet, this study treats the breakup of the compound jet similar to that of a single jet. The breakup is assumed to occur at the most unstable wave number following from the dispersion equation. Since nonlinear effects are neglected, this study is not able to give information about the satellite drops formed.

Due to simplified form of the dispersion equation and the method of the drop size evaluation this method provides means for quick preliminary analysis of compound jets, such as how fast will disturbances grow at certain frequencies, or what will be the approximate size of the main drops at the most unstable frequencies.

The stability characteristics and drops sizes have been studied under varying radius, surface tension, and density ratios of two liquids comprising the compound jet. Overall comparison of the results of this study with those of other authors shows acceptable agreement for this type of analysis.

Nomenclature and subscripts

a	Radius of an undisturbed liquid surface
I_0	Bessel function of the first kind of order zero
I_1	Bessel function of the first kind of order one
K_0	Bessel function of the second kind of order zero
K_1	Bessel function of the second kind of order one
K	Axisymmetric surface curvature
k	Wave number of disturbance
p	Current pressure of disturbed flow
P	Initial base flow pressure before disturbance
r_d	Drop radius
z, r	Axial and radial coordinates
u, v	Axial and radial velocity of disturbance
λ	Wavelength of disturbance
ω	Growth rate of disturbance
ρ	Liquid density
σ	Surface tension at an interface between two fluids
ϕ	Velocity potential of disturbance
i	Number of interface: 1-inner interface, 2-outer free surface
j	Fluid index: 1-inner liquid, 2-outer liquid, g-ambient gas
max	Most unstable disturbance
*	Nondimensional quantity

References.

1. X. Bian and F. Mashayek, Compound Capillary Jet Breakup, *Proc. ILASS Americas Nineteenth Annual Conference on Liquid Atomization and Spray Systems*, 2006.
2. R. Bocanegra, J. Sampedro, A. Ganan-Calvo and M. Marquez, Monodisperse Structured Multi-Vesicle Microencapsulation Using Flow-Focusing and Controlled Disturbance, *Journal of Microencapsulation*, vol. 22(7), pp. 745-759, 2005.
3. D. Bogy, Drop Formation in a Circular Liquid Jet, *Annual Review of Fluid Mechanics*, vol. 11, pp. 207-228, 1979.
4. S. Chandrasekhar, *Hydrodynamic and Hydromagnetic Stability*, Oxford University Press, London, 1961.
5. A. Chaunan, C. Maldarelli, D. Rumschitzki and D. Papageorgiou, Temporal and Spatial Instability of an Inviscid Compound Jet, *Rheologica Acta*, vol. 35, pp. 567-583, 1996.
6. A. Chaunan, C. Maldarelli, D. Papageorgiou and D. Rumschitzki, Temporal Instability of Compound Threads and Jets, *Journal of Fluid Mechanics*, vol. 420, pp. 1-25, 2000.
7. I. Currie, *Fundamental Mechanics of Fluids*, 2nd Edition, McGraw-Hill, 1993.
8. P. Drazin and W. Reid, *Hydrodynamic Instability*, Cambridge University Press, 1984.
9. C. Hertz and B. Hermanrud, A Liquid Compound Jet, *Journal of Fluid Mechanics*, vol. 131, pp. 271-287, 1983.
10. F. Kamphoefner, Ink Jet Printing, *IEEE Transactions on Electron Devices*, vol. ED-19, No. 4, pp. 584-593, 1972.
11. J. Keller, S. Rubinow and T. Tu, Spatial Instability of a Jet, *The Physics of Fluids*, vol. 16, No. 12, pp. 2052-2055, 1973.
12. J. Lighthill, *Waves in Fluids*, Cambridge University Press, 1978.

13. S. Radev and B. Tchavdarov, Linear Capillary Instability of Compound Jets, *International Journal of Multiphase Flow*, vol. 14, No. 1, pp. 67-79, 1988.
14. L. Rayleigh, On the Instability of Jets, *Proceedings of the London Mathematical Society*, v. 10, pp. 4-13, 1879.
15. A. Sanz and J. Meseguer, One-Dimensional Linear Analysis of the Compound Jet, *Journal of Fluid Mechanics*, vol. 159, pp. 55-58, 1985.
16. V. Shkadov and G. Sisoev, Instability of a Two-Layer Capillary Jet, *International Journal of Multiphase Flow*, vol. 22, No 2, pp. 363-377, 1996.
17. V. Smirnov, *Course of Higher Mathematics*, vol. 2, Pergamon Press, 1964.

Appendix D – Modeling Dense Sprays Produced by Pressure-Swirl Atomizer – Parallel Processing Algorithm

1. Parallel Processing

1.1 Introduction to ScaLAPACK

Assuming the Runge-Kutta time integration scheme described in Section 2.1, the BEM calculation requires the solution of the large-dense system of linear equations for four times at every time step. Computational cost on solving this matrix system is fairly expensive. Current BEM codes developed within the research group[1] have used LU decomposition and SOR(Successive Over Relaxation) to solve the large-dense matrix system. Although SOR has been a quite successive method for solving larger matrix systems(over 1000 nodes), it has not been fast enough to get the grid convergence for high Weber number jets. A small grid size has been required to ensure the exactitude of computation in this case, so that computational cost of BEM based on SOR has been quite high. Therefore, it has been necessary to modify the matrix system solver in BEM.

The fully populated square matrix gives BEM codes a unique characteristic compared to the banded structure present in classical CFD codes. Classical CFD codes usually accomplish the acceleration by the use of sparse matrix inversion schemes and parallelization; dividing the computational domain into smaller matrices that are distributed to a set of CPUs. In addition, BEM atomization problems are distinguished by computational domains that increases with time, which yields different size matrix system at every time step. In addition, BEM matrices for fluids problems of this nature are generally poorly conditioned[1] , i.e. not diagonally dominant, thereby further complicating inversion processes. These issues make the matrix inversion in BEM fluids codes quite challenging. To improve performance of current codes, the ScaLAPACK utility was investigated as an aspect of the current work.

Scalable Linear Algebra Package (ScaLAPACK) is a set of library for distributed memory MIMD(Multiple Instruction stream, Multiple Data stream) parallel computers developed by the ScaLAPACK project[2] . ScaLAPACK provides routines for dense and band system of linear equations, linear least squares problems, and eigenvalue and singular value problems. One of the aims of ScaLAPACK project, 'portability', is achieved well so that it can run on any distributed memory computer using either MPI(Message Passing Interface) or PVM(Parallel Virtual Machine).

To use ScaLAPACK, it is necessary to install several codes: MPI or PVM, BLAS(Basic Linear Algebra Subprograms), BLACS(Basic Linear Algebra Communication Subprograms), and LAPACK(Linear Algebra Package). The MPI is a standardized and portable set of library for message-passing on the parallel computers. The PVM is a set of software tools and libraries for concurrent or parallel computation on interconnected computers of varied architecture. The BLAS is a set of subroutines for basic linear algebra calculations. The BLACS are a message-passing library for linear algebra. Software hierarchy of ScaLAPACK is described in Fig. 1.1.

ScaLAPACK provides driver routines, computational routines, and auxiliary routines. Driver routines are for solving standardized mathematical problems of matrix, e.g., linear system of matrix. It can be easily done by calling ScaLAPACK driver routines to achieve parallelization on the problem.

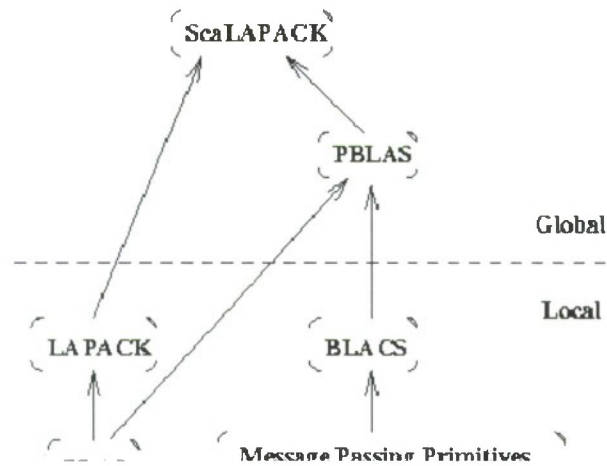


Fig. 1.1 Software hierarchy of ScaLAPACK[2]

1.2 Specification of HPC(High-performance computing) cluster

The performance of all parallelized computational algorithms depends not only on the organization of the algorithm but also on the specification and the parallel architecture of the computing machine. Typically all parallelized computational algorithm contains frequent data transmission between processors. The minimization of data transmission between processors is a way for increasing the performance of the algorithm. Furthermore, it is another way to use powerful computing machine for achieving significant reduction of actual code running time. All our current ScaLAPACK and BEM codes are running on our current HPC(High-performance computing) cluster. Hardware configuration of the HPC cluster is presented in Table. 1.1. Software used for ScaLAPACK and BEM calculation is presented in Table. 1.2.

Table 1.1 Hardware configuration of current HPC cluster used for ScaLAPACK & BEM calculation

Hardware	Description		Total Quantity
CPU	Head node	2.0 GHz AMD Opteron Quad Processor	1
	Computing nodes	2.4 GHz AMD Opteron Quad Processor	56
Motherboard	Head node	HP ProLiant DL385	1
	Computing nodes	HP ProLiant DL145	56
Memory	Head node	8 GB	284 GB
	Computing nodes	13 nodes – 8GB, 43 nodes – 4 GB	
Storage	Head node	1.2 TB	5.7 TB
	Computing nodes	80 GB	
Switch	HP ProCurve 5406zl (10 GB Interconnection support)		1
	HP ProCurve 5400zl (10 GB Interconnection support)		1

Table 1.2 Software used for ScaLAPACK & BEM calculation

Software	Description
Operating system	RedHat Linux 7.2
Fortran Compiler	PGI Compiler 7.1-2 by Potland Group Cluster Development kit
MPI	MPICH2 1.0.5
BLAS	Implemented in Potland Group Cluster Development kit
BLACS	BLACS 1.1 patched
LAPACK	Implemented in Potland Group Cluster Development kit
ScaLAPACK	ScaLAPACK 1.8.0

1.3 Dense System of Linear Equations Solver: PDGESV

ScaLAPACK provides highly effective solver, which is called the subroutine PDGESV, for the dense system of linear equations. The typical linear system solver, LU-factorization algorithm, has been implemented in PDGESV, however, it has been modified for the parallel computing machine. The modification can be characterized by two parts; Block LU Factorization and Parallel LU Factorization.

1.3.1 Block LU Factorization

Typical LU Factorization is working with each component of the matrix. Instead of each component of the matrix, Block LU Factorization is working with the blocked submatrices from the original matrix. Fig. 1.2 shows a decomposition of 9×9 matrix with 3×3 block matrix in order to operate the Block LU Factorization. With more general notations, $M \times N$ global matrix and $MB \times NB$ block matrix, the decomposition gives the following submatrices: A_{11} which is $MB \times NB$, A_{12} which is $MB \times (N - NB)$, A_{21} which is $(M - MB) \times NB$, and A_{22} which is $(M - MB) \times (N - NB)$.

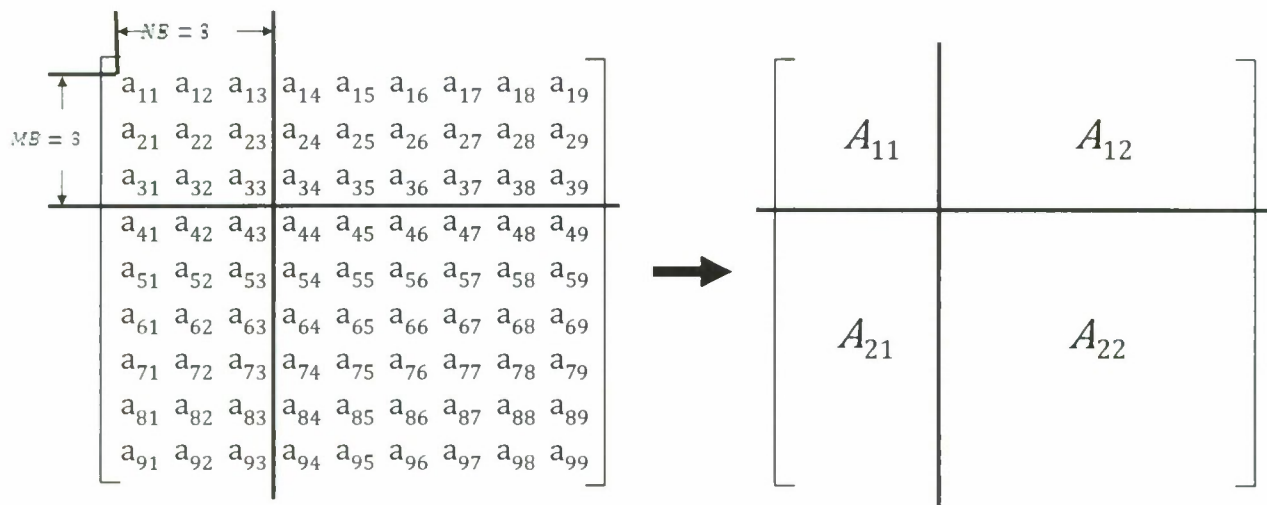


Fig. 1.2 9 x 9 matrix decomposition with 3 x 3 block matrix for Block LU Factorization

The $M \times N$ global matrix can be thought as it decomposed into a lower triangular matrix L and an upper triangular matrix U as illustrated in Fig. 1.3. The matrices L and U are decomposed into submatrices with the same $MB \times NB$ block structure containing sub-matrices L_{ij} on the lower matrix and U_{ij} on the upper matrix. Here, L_{11} is $MB \times NB$, L_{21} is $(M - MB) \times NB$, L_{22} is $(M - MB) \times (N - NB)$, U_{11} is $MB \times NB$, U_{12} is $MB \times (N - NB)$, and U_{22} is $(N - MB) \times (N - NB)$. It is possible to write equations between these submatrices in the global matrix matrix via standard linear algebra:

$$A_{11} = L_{11} U_{11} \quad (1.1)$$

$$A_{12} = L_{11} U_{12} \quad (1.2)$$

$$A_{21} = L_{21} U_{11} \quad (1.3)$$

$$A_{22} = L_{21} U_{12} + L_{22} U_{22} \quad (1.4)$$

$$\left[\begin{array}{c|c} A_{11} & A_{12} \\ \hline A_{21} & A_{22} \end{array} \right] = \left[\begin{array}{c|c} L_{11} & 0 \\ \hline L_{21} & L_{22} \end{array} \right] * \left[\begin{array}{c|c} U_{11} & U_{12} \\ \hline 0 & U_{22} \end{array} \right]$$

Fig. 1.3 Illustration of LU decomposition of global matrix with block matrix

Using this methodology, the matrix inversion process can capitalize on LU factorization schemes. For the Block LU Factorization process, an LU decomposition based on Gaussian elimination including scaling and pivoting is performed on the first column panel of the global matrix, A_{11} and A_{21} . Once A_{11} and A_{21} are decomposed, L_{11} , U_{11} , and L_{21} are known. Then U_{12} is computed using the equation (1.2) because A_{12} and L_{11} are known:

$$U_{12} = (L_{11})^{-1} A_{12} \quad (1.5)$$

At this time, last work to find the whole of L and U matrix of the global matrix is to find matrices L_{22} and U_{22} . Since A_{22} is not equal to $L_{22}U_{22}$, updating of the trailing matrix is required. Updated trailing submatrix A_{22}^* is computed:

$$A_{22}^* = A_{22} - L_{21} U_{12} \quad (1.6)$$

LU decomposition is applied again on the front column panel of A_{22}^* and the equation (1.5) is used again to update the front row panel of A_{22}^* . Using the equation (1.6), the trailing submatrix A_{33}^* is updated. This step is depicted in Fig. 1.4. The decomposition of the primary global matrix is completed by repeating this step on the matrix followed by the completion of the step on the former matrix.

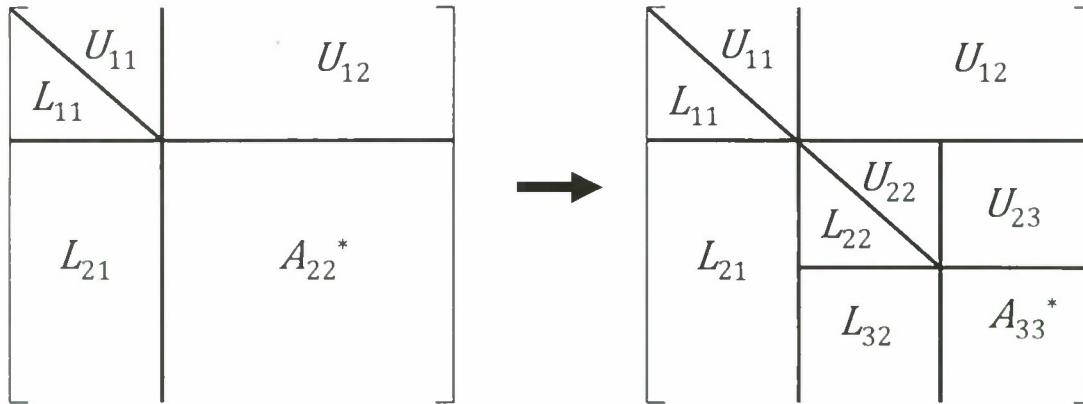


Fig. 1.4 Application of Block LU Factorization on the trailing submatrix

1.3.2 Parallel LU Factorization

While Block LU Factorization represents the work of LU factorization on only one CPU, Parallel LU Factorization represents the work of LU factorization with the data set distributed on a set of CPUs. Parallel LU Factorization contains frequent communication between CPUs, so that keeping the load balance between CPUs is a factor to affect the performance significantly. Choosing an appropriate data distribution scheme is important to keep load balance due to denseness of the matrix to be decomposed. The kind of data distribution scheme that will show greatest performance highly depends on the main algorithm. In the present study, 2-D block cyclic data distribution scheme has been selected as a distribution scheme for the parallel LU Factorization as ScaLAPACK project suggests it for the dense matrix[2]. They says that the effectiveness of 2-D block cyclic distribution of dense matrix is justified on the algorithm based on Gaussian elimination[2] so that we can easily see that 2-D block cyclic distribution can be a highly effective data distribution for LU factorization because it is based on Gaussian elimination operations.

An example of 2-D block cyclic data distribution is described in Fig. 1.5. *NPCOL* and *NPROW* represent the number of columns and the number of rows in the process grid consecutively. 9x9 global matrix is distributed on 2x3 processor grid with 2x2 block matrix and 5x4 maximum dimension of the matrix owned by any processor.

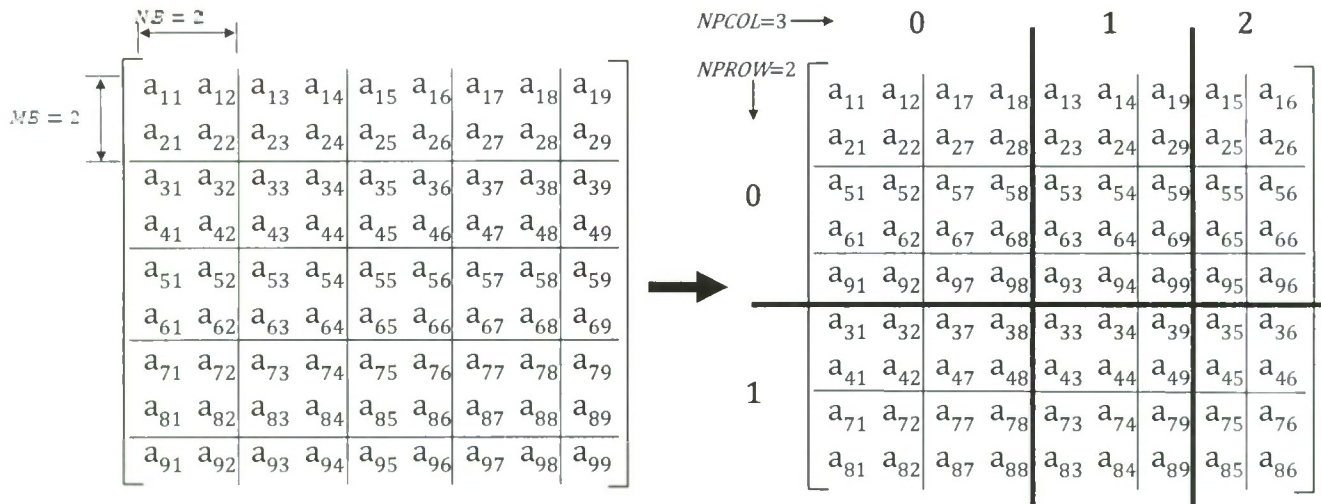


Fig. 1.5 2-D Block cyclic data distribution of 9x9 global matrix on 2x3 processor grid

The procedure to get L and U matrix from the distributed global matrix A is same with the procedure outlined in section 1.3.1 for Block LU Factorization. The front column panel of the distributed global matrix, which size is $M \times NB$, is decomposed using Gaussian elimination to find corresponding L and U. Using the equation (1.5) and (1.6), the front row panel and the trailing submatrix are updated. The difference with Block LU Factorization is that Parallel LU Factorization contains the communication between CPUs. The way to communicate and the number of communications depend on the algorithm. Most of communications occurred between processors in Parallel LU Factorization is the broadcast of data from a processor to other processors. Due to the characteristic of LU factorization, a current processor which sends data to other processors does not need to wait or receive data from processors. This is the reason that using the ScaLAPACK for the dense matrix on a set of CPUs shows better performance than running the LAPACK or running the ScaLAPACK on one CPU even though the main algorithm, Block LU Factorization, is applied on each case in the same way. This will be explained later.

As a whole, Parallel LU Factorization can be divided into two parts; one is the operation of Gaussian elimination, another is updating process for the front row panel and the trailing submatrix. Communications contained in each part are summarized in Fig. 1.6 and Fig. 1.7.

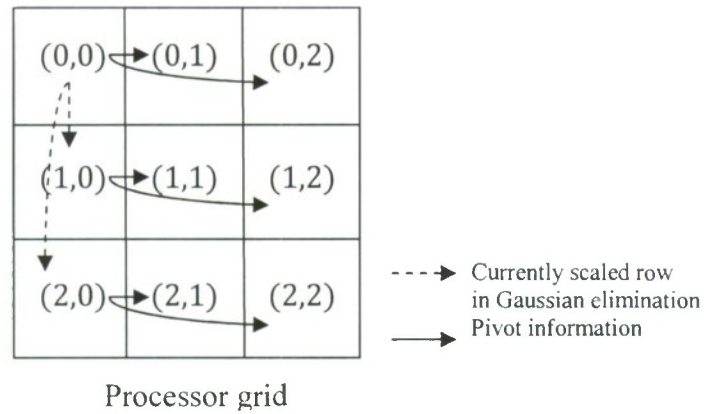


Fig. 1.6 Broadcasting layout in Gaussian elimination

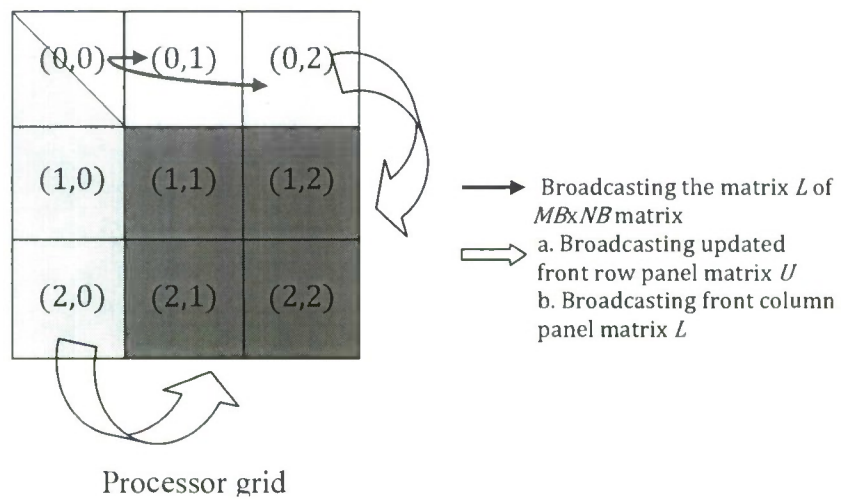


Fig. 1.7 Broadcasting layout in the updating process for the front row panel and the trailing submatrix

References

- [1] H. Park. *Flow Characteristics of Viscous High-Speed Jets in Axial/Swirl Injectors*. PhD thesis, Purdue University, 2005
- [2] L.S.Blackford, J. Choi, A. Cleary, E. D'Azevedo, J. Demmel, I.Dhillon, J. Dongarra, S.Hammarling, G. Henry, A. Petitet, K. Stanley, D. Walker, and R. C. Whaley. *ScaLAPACK Users' Guide*. Society for Industrial and Applied Mathematics, 1997.